Fluid Theory, Turbulence, and Dynamos in Magnetized Plasmas

James R. Beattie[1,2,3,†]

[1]Department of Astrophysical Sciences, Princeton University, Princeton, New Jersey 08540, USA

[2]Canadian Institute for Theoretical Astrophysics, University of Toronto, Toronto, Ontario M5S 3H8, Canada

[3]School of Natural Sciences, Institute for Advanced Study, Princeton, New Jersey 08540, USA

[†]NASA Hubble Fellow

August 2026

Abstract

Fluid theory is a reasonable description of the macroscopic scales of the Universe that exists around us. These lecture notes provide a self-contained, graduate-level introduction to waves, turbulence, and magnetic-field generation in astrophysical plasmas, combining foundational derivations with modern phenomenology and current research. The notes grew out of four lectures delivered at the 2026 summer school of the Simons Collaboration on Extreme Electrodynamics of Compact Sources (SCEECS), *Plasmas Around Black Holes and Neutron Stars*, held from July 27 to August 7 at the Institute of Astronomy, UNAM, in Baja California, Mexico. The presentation follows a continuous path from conservation laws, linear waves, and instabilities to hydrodynamic turbulence, magnetohydrodynamic turbulence, and fluid dynamos. A distinctive feature of the notes is the treatment of hydrodynamic turbulence, magnetohydrodynamic turbulence, and dynamo theory as successive parts of one physical argument. Exact energy budgets and third-order relations are developed alongside the phenomenologies of hydrodynamic and magnetohydrodynamic cascades. This parallel treatment separates conclusions that follow from the governing equations from those that depend on physical hypotheses. A consistent notation then connects nonlinear transfer and turbulent stretching to the amplification and saturation of magnetic fields. Throughout, explicit derivations make the principal assumptions visible, while discussions of intermittency, competing MHD cascade phenomenologies, dynamo saturation, and kinetic limitations connect established theory to questions that remain under active investigation. The aim is to equip students and researchers with the conceptual and mathematical tools needed to study these ubiquitous phenomena and to engage with current research at the limits of the fluid description.

Contents

1 Introduction

Fluid equations are compact enough to fit on a page, but their consequences span an enormous range of scales. The same momentum equation describes a sound wave, a turbulent eddy, and the flow that stretches a magnetic field. What changes from one problem to the next is the ordering of terms, the source of free energy, and the quantities that remain approximately conserved.

The development begins with conservation laws because they fix both the equations and their domain of validity. Waves and instabilities then show how to perturb those equations about a chosen equilibrium. Turbulence requires a different kind of reasoning because individual solutions become less useful than scale-by-scale fluxes and statistical averages. Magnetized turbulence adds a linear propagation time and a direction set by the magnetic field. Dynamo theory closes the circle by asking how a flow can create and maintain that field in the first place.

Most of the calculations use non-relativistic MHD with an isotropic pressure. The turbulence sections usually assume statistical homogeneity, and many of the cleanest results also assume incompressibility and a periodic domain. These restrictions are stated where they enter. These are all useful limits, defining the building blocks of modern theories, not claims that every astrophysical plasma obeys them. My hope is the broader community may engage in these extensive notes and find them useful as their own building blocks for teaching the forthcoming generation of plasma astrophysicists.

2 Acknowledgments

The curiosity, insight, and enthusiasm of the participating SCEECS students (especially, but not limited to, the "pulsar group") were a continual source of inspiration and shaped both the pace and emphasis of the lectures, even though we only got through a subset of what is contained in my lecture notes in this document. I am grateful to Dmitri Uzdensky, Alexander Philippov, and Kristopher Klein for many helpful discussions about how to organize and present these lectures.

Part I

Fluid theory, waves, and instabilities

The fluid and MHD equations are often introduced as a finished list. Here they are derived from balances over a moving material volume. This route keeps the meaning of each flux and force visible and makes the later approximations easier to judge.

3 From a moving fluid element to conservation laws

Each conservation law begins as an integral balance over an arbitrary material volume. The divergence theorem converts surface fluxes into volume integrals. Because the volume is arbitrary, the resulting integrand must vanish point by point, giving a local differential equation.

3.1 Eulerian fields and a material volume

A continuum model replaces the microscopic state by fields such as density $\rho(\boldsymbol{x}, t)$, velocity $\boldsymbol{u}(\boldsymbol{x}, t)$, plasma pressure $p(\boldsymbol{x}, t)$, and magnetic field $\boldsymbol{B}(\boldsymbol{x}, t)$. The variables $\boldsymbol{x} = (x, y, z)$ and t denote position and time. The field ρ gives mass per unit volume, and $\boldsymbol{u}$ assigns a velocity to each point in the continuum. At a fixed instant, a rectangular parcel surrounding $\boldsymbol{x}$ has coordinate side lengths Δx, Δy, and Δz. Its finite volume is

$$\Delta \mathcal{V} = \Delta x \, \Delta y \, \Delta z. \tag{1}$$

The continuum limit sends $\Delta x, \Delta y, \Delta z \to 0$ and defines the local volume element

$$\boxed{\mathrm{d}V = \mathrm{d}x \, \mathrm{d}y \, \mathrm{d}z.} \tag{2}$$

Physically, "small" means small compared with the macroscopic variation scale but still large enough to contain many particles and smooth over microscopic structure.

Each particle in an initial region $\mathcal{V}_0$ receives a label $\boldsymbol{a}$. The flow map $\boldsymbol{x} = \boldsymbol{\chi}(\boldsymbol{a}, t)$ carries that particle to its position at time t and satisfies

$$\left.\frac{\partial \boldsymbol{\chi}}{\partial t}\right|_{\boldsymbol{a}} = \boldsymbol{u}(\boldsymbol{\chi}(\boldsymbol{a}, t), t), \qquad \mathcal{V}(t) = \{\boldsymbol{\chi}(\boldsymbol{a}, t) : \boldsymbol{a} \in \mathcal{V}_0\}. \tag{3}$$

A *fluid element* is the infinitesimal limit of this material region. It contains the same labeled particles at every time, so no matter crosses $\partial \mathcal{V}(t)$. Although the schematic draws it initially as a cube, velocity gradients generally stretch, shear, rotate, and compress it into another shape.

Following one label $\boldsymbol{a}$ converts an Eulerian time derivative into a material derivative. For any scalar field $q(\boldsymbol{x}, t)$, the chain rule gives

$$\frac{\mathrm{d}}{\mathrm{d}t} q(\boldsymbol{\chi}(\boldsymbol{a}, t), t) = \left.\frac{\mathrm{D}q}{\mathrm{D}t}\right|_{\boldsymbol{x} = \boldsymbol{\chi}(\boldsymbol{a}, t)} = \frac{\partial q}{\partial t} + \left.\frac{\partial \boldsymbol{\chi}}{\partial t}\right|_{\boldsymbol{a}} \cdot \boldsymbol{\nabla} q = \frac{\partial q}{\partial t} + \boldsymbol{u} \cdot \boldsymbol{\nabla} q, \tag{4}$$

so

$$\boxed{\frac{\mathrm{D}}{\mathrm{D}t} = \frac{\partial}{\partial t} + \boldsymbol{u} \cdot \boldsymbol{\nabla}.} \tag{5}$$

The operator $\boldsymbol{\nabla} = (\partial/\partial x, \partial/\partial y, \partial/\partial z)$ is the spatial gradient. The notation distinguishes three time derivatives.

$$\begin{aligned} &\partial_t q && \text{means change of an Eulerian field at fixed position } \boldsymbol{x}, \\ &\frac{\mathrm{D}q}{\mathrm{D}t} && \text{means change of that field along a material trajectory}, \\ &\frac{\mathrm{d}Q}{\mathrm{d}t} && \text{means the ordinary derivative of a quantity } Q(t). \end{aligned}$$

Along a fixed particle label, $\mathrm{d}/\mathrm{d}t$ equals the material derivative of the corresponding Eulerian field. By contrast, $\mathrm{d}/\mathrm{d}t \int_{\mathcal{V}(t)} q\,\mathrm{d}V$ below differentiates the entire moving-volume integral; the Reynolds transport theorem accounts for the motion of its boundary. The volume of that particular material element changes according to

$$\frac{1}{\mathrm{d}V}\frac{\mathrm{d}(\mathrm{d}V)}{\mathrm{d}t} = \boldsymbol{\nabla}\cdot\boldsymbol{u}. \tag{6}$$

Thus positive divergence means local expansion and negative divergence means compression. Sections 1.2, 2.1–2.2, and 3.1 of Batchelor (2000) develop the continuum hypothesis, the Lagrangian–Eulerian connection, mass conservation, and material-volume transport.

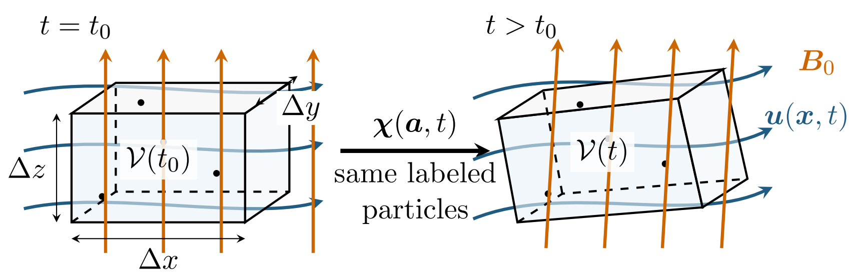

Figure 1. The flow map carries an initially rectangular material element at t_0 into a deformed element at $t > t_0$. The black markers identify the same material particles in both configurations, while the boundary of the material volume $\mathcal{V}(t)$ moves with the blue velocity field $\boldsymbol{u}(\boldsymbol{x}, t)$, so no marked particle crosses it. The map $\boldsymbol{\chi}(\boldsymbol{a}, t)$ carries each particle label $\boldsymbol{a}$ to its current position, and a background magnetic field $\boldsymbol{B}_0$ (orange) threads both local views.

The material volume follows the particles, even when it changes shape. A control volume, by contrast, occupies a fixed region of space while fluid crosses its boundary.

For a fixed control volume $\mathcal{V}$, every local conservation law has the schematic form

$$\boxed{\frac{\partial q}{\partial t} + \boldsymbol{\nabla}\cdot\boldsymbol{F}_q = s_q,} \tag{7}$$

where q denotes the conserved quantity per unit volume, $\boldsymbol{F}_q$ its flux vector, and s_q its net source per unit volume. The scalar $\boldsymbol{F}_q \cdot \hat{\boldsymbol{n}}$ gives the outward flux through a surface with unit normal $\hat{\boldsymbol{n}}$. Each conservation law assigns a specific physical meaning to these three quantities. The Reynolds transport theorem connects moving and fixed volumes.

$$\frac{\mathrm{d}}{\mathrm{d}t}\int_{\mathcal{V}(t)} q\,\mathrm{d}V = \int_{\mathcal{V}(t)} \left[\frac{\partial q}{\partial t} + \boldsymbol{\nabla}\cdot(q\boldsymbol{u})\right]\mathrm{d}V, \tag{8}$$

for a material volume whose boundary moves with $\boldsymbol{u}$. Setting $q = 1$ recovers (6). Appendix A derives (8), states the scalar, vector, and tensor forms of the divergence theorem, and explains why an integral identity over every volume implies a pointwise equation.

3.2 Conservation of mass

A material volume retains its mass, so

$$0 = \frac{\mathrm{d}}{\mathrm{d}t}\int_{\mathcal{V}(t)} \rho \,\mathrm{d}V = \int_{\mathcal{V}(t)} [\partial_t \rho + \boldsymbol{\nabla}\cdot(\rho\boldsymbol{u})]\,\mathrm{d}V. \tag{9}$$

Because the material volume is arbitrary, the integrand vanishes. Expanding its divergence then gives the equivalent material form

$$\partial_t \rho + \boldsymbol{\nabla}\cdot(\rho\boldsymbol{u}) = \frac{\mathrm{D}}{\mathrm{D}t}\rho + \rho\,\boldsymbol{\nabla}\cdot\boldsymbol{u} = 0. \tag{10}$$

Equivalently, in conservative form,

$$\boxed{\frac{\partial \rho}{\partial t} + \boldsymbol{\nabla}\cdot(\rho\boldsymbol{u}) = 0.} \tag{11}$$

The two terms in the material form have a direct interpretation. A moving element becomes less dense if it expands, and denser if it contracts. Sections 2.2 and 3.1 of Batchelor (2000) derive this local mass balance from a material volume and connect density change to the element's expansion rate.

3.3 Momentum from surface stresses and body forces

Newton's second law for a material element is

$$\frac{\mathrm{d}}{\mathrm{d}t}\int_{\mathcal{V}(t)} \rho\boldsymbol{u}\,\mathrm{d}V = \oint_{\partial\mathcal{V}(t)} \boldsymbol{\sigma}\cdot\hat{\boldsymbol{n}}\,\mathrm{d}A + \int_{\mathcal{V}(t)} \rho\boldsymbol{f}\,\mathrm{d}V, \tag{12}$$

where $\hat{\boldsymbol{n}}$ denotes the outward unit normal and $\mathrm{d}A$ a surface-area element. The symbol $\boldsymbol{\sigma}$ denotes the Cauchy stress tensor. The vector $\boldsymbol{\sigma}\cdot\hat{\boldsymbol{n}}$ is the surface force per unit area, or traction, acting across the boundary. The prescribed field $\boldsymbol{f}(\boldsymbol{x},t)$ is an external force per unit mass, so $\rho\boldsymbol{f}$ is the force per unit volume; gravity gives the special case $\boldsymbol{f} = \boldsymbol{g}$. For a Newtonian conducting plasma, the stress separates into plasma, viscous, and magnetic pieces,

$$\boldsymbol{\sigma} = -p\mathsf{I} + \boldsymbol{\tau} + \boldsymbol{\sigma}_B, \tag{13}$$

$$\boldsymbol{\tau} = \mu\left[\boldsymbol{\nabla}\boldsymbol{u} + (\boldsymbol{\nabla}\boldsymbol{u})^{\mathsf{T}} - \frac{2}{3}(\boldsymbol{\nabla}\cdot\boldsymbol{u})\mathsf{I}\right] + \zeta(\boldsymbol{\nabla}\cdot\boldsymbol{u})\mathsf{I}, \tag{14}$$

$$\boldsymbol{\sigma}_B = \frac{\boldsymbol{B}\otimes\boldsymbol{B}}{\mu_0} - \frac{B^2}{2\mu_0}\mathsf{I}. \tag{15}$$

The symbols I, $\boldsymbol{\tau}$, μ, and ζ denote the identity tensor, viscous stress, and dynamic shear and bulk viscosities, respectively; $\boldsymbol{\sigma}_B$ denotes the magnetic stress, and μ_0 denotes the permeability of free space. The abbreviation B^2 means $\boldsymbol{B}\cdot\boldsymbol{B}$, while $(\boldsymbol{\nabla}\boldsymbol{u})^{\mathsf{T}}$ denotes the transpose of the velocity-gradient tensor. The dyadic product obeys $(\boldsymbol{a}\otimes\boldsymbol{b})_{ij} = a_i b_j$, where $i, j \in \{1,2,3\}$ label Cartesian components; repeated indices imply summation. The isotropic term $B^2/(2\mu_0)$ acts like a magnetic pressure, while $\boldsymbol{B}\otimes\boldsymbol{B}/\mu_0$ pulls along field lines like tension in a stretched string. Sections 1.3 and 3.1–3.3 of Batchelor (2000) develop surface forces, material momentum balance, and Newtonian stress. Sections 1.1.7 and 1.3.1–1.3.3 of Spruit (2013) give the corresponding Lorentz-force and magnetic-stress construction.

Applying (8) component by component to the left-hand side and the tensor divergence theorem to the surface traction gives

$$\int_{\mathcal{V}(t)} \{\partial_t(\rho\boldsymbol{u}) + \boldsymbol{\nabla}\cdot(\rho\boldsymbol{u}\otimes\boldsymbol{u}) - \boldsymbol{\nabla}\cdot\boldsymbol{\sigma} - \rho\boldsymbol{f}\}\,\mathrm{d}V = 0. \tag{16}$$

Localization gives the conservative equation. The identity

$$\partial_t(\rho\boldsymbol{u}) + \boldsymbol{\nabla}\cdot(\rho\boldsymbol{u}\otimes\boldsymbol{u}) = \rho\frac{\mathrm{D}}{\mathrm{D}t}\boldsymbol{u} + \boldsymbol{u}[\partial_t\rho + \boldsymbol{\nabla}\cdot(\rho\boldsymbol{u})], \tag{17}$$

and continuity eliminate the bracket, yielding

$$\rho\frac{\mathrm{D}}{\mathrm{D}t}\boldsymbol{u} = -\boldsymbol{\nabla}p + \boldsymbol{\nabla}\cdot\boldsymbol{\tau} + \frac{1}{\mu_0}(\boldsymbol{\nabla}\times\boldsymbol{B})\times\boldsymbol{B} + \rho\boldsymbol{f}, \tag{18}$$

provided $\boldsymbol{\nabla}\cdot\boldsymbol{B} = 0$. The Lorentz force identity

$$\frac{1}{\mu_0}(\boldsymbol{\nabla}\times\boldsymbol{B})\times\boldsymbol{B} = -\boldsymbol{\nabla}\left(\frac{B^2}{2\mu_0}\right) + \frac{1}{\mu_0}(\boldsymbol{B}\cdot\boldsymbol{\nabla})\boldsymbol{B} \tag{19}$$

separates the magnetic-pressure force from magnetic tension.

In the ideal, inviscid limit ($\boldsymbol{\tau} = 0$), the conservative momentum equation takes the form

$$\boxed{\frac{\partial(\rho\boldsymbol{u})}{\partial t} + \boldsymbol{\nabla}\cdot\left[\rho\boldsymbol{u}\otimes\boldsymbol{u} + \left(p + \frac{B^2}{2\mu_0}\right)\mathsf{I} - \frac{\boldsymbol{B}\otimes\boldsymbol{B}}{\mu_0}\right] = \rho\boldsymbol{f}.} \tag{20}$$

The velocity flux $\rho\boldsymbol{u}\otimes\boldsymbol{u}$ contains the self-advection $(\boldsymbol{u}\cdot\boldsymbol{\nabla})\boldsymbol{u}$ that couples scales in hydrodynamic turbulence. Magnetic stress adds a second route for transferring momentum and energy in MHD turbulence.

3.4 Lorentz-force geometry in the tangent–normal–binormal basis

The pressure–tension split in (19) has a direct geometric interpretation. A smooth magnetic field line has position $\boldsymbol{r}(s)$, where s measures arclength along the line. The field strength and unit tangent obey

$$\boldsymbol{B} = B\hat{\boldsymbol{t}}, \qquad B = |\boldsymbol{B}|, \qquad \hat{\boldsymbol{t}} = \frac{\mathrm{d}\boldsymbol{r}}{\mathrm{d}s} = \frac{\boldsymbol{B}}{B}, \tag{21}$$

where B denotes the magnetic-field strength and $\hat{\boldsymbol{t}}$ denotes the unit tangent in the direction of the field. At a point with nonzero curvature, the Frenet–Serret relations complete the local tangent–normal–binormal (TNB) basis.

$$\frac{\mathrm{d}\hat{\boldsymbol{t}}}{\mathrm{d}s} = \kappa\hat{\boldsymbol{n}}, \qquad \frac{\mathrm{d}\hat{\boldsymbol{n}}}{\mathrm{d}s} = -\kappa\hat{\boldsymbol{t}} + \tau_{\mathrm{FS}}\hat{\boldsymbol{b}}, \qquad \frac{\mathrm{d}\hat{\boldsymbol{b}}}{\mathrm{d}s} = -\tau_{\mathrm{FS}}\hat{\boldsymbol{n}}. \tag{22}$$

The symbols $\kappa = 1/R_c$ and R_c denote the curvature and local radius of curvature. The principal normal $\hat{\boldsymbol{n}}$ points toward the center of curvature, $\hat{\boldsymbol{b}} = \hat{\boldsymbol{t}}\times\hat{\boldsymbol{n}}$ is the binormal, and τ_{FS} is the geometric torsion. The torsion measures how the plane containing $\hat{\boldsymbol{t}}$ and $\hat{\boldsymbol{n}}$ rotates along the field line; it does not denote the viscous stress tensor $\boldsymbol{\tau}$.

The derivatives along the three local directions are

$$\partial_s = \hat{\boldsymbol{t}}\cdot\boldsymbol{\nabla}, \qquad \partial_n = \hat{\boldsymbol{n}}\cdot\boldsymbol{\nabla}, \qquad \partial_b = \hat{\boldsymbol{b}}\cdot\boldsymbol{\nabla}, \qquad \boldsymbol{\nabla}_\perp = \hat{\boldsymbol{n}}\,\partial_n + \hat{\boldsymbol{b}}\,\partial_b. \tag{23}$$

Equation (21) and the first Frenet–Serret relation give

$$\frac{1}{\mu_0}(\boldsymbol{B}\cdot\boldsymbol{\nabla})\boldsymbol{B} = \frac{B}{\mu_0}\frac{\mathrm{d}}{\mathrm{d}s}(B\hat{\boldsymbol{t}}) \tag{24}$$

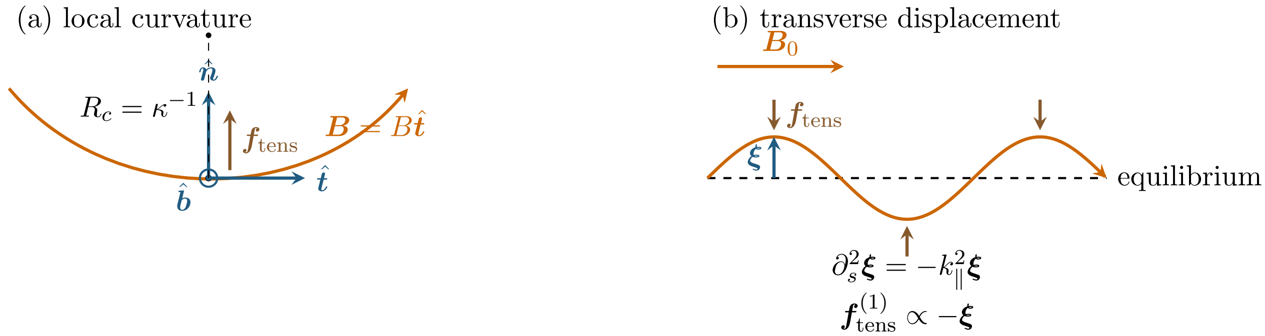

Figure 2. A smooth magnetic field line defines a local TNB basis. In panel (a), the tangent follows $\boldsymbol{B}$, the normal points toward the center of curvature, and the binormal completes the right-handed triad; curvature tension pulls in the $+\hat{\boldsymbol{n}}$ direction. Panel (b) applies that local force along a sinusoidally displaced field line. At each extremum, magnetic tension points back toward the straight equilibrium and therefore restores the displacement. Here $\boldsymbol{B}_0$ denotes the straight equilibrium field, $k_\parallel$ the wavenumber along it, and $\boldsymbol{\xi}$ and $\boldsymbol{f}_{\text{tens}}$ the transverse displacement and tension force density, respectively.

$$= \frac{B}{\mu_0}\frac{\mathrm{d}B}{\mathrm{d}s}\hat{\boldsymbol{t}} + \frac{B^2\kappa}{\mu_0}\hat{\boldsymbol{n}}. \tag{25}$$

The magnetic-pressure term becomes

$$-\boldsymbol{\nabla}\left(\frac{B^2}{2\mu_0}\right) = -\frac{B}{\mu_0}\frac{\mathrm{d}B}{\mathrm{d}s}\hat{\boldsymbol{t}} - \boldsymbol{\nabla}_\perp\left(\frac{B^2}{2\mu_0}\right). \tag{26}$$

The tangent terms in (25) and (26) cancel exactly. The Lorentz force per unit volume therefore becomes

$$\boxed{\boldsymbol{f}_{\mathrm{L}} = \boldsymbol{J}\times\boldsymbol{B} = -\boldsymbol{\nabla}_\perp\left(\frac{B^2}{2\mu_0}\right) + \underbrace{\frac{B^2\kappa}{\mu_0}\hat{\boldsymbol{n}}}_{\boldsymbol{f}_{\text{tens}}}.} \tag{27}$$

Here $\boldsymbol{f}_{\mathrm{L}}$ denotes the Lorentz force density and $\boldsymbol{J} = \boldsymbol{\nabla}\times\boldsymbol{B}/\mu_0$ denotes the electric-current density. The first term pushes from large magnetic pressure toward small magnetic pressure. The second term gives the curvature force. A field line with curvature κ pulls toward its center of curvature with magnitude $B^2/(\mu_0 R_c)$. The sign convention matters here. The Frenet–Serret principal normal points toward the center of curvature, so $\boldsymbol{f}_{\text{tens}}$ is parallel to $+\hat{\boldsymbol{n}}$, not opposite to it. If instead $\hat{\boldsymbol{n}}_{\text{out}} \equiv -\hat{\boldsymbol{n}}$ denotes the outward normal, then $\boldsymbol{f}_{\text{tens}} = -(B^2\kappa/\mu_0)\hat{\boldsymbol{n}}_{\text{out}}$. The word *restoring* compares tension with the displacement, not with the principal normal. At the crest of a displaced field line, for example, the center of curvature lies back toward the straight equilibrium. Both terms in (27) are perpendicular to $\hat{\boldsymbol{t}}$, so $\boldsymbol{f}_{\mathrm{L}}\cdot\hat{\boldsymbol{t}} = 0$. The Lorentz force can accelerate the plasma across a field line, but not directly along it.

Perturbing a straight, uniform field $\boldsymbol{B}_0 = B_0\hat{\boldsymbol{t}}_0$ in a plasma of uniform density ρ_0 shows why curvature tension restores a displaced field line. Here B_0 is the background field strength and $\hat{\boldsymbol{t}}_0$ its constant unit direction. A small transverse displacement $\boldsymbol{\xi}(s,t)$ satisfies $\boldsymbol{\xi}\cdot\hat{\boldsymbol{t}}_0 = 0$, and the displaced line is

$$\boldsymbol{r}(s,t) = s\hat{\boldsymbol{t}}_0 + \boldsymbol{\xi}(s,t). \tag{28}$$

Here s labels arclength along the unperturbed line. Because $|\partial_s\boldsymbol{r}| = 1 + \mathcal{O}(|\partial_s\boldsymbol{\xi}|^2)$, it also measures arclength along the displaced line to first order. The unit tangent and curvature vector are

$$\hat{\boldsymbol{t}} = \frac{\partial_s \boldsymbol{r}}{|\partial_s \boldsymbol{r}|} \simeq \hat{\boldsymbol{t}}_0 + \partial_s \boldsymbol{\xi}, \qquad \kappa \hat{\boldsymbol{n}} \simeq \partial_s \hat{\boldsymbol{t}} \simeq \partial_s^2 \boldsymbol{\xi}. \tag{29}$$

The symbol $\boldsymbol{B}_1$ denotes the first-order magnetic-field perturbation, consistently with the linear MHD equations below. The linearized flux-freezing relation gives $\boldsymbol{B}_1 = B_0 \partial_s \boldsymbol{\xi}$, which is perpendicular to $\boldsymbol{B}_0$. Thus $\boldsymbol{B}_0 \cdot \boldsymbol{B}_1 = 0$, and the field strength and magnetic pressure change only at second order. The curvature term in (27) therefore gives the linear tension force,

$$\boldsymbol{f}_{\text{tens}}^{(1)} = \frac{B_0^2}{\mu_0} \partial_s^2 \boldsymbol{\xi}. \tag{30}$$

For a Fourier displacement, $\boldsymbol{\xi} = \widehat{\boldsymbol{\xi}} \exp[i(k_\parallel s - \omega t)]$. The symbols $\widehat{\boldsymbol{\xi}}$, $k_\parallel$, ω, and i denote the complex displacement amplitude, the wavenumber parallel to $\boldsymbol{B}_0$, the angular frequency, and the imaginary unit, with $i^2 = -1$. Equation (30) then gives

$$\boxed{\boldsymbol{f}_{\text{tens}}^{(1)} = -\frac{B_0^2 k_\parallel^2}{\mu_0} \boldsymbol{\xi}.} \tag{31}$$

The minus sign shows explicitly that tension opposes the transverse displacement. Newton's second law then gives

$$\rho_0 \partial_t^2 \boldsymbol{\xi} = \frac{B_0^2}{\mu_0} \partial_s^2 \boldsymbol{\xi}, \qquad \omega^2 = v_{\text{A}}^2 k_\parallel^2, \qquad v_{\text{A}} = \frac{B_0}{\sqrt{\mu_0 \rho_0}}. \tag{32}$$

Thus a bent magnetic field line behaves locally like a stretched string. Section 4.3 derives the same Alfvén restoring force directly from the linearized MHD equations. Section 1.3.1 of Spruit (2013) develops the magnetic-pressure/curvature-force split and its field-line geometry.

3.5 Momentum diffusion by shear viscosity

Equation (18) contains the viscous force per unit volume $\boldsymbol{\nabla} \cdot \boldsymbol{\tau}$. If the dynamic viscosities μ and ζ remain spatially uniform, the Newtonian stress in (14) gives

$$\boldsymbol{\nabla} \cdot \boldsymbol{\tau} = \mu \nabla^2 \boldsymbol{u} + \left(\frac{\mu}{3} + \zeta\right) \boldsymbol{\nabla}(\boldsymbol{\nabla} \cdot \boldsymbol{u}). \tag{33}$$

For an incompressible plasma, $\boldsymbol{\nabla} \cdot \boldsymbol{u} = 0$. At constant density, the kinematic shear viscosity is $\nu = \mu/\rho$, and the viscous acceleration reduces to $\nu \nabla^2 \boldsymbol{u}$. A planar shear flow $\boldsymbol{u} = u_x(y,t)\hat{\boldsymbol{x}}$, where $\hat{\boldsymbol{x}}$ is the unit vector in the x direction, with no pressure gradient, magnetic force, or external force therefore obeys

$$\partial_t u_x = \nu\, \partial_y^2 u_x. \tag{34}$$

Viscosity smooths velocity differences on a length scale ℓ over the viscous time $t_\nu = \ell^2/\nu$. Comparing this time with the advection time ℓ/U gives the Reynolds number $\text{Re} = U\ell/\nu$. Viscous diffusion dominates for $\text{Re} \ll 1$, whereas inertia dominates for $\text{Re} \gg 1$. Viscous heating converts the kinetic energy that it removes from the resolved shear into internal energy. For incompressible flow, its local heating rate is $Q_\nu = 2\mu \boldsymbol{S} : \boldsymbol{S} \geq 0$, where the rate-of-strain tensor is $\boldsymbol{S} = [\boldsymbol{\nabla}\boldsymbol{u} + (\boldsymbol{\nabla}\boldsymbol{u})^\mathsf{T}]/2$ and $\boldsymbol{A} : \boldsymbol{C} = A_{ij} C_{ij}$ denotes double contraction. Sections 1.6 and 3.3 of Batchelor (2000) connect molecular momentum transport to the Newtonian stress and Navier–Stokes equation; Section 4.7 derives the Reynolds number by dynamical similarity.

3.6 Magnetic flux carried by a conducting element

Maxwell's equations impose

$$\frac{\partial \boldsymbol{B}}{\partial t} = -\boldsymbol{\nabla} \times \boldsymbol{E}, \qquad \boldsymbol{\nabla} \cdot \boldsymbol{B} = 0. \tag{35}$$

The field $\boldsymbol{E}(\boldsymbol{x}, t)$ denotes the electric field. The first equation expresses Faraday's law, and the second expresses the absence of magnetic monopoles. The ideal-conductor condition requires the electric field to vanish in the local fluid frame.

$$\boxed{\boldsymbol{E} + \boldsymbol{u} \times \boldsymbol{B} = 0.} \tag{36}$$

Combining this condition with Faraday's law gives the ideal induction equation.

$$\boxed{\frac{\partial \boldsymbol{B}}{\partial t} = \boldsymbol{\nabla} \times (\boldsymbol{u} \times \boldsymbol{B})} \qquad \boxed{\boldsymbol{\nabla} \cdot \boldsymbol{B} = 0} \tag{37}$$

In Cartesian components, x_j denotes the jth coordinate, and the conservation form is

$$\frac{\partial B_i}{\partial t} + \frac{\partial}{\partial x_j}(u_j B_i - u_i B_j) = 0. \tag{38}$$

For an oriented material surface $S(t)$ whose boundary $\partial S(t)$ moves with the fluid, $\mathrm{d}\boldsymbol{S} = \hat{\boldsymbol{n}}\,\mathrm{d}A$ is its vector area element, and $\mathrm{d}\boldsymbol{\ell}$ is the directed line element around its boundary. The moving-loop form of Faraday's law is

$$\frac{\mathrm{d}}{\mathrm{d}t} \int_{S(t)} \boldsymbol{B} \cdot \mathrm{d}\boldsymbol{S} = -\oint_{\partial S(t)} (\boldsymbol{E} + \boldsymbol{u} \times \boldsymbol{B}) \cdot \mathrm{d}\boldsymbol{\ell} = 0. \tag{39}$$

Thus ideal MHD conserves magnetic flux through every material loop, which is Alfvén's flux-freezing theorem. Sections 1.1.2–1.1.4 and 1.2.1 of Spruit (2013) develop ideal Ohm's law, the induction equation, and magnetic flux; Sections 2.1–2.2 derive Alfvén's theorem and state its qualifications. Reconnection occurs precisely where nonideal terms make the right-hand side of (39) nonzero.

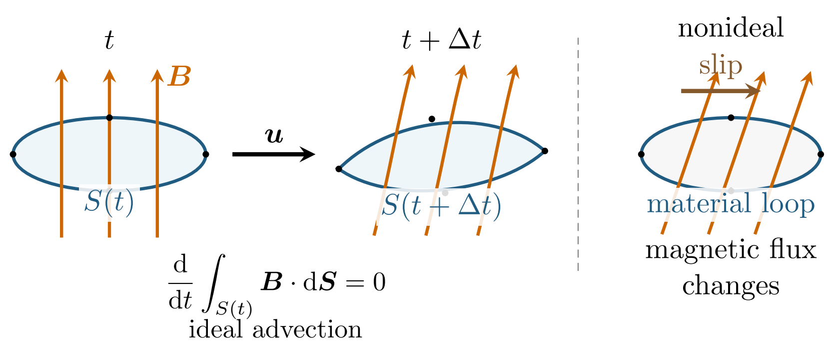

Figure 3. A material loop carries its spanning surface from $S(t)$ to $S(t + \Delta t)$. In ideal MHD, the same magnetic field lines thread the deformed surface, so the magnetic flux remains constant. Finite magnetic diffusion allows field lines to slip across the material loop and changes the enclosed flux.

A local form follows by expanding the curl in (37) and using $\boldsymbol{\nabla} \cdot \boldsymbol{B} = 0$ gives

$$\partial_t \boldsymbol{B} + (\boldsymbol{u} \cdot \boldsymbol{\nabla})\boldsymbol{B} = (\boldsymbol{B} \cdot \boldsymbol{\nabla})\boldsymbol{u} - \boldsymbol{B}(\boldsymbol{\nabla} \cdot \boldsymbol{u}), \qquad \frac{\mathrm{D}}{\mathrm{D}t}\boldsymbol{B} = (\boldsymbol{B} \cdot \boldsymbol{\nabla})\boldsymbol{u} - \boldsymbol{B}\boldsymbol{\nabla} \cdot \boldsymbol{u}. \tag{40}$$

Continuity gives $\frac{\mathrm{D}}{\mathrm{D}t}\rho = -\rho\boldsymbol{\nabla}\cdot\boldsymbol{u}$. The quotient rule therefore yields

$$\boxed{\frac{\mathrm{D}}{\mathrm{D}t}\left(\frac{\boldsymbol{B}}{\rho}\right) = \left(\frac{\boldsymbol{B}}{\rho}\cdot\boldsymbol{\nabla}\right)\boldsymbol{u}.} \tag{41}$$

Thus the velocity gradient stretches and rotates $\boldsymbol{B}/\rho$. For a thin comoving flux tube of length ℓ and cross-sectional area $A_\perp$, conserved flux $\Phi = BA_\perp$ and mass $m = \rho A_\perp \ell$ give

$$\frac{B}{\rho} = \frac{\Phi\ell}{m}. \tag{42}$$

The field strength therefore grows when the material line element stretches. Equations (39) and (41) state flux freezing in integral and local form, respectively.

3.7 Magnetic-field diffusion by Ohmic resistivity

A plasma with finite electrical conductivity σ_e has electrical resistivity $r_\mathrm{O} = 1/\sigma_\mathrm{e}$. The electric current density is $\boldsymbol{J} = \boldsymbol{\nabla}\times\boldsymbol{B}/\mu_0$, and the scalar resistive form of Ohm's law is

$$\boldsymbol{E} + \boldsymbol{u}\times\boldsymbol{B} = r_\mathrm{O}\boldsymbol{J} = \mu_0\eta\boldsymbol{J}, \qquad \eta = \frac{1}{\mu_0\sigma_\mathrm{e}}, \tag{43}$$

where η denotes the magnetic diffusivity, with dimensions of length squared per unit time. MHD texts often call η the resistivity, although it is a diffusivity rather than the electrical resistivity r_O. For uniform η, combining Faraday's law with $\boldsymbol{\nabla}\cdot\boldsymbol{B} = 0$ gives

$$\boxed{\partial_t\boldsymbol{B} = \boldsymbol{\nabla}\times(\boldsymbol{u}\times\boldsymbol{B}) + \eta\nabla^2\boldsymbol{B}.} \tag{44}$$

The second term diffuses magnetic structure. A field varying on a length scale ℓ decays on the resistive time $t_\eta = \ell^2/\eta$. For a characteristic speed U, comparison with the advection time ℓ/U gives the magnetic Reynolds number $\mathrm{Rm} = U\ell/\eta$. Flux freezing is a good approximation when $\mathrm{Rm} \gg 1$ on the scale of interest; finite resistivity permits the magnetic flux through a material loop to change according to

$$\frac{\mathrm{d}}{\mathrm{d}t}\int_{S(t)}\boldsymbol{B}\cdot\mathrm{d}\boldsymbol{S} = -\oint_{\partial S(t)}\mu_0\eta\boldsymbol{J}\cdot\mathrm{d}\boldsymbol{\ell}. \tag{45}$$

The corresponding Ohmic heating rate per unit volume is $Q_\eta = \boldsymbol{J}\cdot(\boldsymbol{E}+\boldsymbol{u}\times\boldsymbol{B}) = \mu_0\eta J^2 = J^2/\sigma_\mathrm{e} \geq 0$, where $J^2 = \boldsymbol{J}\cdot\boldsymbol{J}$. Ohmic heating converts magnetic energy into internal energy. Section 1.10 of Spruit (2013) derives magnetic diffusion and Rm, while Chapter 4, Section 4.4.1 of Goedbloed et al. (2019) places the same terms in resistive MHD.

3.8 Energy exchanges among internal, kinetic, and magnetic reservoirs

The symbol e denotes the internal energy per unit mass, and $u^2 = \boldsymbol{u}\cdot\boldsymbol{u}$. The ideal-MHD total energy per unit volume $\mathcal{E}_\mathrm{vol}$ is

$$\mathcal{E}_\mathrm{vol} = \rho e + \frac{1}{2}\rho u^2 + \frac{B^2}{2\mu_0}. \tag{46}$$

For an adiabatic, inviscid plasma, the first law for a material element is

$$\rho\frac{\mathrm{D}}{\mathrm{D}t}e = -p\boldsymbol{\nabla}\cdot\boldsymbol{u}, \qquad \partial_t(\rho e) + \boldsymbol{\nabla}\cdot(\rho e\boldsymbol{u}) = -p\boldsymbol{\nabla}\cdot\boldsymbol{u}, \tag{47}$$

where continuity gives the second equality. Dotting the inviscid momentum equation with $\boldsymbol{u}$, using continuity, and applying $-\boldsymbol{u}\cdot\boldsymbol{\nabla}p = -\boldsymbol{\nabla}\cdot(p\boldsymbol{u}) + p\boldsymbol{\nabla}\cdot\boldsymbol{u}$ gives

$$\partial_t\left(\frac{\rho u^2}{2}\right) + \boldsymbol{\nabla}\cdot\left[\left(\frac{\rho u^2}{2} + p\right)\boldsymbol{u}\right] = p\boldsymbol{\nabla}\cdot\boldsymbol{u} + \boldsymbol{u}\cdot(\boldsymbol{J}\times\boldsymbol{B}) + \rho\boldsymbol{f}\cdot\boldsymbol{u}, \tag{48}$$

where $\boldsymbol{J} = \boldsymbol{\nabla}\times\boldsymbol{B}/\mu_0$ is the current density in magnetoquasistatic MHD. Poynting's theorem in the magnetoquasistatic approximation supplies the magnetic-energy balance,

$$\partial_t\left(\frac{B^2}{2\mu_0}\right) + \boldsymbol{\nabla}\cdot\left(\frac{\boldsymbol{E}\times\boldsymbol{B}}{\mu_0}\right) = -\boldsymbol{J}\cdot\boldsymbol{E} = -\boldsymbol{u}\cdot(\boldsymbol{J}\times\boldsymbol{B}), \tag{49}$$

where $\boldsymbol{E} = -\boldsymbol{u}\times\boldsymbol{B}$ gives the last step. The pressure-work terms cancel between (47) and (48); the Lorentz work cancels between (48) and (49).

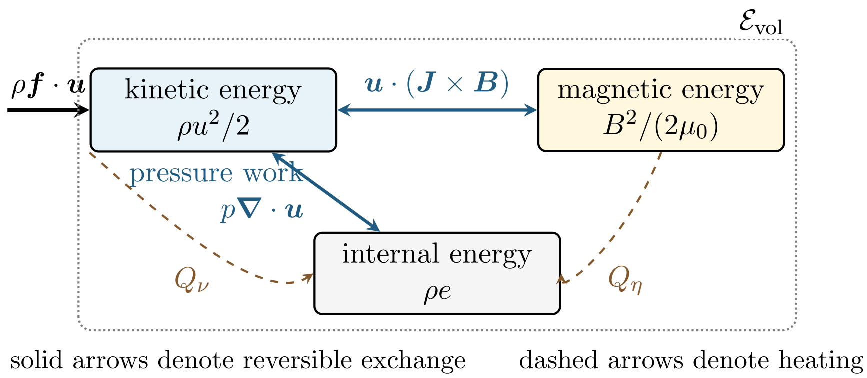

Figure 4. Pressure work transfers energy between the internal and kinetic reservoirs, while the Lorentz force transfers energy between the kinetic and magnetic reservoirs. Adding the three ideal balances cancels these internal transfers. External work $\rho\boldsymbol{f}\cdot\boldsymbol{u}$ changes the total energy; nonideal viscous and Ohmic heating (Q_ν and Q_η) convert kinetic and magnetic energy into internal energy.

Under ideal Ohm's law,

$$\frac{\boldsymbol{E}\times\boldsymbol{B}}{\mu_0} = \frac{B^2\boldsymbol{u} - (\boldsymbol{u}\cdot\boldsymbol{B})\boldsymbol{B}}{\mu_0}. \tag{50}$$

Adding the internal, kinetic, and magnetic energy balances gives

$$\boxed{\frac{\partial\mathcal{E}_{\rm vol}}{\partial t} + \boldsymbol{\nabla}\cdot\left[\left(\mathcal{E}_{\rm vol} + p + \frac{B^2}{2\mu_0}\right)\boldsymbol{u} - \frac{(\boldsymbol{u}\cdot\boldsymbol{B})\boldsymbol{B}}{\mu_0}\right] = \rho\boldsymbol{f}\cdot\boldsymbol{u}.} \tag{51}$$

Viscosity and resistivity convert kinetic and magnetic energy into internal energy. Heat conduction changes the energy flux, while radiation and external driving can remove or add total energy. Ideal MHD neglects these effects only when they act slowly on the scales and times under discussion. Section 3.4 of Batchelor (2000) derives the internal-energy balance for a moving fluid, Section 1.9 of Spruit (2013) interprets the MHD Poynting flux, and Chapter 4, Sections 4.3.1–4.3.2 of Goedbloed et al. (2019) give the local and global MHD conservation laws.

3.9 The ideal-MHD system and its assumptions

Equations (11), (20), (37), and (51), plus an equation of state, form a closed ideal-MHD system. For a one-temperature ideal plasma,

$$p = (\gamma-1)\rho e, \qquad c_s^2 = \left(\frac{\partial p}{\partial\rho}\right)_s = \frac{\gamma p}{\rho}. \tag{52}$$

The symbols γ, s, and c_s denote the adiabatic index, specific entropy, and adiabatic sound speed; the definition of c_s evaluates the derivative at fixed s. For a rapidly cooled or explicitly isothermal model, instead $p = c_s^2\rho$ with constant c_s.

The model assumes a continuum, a non-relativistic bulk flow, quasi-neutrality on the scales of interest, a single bulk velocity, negligible displacement current, and sufficiently large conductivity.

Nondimensionalization

Retaining viscosity and magnetic diffusion in the governing equations allows direct comparison of the physical terms on specified length and time scales.

$$\partial_t\rho + \boldsymbol{\nabla}\cdot(\rho\boldsymbol{u}) = 0, \tag{53}$$

$$\frac{\mathrm{D}}{\mathrm{D}t}\boldsymbol{u} = -\frac{1}{\rho}\boldsymbol{\nabla}p + \frac{1}{\mu_0\rho}(\boldsymbol{\nabla}\times\boldsymbol{B})\times\boldsymbol{B} + \frac{1}{\rho}\boldsymbol{\nabla}\cdot\boldsymbol{\tau} + \boldsymbol{f}, \tag{54}$$

$$\partial_t\boldsymbol{B} = \boldsymbol{\nabla}\times(\boldsymbol{u}\times\boldsymbol{B}) + \eta\nabla^2\boldsymbol{B}. \tag{55}$$

Equation (43) defines the magnetic diffusivity η, and $\nabla^2 = \boldsymbol{\nabla}\cdot\boldsymbol{\nabla}$ defines the Laplacian. At the reference density, the kinematic shear viscosity is $\nu = \mu/\rho_0$, so that $\boldsymbol{\nabla}\cdot\boldsymbol{\tau} \sim \rho_0\nu\nabla^2\boldsymbol{u}$. The characteristic length L, speed U, density ρ_0, pressure p_0, magnetic-field strength B_0, and external acceleration f_0 introduce dimensionless starred variables through

$$\boldsymbol{x} = L\boldsymbol{x}^*, \quad t = \frac{L}{U}t^*, \quad \boldsymbol{u} = U\boldsymbol{u}^*, \quad \rho = \rho_0\rho^*, \quad p = p_0p^*, \quad \boldsymbol{B} = B_0\boldsymbol{B}^*, \quad \boldsymbol{f} = f_0\boldsymbol{f}^*, \quad \boldsymbol{\tau} = \frac{\rho_0\nu U}{L}\boldsymbol{\tau}^*. \tag{56}$$

An asterisk marks each dimensionless variable. The reference sound and Alfvén speeds are $c_{s0} = \sqrt{\gamma p_0/\rho_0}$ and $v_{\mathrm{A}0} = B_0/\sqrt{\mu_0\rho_0}$. Substituting (56) and dividing continuity, momentum, and induction by their inertial scales ρ_0U/L, U^2/L, and B_0U/L, respectively, gives

$$\partial_{t^*}\rho^* + \boldsymbol{\nabla}^*\cdot(\rho^*\boldsymbol{u}^*) = 0, \tag{57}$$

$$(\partial_{t^*} + \boldsymbol{u}^*\cdot\boldsymbol{\nabla}^*)\boldsymbol{u}^* = -\frac{1}{\gamma\mathcal{M}^2}\frac{\boldsymbol{\nabla}^*p^*}{\rho^*} + \frac{1}{\mathcal{M}_{\mathrm{A}}^2\rho^*}(\boldsymbol{\nabla}^*\times\boldsymbol{B}^*)\times\boldsymbol{B}^* + \frac{1}{\mathrm{Re}\,\rho^*}\boldsymbol{\nabla}^*\cdot\boldsymbol{\tau}^* + \mathcal{A}_f\boldsymbol{f}^*, \tag{58}$$

$$\partial_{t^*}\boldsymbol{B}^* = \boldsymbol{\nabla}^*\times(\boldsymbol{u}^*\times\boldsymbol{B}^*) + \frac{1}{\mathrm{Rm}}\nabla^{*2}\boldsymbol{B}^*. \tag{59}$$

The gradient $\boldsymbol{\nabla}^*$ differentiates with respect to $\boldsymbol{x}^*$. The coefficients are

$$\boxed{\mathcal{M} = \frac{U}{c_{s0}}, \qquad \mathcal{M}_{\mathrm{A}} = \frac{U}{v_{\mathrm{A}0}}, \qquad \mathrm{Re} = \frac{UL}{\nu}, \qquad \mathrm{Rm} = \frac{UL}{\eta}, \qquad \mathcal{A}_f = \frac{f_0L}{U^2}.} \tag{60}$$

The quantities $\mathcal{M}$, $\mathcal{M}_{\mathrm{A}}$, Re, Rm, and $\mathcal{A}_f$ are the sonic Mach number, Alfvénic Mach number, Reynolds number, magnetic Reynolds number, and dimensionless forcing strength, respectively. Thus $(\gamma\mathcal{M}^2)^{-1}$ compares plasma-pressure forces with inertia, $\mathcal{M}_{\mathrm{A}}^{-2}$ compares magnetic forces with inertia, Re^{-1} and Rm^{-1} measure viscous and resistive transport over one flow time, and $\mathcal{A}_f$ compares external acceleration with inertial acceleration. If $\boldsymbol{f} = \boldsymbol{g}$, with $g = |\boldsymbol{g}|$ and $f_0 = g$, then $\mathcal{A}_f = \mathrm{Fr}^{-2}$ with the Froude number $\mathrm{Fr} = U/\sqrt{gL}$.

These parameters also determine the magnetic Prandtl number Pm and the reference plasma beta β_0.

$$\boxed{\mathrm{Pm} = \frac{\nu}{\eta} = \frac{\mathrm{Rm}}{\mathrm{Re}}} \qquad \boxed{\beta_0 = \frac{2\mu_0p_0}{B_0^2} = \frac{2\mathcal{M}_{\mathrm{A}}^2}{\gamma\mathcal{M}^2}} \tag{61}$$

The ideal limit is $\mathrm{Re}, \mathrm{Rm} \to \infty$ on the chosen scales. The energy equation contains the same ratios and introduces additional ones only when cooling, conduction, radiation, or other physics enters the model. Subsequent equations drop the asterisks and identify all dimensional variables explicitly. Chapter 4, Sections 4.1–4.4 of Goedbloed et al. (2019) develop the ideal and resistive MHD systems, flux conservation, and energy conservation. Section 4.1.2 of that text, Section 4.7 of Batchelor (2000), and Sections 1.4 and 1.10 of Spruit (2013) provide the corresponding scale analysis, Reynolds numbers, plasma beta, and magnetic Reynolds number.

> **A useful check.** Which ingredients close the conservation laws, and what limits ideal MHD? The stress law, Ohm's law, and equation of state close the mass, momentum, magnetic-flux, and energy balances. The nearest neglected scale or time then limits the model; examples include a mean free path, ion skin depth, gyroradius, resistive scale, light-crossing time, cooling time, and radiation mean free path.

4 Waves and their restoring forces

The conservation laws now form a closed nonlinear evolution system. Small-amplitude perturbations isolate its restoring forces and characteristic propagation speeds.

4.1 Small perturbations about a uniform equilibrium

For any dependent variable q, the perturbation expansion is

$$q(\boldsymbol{x}, t) = q_0 + \epsilon q_1(\boldsymbol{x}, t), \qquad \epsilon \ll 1, \tag{62}$$

where q_0 denotes the equilibrium value, q_1 denotes a perturbation with the same physical units, and the dimensionless parameter ϵ measures its relative amplitude. Substitution into every nonlinear equation retains terms proportional to ϵ and discards products of two perturbations because they enter at $\mathcal{O}(\epsilon^2)$. The chosen equilibrium is uniform and static,

$$\rho_0, p_0, \boldsymbol{B}_0 = \text{constant}, \qquad \boldsymbol{u}_0 = 0, \tag{63}$$

and the analysis considers free waves, so $\boldsymbol{f}_0 = \boldsymbol{f}_1 = 0$ (or, for uniform gravity, equivalently adopts a freely falling frame). A background pressure gradient that balances a force produces a stratified equilibrium and buoyancy physics. A nonzero $\boldsymbol{f}_1$ drives the plasma but does not change the frequencies of the corresponding free waves. Plane waves take the form

$$q_1 = \widehat{q}_1\, e^{i(\boldsymbol{k}\cdot\boldsymbol{x} - \omega t)}, \qquad \partial_t \mapsto -i\omega, \qquad \boldsymbol{\nabla} \mapsto i\boldsymbol{k}. \tag{64}$$

The symbols $\widehat{q}_1$, $\boldsymbol{k}$, $k = |\boldsymbol{k}|$, and ω denote the generally complex first-order wave amplitude, wavevector, wavenumber, and angular frequency, with $i^2 = -1$. The physical perturbation is the real part of the complex expression. For real $\boldsymbol{k}$, real ω describes oscillation, whereas $\mathrm{Im}\,\omega > 0$ describes exponential growth. Chapter 2, Section 2.3 of Drazin (2002) introduces the linearized stability problem, and Chapter 6, Section 6.1.2 of Goedbloed et al. (2019) develops linearization for ideal MHD.

4.2 Hydrodynamic linearization, term by term

Setting $\boldsymbol{B} = 0$ gives

$$\rho = \rho_0 + \epsilon\rho_1, \qquad p = p_0 + \epsilon p_1, \qquad \boldsymbol{u} = \epsilon\boldsymbol{u}_1. \tag{65}$$

Continuity expands as

$$0 = \epsilon\left(\partial_t\rho_1 + \rho_0\boldsymbol{\nabla}\cdot\boldsymbol{u}_1\right) + \epsilon^2\boldsymbol{\nabla}\cdot(\rho_1\boldsymbol{u}_1), \tag{66}$$

while the primitive momentum equation expands as

$$\epsilon\rho_0\partial_t\boldsymbol{u}_1 + \epsilon^2\rho_1\partial_t\boldsymbol{u}_1 + \epsilon^2(\rho_0 + \epsilon\rho_1)(\boldsymbol{u}_1\cdot\boldsymbol{\nabla})\boldsymbol{u}_1 = -\epsilon\boldsymbol{\nabla}p_1. \tag{67}$$

Dividing by ϵ and taking $\epsilon \to 0$ gives

$$\boxed{\partial_t\rho_1 + \rho_0\boldsymbol{\nabla}\cdot\boldsymbol{u}_1 = 0} \qquad \boxed{\rho_0\partial_t\boldsymbol{u}_1 = -\boldsymbol{\nabla}p_1} \tag{68}$$

The closure follows by Taylor expanding $p = p(\rho, s)$,

$$p_1 = \left(\frac{\partial p}{\partial\rho}\right)_{s,0}\rho_1 + \left(\frac{\partial p}{\partial s}\right)_{\rho,0}s_1. \tag{69}$$

For an ideal adiabatic plasma, $\frac{\mathrm{D}}{\mathrm{D}t}s = 0$ expands to $\partial_t s_1 = 0$. A propagating disturbance therefore has $s_1 = 0$, so $p_1 = c_s^2\rho_1$, where $c_s^2 = (\partial p/\partial\rho)_{s,0}$ gives the equilibrium sound speed; retaining a stationary s_1 supplies a zero-frequency entropy mode.

Differentiating continuity in time and taking the divergence of momentum gives

$$\partial_t^2\rho_1 + \rho_0\boldsymbol{\nabla}\cdot\partial_t\boldsymbol{u}_1 = 0, \qquad \rho_0\boldsymbol{\nabla}\cdot\partial_t\boldsymbol{u}_1 = -\nabla^2 p_1. \tag{70}$$

Eliminating the velocity divergence gives

$$\partial_t^2\rho_1 - c_s^2\nabla^2\rho_1 = 0, \qquad \boxed{\omega^2 = c_s^2k^2.} \tag{71}$$

The Fourier-space equations show the polarization as well as the frequency,

$$\omega\widehat{\rho}_1 = \rho_0\boldsymbol{k}\cdot\widehat{\boldsymbol{u}}_1, \qquad \omega\rho_0\widehat{\boldsymbol{u}}_1 = \boldsymbol{k}\widehat{p}_1, \qquad \widehat{p}_1 = c_s^2\widehat{\rho}_1. \tag{72}$$

The momentum equation has no component perpendicular to $\boldsymbol{k}$, so the two transverse velocity components are zero-frequency vortical modes. The propagating sound modes have $\widehat{\boldsymbol{u}}_1 \parallel \boldsymbol{k}$ and $\widehat{\rho}_1/\rho_0 = (k/\omega)\widehat{u}_{1\parallel}$, where $\widehat{u}_{1\parallel} = \widehat{\boldsymbol{u}}_1\cdot\boldsymbol{k}/k$ denotes the velocity amplitude along the wavevector. A compression raises the pressure, and the resulting pressure gradient accelerates the plasma back toward equilibrium. Inertia carries it past equilibrium and produces an oscillation. The other wave families likewise combine inertia with a restoring force. Chapter 5, Sections 5.1.1–5.1.2 of Goedbloed et al. (2019) derive the sound-wave equations, dispersion relation, and pressure-restored longitudinal polarization.

4.3 Linear ideal-MHD equations

The MHD calculation perturbs all four primitive fields,

$$\rho = \rho_0 + \epsilon\rho_1, \qquad p = p_0 + \epsilon p_1, \qquad \boldsymbol{u} = \epsilon\boldsymbol{u}_1, \qquad \boldsymbol{B} = \boldsymbol{B}_0 + \epsilon\boldsymbol{B}_1. \tag{73}$$

The equilibrium fields ρ_0, p_0, and $\boldsymbol{B}_0$ are spatially uniform and time-independent, while $\boldsymbol{u}_0 = 0$. The adiabatic closure remains $p_1 = c_s^2\rho_1$.

Linearized continuity

Substitution into mass conservation gives

$$\begin{aligned}0 &= \partial_t(\rho_0 + \epsilon\rho_1) + \boldsymbol{\nabla}\cdot[(\rho_0+\epsilon\rho_1)\epsilon\boldsymbol{u}_1] \\ &= \epsilon\left(\partial_t\rho_1 + \rho_0\boldsymbol{\nabla}\cdot\boldsymbol{u}_1\right) + \epsilon^2\boldsymbol{\nabla}\cdot(\rho_1\boldsymbol{u}_1).\end{aligned} \tag{74}$$

Dividing by ϵ and taking $\epsilon \to 0$ leaves

$$\boxed{\partial_t\rho_1 + \rho_0\boldsymbol{\nabla}\cdot\boldsymbol{u}_1 = 0.} \tag{75}$$

Linearized induction and magnetic divergence

The ideal induction equation expands as

$$\begin{aligned}\partial_t(\boldsymbol{B}_0 + \epsilon\boldsymbol{B}_1) &= \boldsymbol{\nabla}\times[\epsilon\boldsymbol{u}_1\times(\boldsymbol{B}_0+\epsilon\boldsymbol{B}_1)] \\ \epsilon\partial_t\boldsymbol{B}_1 &= \epsilon\boldsymbol{\nabla}\times(\boldsymbol{u}_1\times\boldsymbol{B}_0) + \epsilon^2\boldsymbol{\nabla}\times(\boldsymbol{u}_1\times\boldsymbol{B}_1).\end{aligned} \tag{76}$$

The first-order equation is therefore

$$\boxed{\partial_t\boldsymbol{B}_1 = \boldsymbol{\nabla}\times(\boldsymbol{u}_1\times\boldsymbol{B}_0).} \tag{77}$$

Taking its divergence shows why the solenoidal constraint persists.

$$\partial_t(\boldsymbol{\nabla}\cdot\boldsymbol{B}_1) = \boldsymbol{\nabla}\cdot[\boldsymbol{\nabla}\times(\boldsymbol{u}_1\times\boldsymbol{B}_0)] = 0. \tag{78}$$

Consequently, an initially divergence-free perturbation remains divergence-free, $\boldsymbol{\nabla}\cdot\boldsymbol{B}_1 = 0$.

Linearized momentum

For the inertial term,

$$\begin{aligned}\rho\left[\partial_t\boldsymbol{u} + (\boldsymbol{u}\cdot\boldsymbol{\nabla})\boldsymbol{u}\right] = \epsilon\rho_0\partial_t\boldsymbol{u}_1 &+ \epsilon^2\left[\rho_1\partial_t\boldsymbol{u}_1 + \rho_0(\boldsymbol{u}_1\cdot\boldsymbol{\nabla})\boldsymbol{u}_1\right] \\ &+ \epsilon^3\rho_1(\boldsymbol{u}_1\cdot\boldsymbol{\nabla})\boldsymbol{u}_1.\end{aligned} \tag{79}$$

Thus self-advection and every other product of perturbations enter beyond first order. The pressure force is $-\epsilon\boldsymbol{\nabla}p_1$. Because $\boldsymbol{B}_0$ is uniform, the Lorentz force becomes

$$(\boldsymbol{\nabla}\times\boldsymbol{B})\times\boldsymbol{B} = \epsilon(\boldsymbol{\nabla}\times\boldsymbol{B}_1)\times\boldsymbol{B}_0 + \epsilon^2(\boldsymbol{\nabla}\times\boldsymbol{B}_1)\times\boldsymbol{B}_1. \tag{80}$$

Here the unsubscripted $\boldsymbol{B}$ on the left denotes the full magnetic field. Collecting the first-order terms gives

$$\rho_0\partial_t\boldsymbol{u}_1 = -\boldsymbol{\nabla}p_1 + \frac{1}{\mu_0}(\boldsymbol{\nabla}\times\boldsymbol{B}_1)\times\boldsymbol{B}_0. \tag{81}$$

For uniform $\boldsymbol{B}_0$, the identity

$$(\boldsymbol{\nabla}\times\boldsymbol{B}_1)\times\boldsymbol{B}_0 = (\boldsymbol{B}_0\cdot\boldsymbol{\nabla})\boldsymbol{B}_1 - \boldsymbol{\nabla}(\boldsymbol{B}_0\cdot\boldsymbol{B}_1) \tag{82}$$

separates magnetic tension from magnetic pressure. Equation (81) then becomes

$$\boxed{\rho_0\partial_t\boldsymbol{u}_1 = -\boldsymbol{\nabla}\left(p_1 + \frac{\boldsymbol{B}_0\cdot\boldsymbol{B}_1}{\mu_0}\right) + \frac{1}{\mu_0}(\boldsymbol{B}_0\cdot\boldsymbol{\nabla})\boldsymbol{B}_1.} \tag{83}$$

The gradient contains the plasma-pressure and magnetic-pressure perturbations; the last term supplies magnetic tension along the equilibrium field.

Plane-wave algebraic system

Applying (64) to every first-order MHD variable gives

$$(\rho_1, p_1, \boldsymbol{u}_1, \boldsymbol{B}_1) = (\widehat{\rho}_1, \widehat{p}_1, \widehat{\boldsymbol{u}}_1, \widehat{\boldsymbol{B}}_1)e^{i(\boldsymbol{k}\cdot\boldsymbol{x}-\omega t)}.$$

The linear partial differential equations reduce to

$$-\omega\widehat{\rho}_1 + \rho_0 \boldsymbol{k}\cdot\widehat{\boldsymbol{u}}_1 = 0, \qquad \widehat{p}_1 = c_s^2\widehat{\rho}_1, \tag{84}$$

$$-\omega\widehat{\boldsymbol{B}}_1 = \boldsymbol{k}\times(\widehat{\boldsymbol{u}}_1\times\boldsymbol{B}_0), \qquad \boldsymbol{k}\cdot\widehat{\boldsymbol{B}}_1 = 0, \tag{85}$$

$$-\omega\rho_0\widehat{\boldsymbol{u}}_1 = -\boldsymbol{k}\widehat{p}_1 + \frac{1}{\mu_0}(\boldsymbol{k}\times\widehat{\boldsymbol{B}}_1)\times\boldsymbol{B}_0. \tag{86}$$

These equations form a closed algebraic system for $(\widehat{\rho}_1, \widehat{p}_1, \widehat{\boldsymbol{u}}_1, \widehat{\boldsymbol{B}}_1)$. Eliminating the density, pressure, and magnetic-field amplitudes will leave a 3×3 eigenvalue problem for $\widehat{\boldsymbol{u}}_1$.

Pressure and magnetic-field elimination

Multiplying (86) by $-\omega$ puts the momentum equation in the required $\omega^2\widehat{\boldsymbol{u}}_1$ form,

$$\omega^2\rho_0\widehat{\boldsymbol{u}}_1 = \omega\boldsymbol{k}\widehat{p}_1 - \frac{\omega}{\mu_0}(\boldsymbol{k}\times\widehat{\boldsymbol{B}}_1)\times\boldsymbol{B}_0. \tag{87}$$

Continuity and the closure give

$$\widehat{p}_1 = c_s^2\widehat{\rho}_1 = \frac{\rho_0 c_s^2}{\omega}\,\boldsymbol{k}\cdot\widehat{\boldsymbol{u}}_1. \tag{88}$$

The pressure term in (87) therefore becomes

$$\omega\boldsymbol{k}\widehat{p}_1 = \rho_0 c_s^2\boldsymbol{k}(\boldsymbol{k}\cdot\widehat{\boldsymbol{u}}_1) = \rho_0 c_s^2(\boldsymbol{k}\otimes\boldsymbol{k})\cdot\widehat{\boldsymbol{u}}_1. \tag{89}$$

The induction equation requires one vector identity,

$$\boldsymbol{k}\times(\widehat{\boldsymbol{u}}_1\times\boldsymbol{B}_0) = (\boldsymbol{k}\cdot\boldsymbol{B}_0)\widehat{\boldsymbol{u}}_1 - (\boldsymbol{k}\cdot\widehat{\boldsymbol{u}}_1)\boldsymbol{B}_0, \tag{90}$$

and hence

$$\widehat{\boldsymbol{B}}_1 = -\frac{1}{\omega}\left[(\boldsymbol{k}\cdot\boldsymbol{B}_0)\widehat{\boldsymbol{u}}_1 - (\boldsymbol{k}\cdot\widehat{\boldsymbol{u}}_1)\boldsymbol{B}_0\right]. \tag{91}$$

To reconstruct the Lorentz force explicitly, first use

$$(\boldsymbol{k}\times\widehat{\boldsymbol{B}}_1)\times\boldsymbol{B}_0 = \widehat{\boldsymbol{B}}_1(\boldsymbol{k}\cdot\boldsymbol{B}_0) - \boldsymbol{k}(\widehat{\boldsymbol{B}}_1\cdot\boldsymbol{B}_0). \tag{92}$$

Substitution of (91) into the two terms on the right-hand side gives

$$\omega\widehat{\boldsymbol{B}}_1(\boldsymbol{k}\cdot\boldsymbol{B}_0) = -\left[(\boldsymbol{k}\cdot\boldsymbol{B}_0)^2\widehat{\boldsymbol{u}}_1 - (\boldsymbol{k}\cdot\boldsymbol{B}_0)(\boldsymbol{k}\cdot\widehat{\boldsymbol{u}}_1)\boldsymbol{B}_0\right], \tag{93}$$

$$\omega\boldsymbol{k}(\widehat{\boldsymbol{B}}_1\cdot\boldsymbol{B}_0) = -\left[(\boldsymbol{k}\cdot\boldsymbol{B}_0)(\widehat{\boldsymbol{u}}_1\cdot\boldsymbol{B}_0)\boldsymbol{k} - B_0^2(\boldsymbol{k}\cdot\widehat{\boldsymbol{u}}_1)\boldsymbol{k}\right]. \tag{94}$$

Combining them in the precise form that appears in (87) yields

$$\begin{aligned} -\omega(\boldsymbol{k}\times\widehat{\boldsymbol{B}}_1)\times\boldsymbol{B}_0 = {} & (\boldsymbol{k}\cdot\boldsymbol{B}_0)^2\widehat{\boldsymbol{u}}_1 - (\boldsymbol{k}\cdot\boldsymbol{B}_0)(\boldsymbol{k}\cdot\widehat{\boldsymbol{u}}_1)\boldsymbol{B}_0 \\ & - (\boldsymbol{k}\cdot\boldsymbol{B}_0)(\widehat{\boldsymbol{u}}_1\cdot\boldsymbol{B}_0)\boldsymbol{k} + B_0^2(\boldsymbol{k}\cdot\widehat{\boldsymbol{u}}_1)\boldsymbol{k}. \end{aligned} \tag{95}$$

Velocity eigenvalue problem

With the equilibrium field direction $\widehat{\boldsymbol{b}}_0 = \boldsymbol{B}_0/B_0$, the parallel wavenumber $k_\parallel = \boldsymbol{k}\cdot\widehat{\boldsymbol{b}}_0$, and the Alfvén speed $v_\mathrm{A} = B_0/\sqrt{\mu_0\rho_0}$, substituting (89) and (95) into (87) and dividing by ρ_0 gives

$$\begin{aligned}\omega^2\widehat{\boldsymbol{u}}_1 = {}& (c_s^2+v_\mathrm{A}^2)\boldsymbol{k}(\boldsymbol{k}\cdot\widehat{\boldsymbol{u}}_1) + v_\mathrm{A}^2 k_\parallel^2\widehat{\boldsymbol{u}}_1 \\ & - v_\mathrm{A}^2 k_\parallel\left[\widehat{\boldsymbol{b}}_0(\boldsymbol{k}\cdot\widehat{\boldsymbol{u}}_1) + \boldsymbol{k}(\widehat{\boldsymbol{b}}_0\cdot\widehat{\boldsymbol{u}}_1)\right].\end{aligned} \tag{96}$$

Equivalently,

$$\boxed{\omega^2\widehat{\boldsymbol{u}}_1 = \mathsf{M}(\boldsymbol{k})\cdot\widehat{\boldsymbol{u}}_1,} \qquad \mathsf{M}(\boldsymbol{k}) = (c_s^2+v_\mathrm{A}^2)\boldsymbol{k}\otimes\boldsymbol{k} + v_\mathrm{A}^2k_\parallel^2\mathsf{I} - v_\mathrm{A}^2k_\parallel\left(\widehat{\boldsymbol{b}}_0\otimes\boldsymbol{k} + \boldsymbol{k}\otimes\widehat{\boldsymbol{b}}_0\right), \tag{97}$$

where I denotes the identity tensor. The two dyadic products in parentheses occur as a symmetric pair, so M is real and symmetric for real $\boldsymbol{k}$.

Choosing the z axis along the equilibrium field gives $\boldsymbol{B}_0 = B_0\hat{\boldsymbol{z}}$ and $\widehat{\boldsymbol{b}}_0 = \hat{\boldsymbol{z}}$. Rotational symmetry about $\boldsymbol{B}_0$ places the wavevector in the x–z plane,

$$\boldsymbol{k} = (k_\perp, 0, k_\parallel), \qquad k^2 = k_\perp^2 + k_\parallel^2. \tag{98}$$

In this basis, (91) becomes

$$\widehat{\boldsymbol{B}}_1 = \frac{B_0}{\omega}\begin{pmatrix} -k_\parallel\widehat{u}_{1x} \\ -k_\parallel\widehat{u}_{1y} \\ k_\perp\widehat{u}_{1x}\end{pmatrix}, \tag{99}$$

and the velocity eigenvalue problem is

$$\omega^2\begin{pmatrix}\widehat{u}_{1x}\\ \widehat{u}_{1y}\\ \widehat{u}_{1z}\end{pmatrix} = \begin{pmatrix}(c_s^2+v_\mathrm{A}^2)k_\perp^2 + v_\mathrm{A}^2k_\parallel^2 & 0 & c_s^2k_\perp k_\parallel \\ 0 & v_\mathrm{A}^2k_\parallel^2 & 0 \\ c_s^2k_\perp k_\parallel & 0 & c_s^2k_\parallel^2\end{pmatrix}\begin{pmatrix}\widehat{u}_{1x}\\ \widehat{u}_{1y}\\ \widehat{u}_{1z}\end{pmatrix}. \tag{100}$$

The y polarization decouples immediately. The remaining x and z components mix compression across and along the equilibrium field.

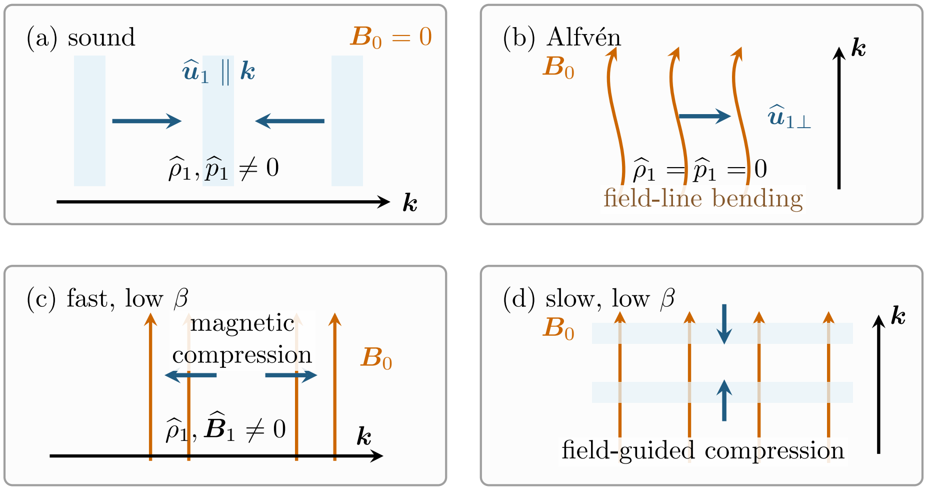

Figure 5. The wave eigenvectors identify the restoring physics. Sound moves longitudinally and compresses the plasma without a magnetic field. The Alfvén mode bends field lines without changing density or plasma pressure. The fast and slow panels show representative low-β limits. The fast mode compresses the magnetic field mainly across $\boldsymbol{B}_0$, whereas the slow mode produces a field-guided compression. Oblique propagation mixes the two in-plane velocity components according to (110).

4.4 Ideal-MHD eigenmodes and their restoring forces

Alfvén mode restored by transverse magnetic tension

The y row of (100) contains only one velocity component,

$$\omega^2 \widehat{u}_{1y} = v_\mathrm{A}^2 k_\parallel^2 \widehat{u}_{1y}. \tag{101}$$

For a nonzero transverse amplitude, the Alfvén dispersion relation and velocity eigenvector are

$$\boxed{\omega = \pm v_\mathrm{A} k_\parallel,} \qquad \widehat{\boldsymbol{u}}_1 = \widehat{u}_{1y} \hat{\boldsymbol{y}}. \tag{102}$$

Because both $\boldsymbol{k}$ and $\boldsymbol{B}_0$ lie in the x–z plane,

$$\boldsymbol{k} \cdot \widehat{\boldsymbol{u}}_1 = 0, \qquad \widehat{\boldsymbol{u}}_1 \cdot \boldsymbol{B}_0 = 0. \tag{103}$$

Continuity and the closure then show explicitly that the Alfvén wave is incompressible.

$$\widehat{\rho}_1 = \frac{\rho_0}{\omega} \boldsymbol{k} \cdot \widehat{\boldsymbol{u}}_1 = 0, \qquad \widehat{p}_1 = c_s^2 \widehat{\rho}_1 = 0. \tag{104}$$

Equation (91) reduces to

$$\widehat{\boldsymbol{B}}_1 = -\frac{\boldsymbol{k} \cdot \boldsymbol{B}_0}{\omega} \widehat{\boldsymbol{u}}_1 = \mp \frac{B_0}{v_\mathrm{A}} \widehat{\boldsymbol{u}}_1, \tag{105}$$

so the magnetic and velocity perturbations are parallel or antiparallel. In velocity units,

$$\boxed{\frac{\widehat{\boldsymbol{B}}_1}{\sqrt{\mu_0 \rho_0}} = \mp \widehat{\boldsymbol{u}}_1.} \tag{106}$$

This relation anticipates the Elsasser variables of MHD turbulence. Moreover, $\boldsymbol{B}_0 \cdot \widehat{\boldsymbol{B}}_1 = 0$, so both the plasma-pressure and magnetic-pressure perturbations vanish. Magnetic tension is therefore the only restoring force.

Fast and slow modes from coupled compression

The remaining velocity lies in the plane spanned by $\boldsymbol{k}$ and $\boldsymbol{B}_0$. The x and z rows of (100) give the reduced problem

$$\begin{pmatrix} (c_s^2 + v_{\mathrm{A}}^2)k_\perp^2 + v_{\mathrm{A}}^2 k_\parallel^2 & c_s^2 k_\perp k_\parallel \\ c_s^2 k_\perp k_\parallel & c_s^2 k_\parallel^2 \end{pmatrix} \begin{pmatrix} \widehat{u}_{1x} \\ \widehat{u}_{1z} \end{pmatrix} = \omega^2 \begin{pmatrix} \widehat{u}_{1x} \\ \widehat{u}_{1z} \end{pmatrix}. \tag{107}$$

Setting the determinant of this 2×2 system to zero gives

$$\omega^4 - k^2(c_s^2 + v_{\mathrm{A}}^2)\omega^2 + c_s^2 v_{\mathrm{A}}^2 k^2 k_\parallel^2 = 0. \tag{108}$$

This quartic is a quadratic in $X = \omega^2$. The quadratic formula gives

$$\boxed{\omega^2 = k^2 c_\pm^2, \qquad c_\pm^2 = \frac{1}{2}\left[c_s^2 + v_{\mathrm{A}}^2 \pm \sqrt{(c_s^2 + v_{\mathrm{A}}^2)^2 - 4c_s^2 v_{\mathrm{A}}^2 \cos^2\theta}\right],} \tag{109}$$

where θ denotes the angle between $\boldsymbol{k}$ and $\boldsymbol{B}_0$, so $\cos\theta = k_\parallel/k$. The plus sign defines the fast speed $c_f = c_+$; the minus sign defines the slow speed $c_{\mathrm{slow}} = c_-$.

Either row of (107) fixes the velocity polarization. Using the second row and then continuity gives

$$\frac{\widehat{u}_{1z}}{\widehat{u}_{1x}} = \frac{c_s^2 k_\perp k_\parallel}{\omega^2 - c_s^2 k_\parallel^2}, \qquad \frac{\widehat{\rho}_1}{\rho_0} = \frac{k_\perp \widehat{u}_{1x} + k_\parallel \widehat{u}_{1z}}{\omega}, \tag{110}$$

The quantity $\boldsymbol{k} \cdot \widehat{\boldsymbol{u}}_1$ is generally nonzero, so $\widehat{\rho}_1 \neq 0$ and $\widehat{p}_1 \neq 0$, so both modes compress the plasma. Equation (91) then reconstructs the magnetic fluctuation,

$$\widehat{\boldsymbol{B}}_1 = -\frac{\boldsymbol{k} \cdot \boldsymbol{B}_0}{\omega}\widehat{\boldsymbol{u}}_1 + \frac{\boldsymbol{k} \cdot \widehat{\boldsymbol{u}}_1}{\omega}\boldsymbol{B}_0. \tag{111}$$

The first term follows field-line bending by the velocity perturbation, while the second records compression of the equilibrium field. Consequently, magnetosonic waves draw their restoring force from a combination of plasma pressure, magnetic pressure, and magnetic tension.

Mode	Main polarization	Restoring force	Characteristic limit
Sound	$\widehat{\boldsymbol{u}}_1 \parallel \boldsymbol{k}$	plasma-pressure gradient	$\omega = \pm c_s k$
Alfvén	$\widehat{\boldsymbol{u}}_1 \perp \boldsymbol{k}, \boldsymbol{B}_0$	magnetic tension	$\omega = \pm v_{\mathrm{A}} k_\parallel$
Fast	compressive, in $(\boldsymbol{k}, \boldsymbol{B}_0)$ plane	plasma and magnetic forces act mostly together	$c_f \to \max(c_s, v_{\mathrm{A}})$ for parallel propagation
Slow	compressive, field-guided	plasma and magnetic forces partly oppose	$c_{\mathrm{slow}} \to \min(c_s, v_{\mathrm{A}})$ for parallel propagation

Propagation-angle and plasma-beta limits

For parallel propagation, $\theta = 0$ and $k_\parallel = k$, so

$$c_f^2 = \max(c_s^2, v_{\mathrm{A}}^2), \qquad c_{\mathrm{slow}}^2 = \min(c_s^2, v_{\mathrm{A}}^2). \tag{112}$$

The fast label follows whichever of the acoustic or magnetic responses is faster; the slow label follows the weaker response. For perpendicular propagation, $\theta = \pi/2$ and $k_\parallel = 0$, so

$$c_f^2 = c_s^2 + v_{\mathrm{A}}^2, \qquad \omega_{\mathrm{slow}} = 0. \tag{113}$$

The zero-frequency limit must be read from the original linear equations rather than from formulas obtained after division by ω. With $\partial_t = 0$ and $\boldsymbol{B}_0 \cdot \boldsymbol{\nabla} = 0$, (83) gives

$$\boldsymbol{\nabla}\left(p_1 + \frac{\boldsymbol{B}_0 \cdot \boldsymbol{B}_1}{\mu_0}\right) = 0. \tag{114}$$

The perpendicular slow branch is therefore a non-propagating, total-pressure-balanced structure.

The equilibrium plasma beta is

$$\beta = \frac{2\mu_0 p_0}{B_0^2}. \tag{115}$$

For an ideal adiabatic plasma, $c_s^2 = \gamma p_0/\rho_0$, and therefore

$$\frac{c_s^2}{v_\mathrm{A}^2} = \frac{\gamma\beta}{2}. \tag{116}$$

In the low-beta limit, $v_\mathrm{A} \gg c_s$,

$$\omega_f^2 \simeq v_\mathrm{A}^2 k^2, \qquad \omega_\mathrm{slow}^2 \simeq c_s^2 k_\parallel^2. \tag{117}$$

The fast wave is predominantly magnetic and propagates in every direction, while the slow wave behaves as a field-guided acoustic response. In the high-beta limit, $c_s \gg v_\mathrm{A}$,

$$\omega_f^2 \simeq c_s^2 k^2, \qquad \omega_\mathrm{slow}^2 \simeq v_\mathrm{A}^2 k_\parallel^2. \tag{118}$$

The fast wave becomes sound-like, while the slow wave becomes a weaker, field-guided magnetic response.

Restoring the entropy equation adds the seventh ideal-MHD characteristic, a zero-frequency entropy disturbance in this static frame, alongside the $\pm$ fast, $\pm$ Alfvén, and $\pm$ slow characteristics. Sections 1.8–1.8.2 of Spruit (2013) provide diagrams and physical limits for all three MHD wave families. Chapter 5, Sections 5.2.1–5.3.3 of Goedbloed et al. (2019) give the velocity reduction, dispersion relations, polarizations, and phase/group diagrams.

> **A useful check.** Which three questions identify the physics of a wave before calculating a determinant? What moves? What stores the potential energy? In which direction can information propagate? The polarization usually reveals the restoring force.

5 Rayleigh–Taylor instability with heavy plasma over light plasma

A stable wave oscillates because a restoring force returns a displacement toward equilibrium. An instability instead draws energy from its background and amplifies the displacement. The Rayleigh–Taylor instability provides a particularly simple example. Supporting a heavier plasma above a lighter plasma stores gravitational potential energy.

5.1 A heavy plasma above a light plasma

The simplest calculation considers two semi-infinite, incompressible, inviscid, and unmagnetized plasmas initially at rest, with no surface tension at their interface. The unperturbed interface lies at $z = 0$, gravity is $\boldsymbol{g} = -g\hat{\boldsymbol{z}}$ with $g > 0$, and the constant densities are

$$\rho_0(z) = \begin{cases} \rho_\mathrm{h}, & z > 0, \\ \rho_\mathrm{l}, & z < 0, \end{cases} \qquad \rho_\mathrm{h} > \rho_\mathrm{l}. \tag{119}$$

The subscripts h and l denote the heavy upper plasma and light lower plasma, respectively. The background pressure $p_{0j}(z)$ in either plasma $j \in \{\mathrm{h}, \mathrm{l}\}$ obeys hydrostatic balance,

$$\frac{\mathrm{d}p_{0j}}{\mathrm{d}z} = -\rho_j g. \tag{120}$$

A small vertical displacement of the interface takes the normal-mode form

$$\xi(x,t) = \widehat{\xi}\, e^{i(kx-\omega t)}, \qquad k > 0. \tag{121}$$

Here ξ is the displacement, $\widehat{\xi}$ its complex amplitude, k the horizontal wavenumber, and ω the complex frequency. Because the time dependence is $e^{-i\omega t}$, a root with $\operatorname{Im}\omega > 0$ grows exponentially.

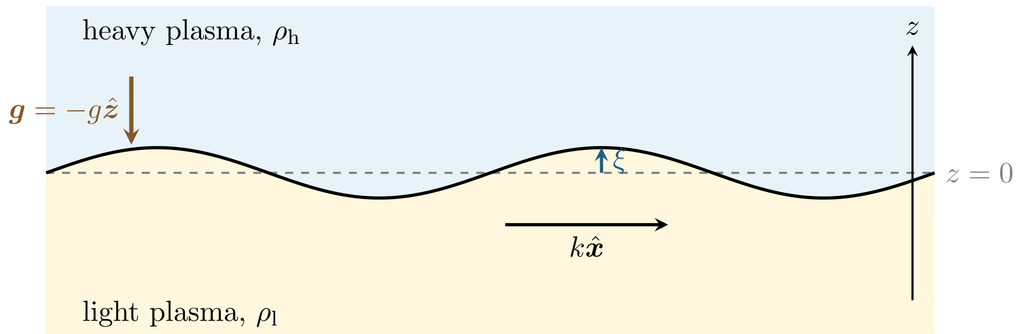

Figure 6. The simplest Rayleigh–Taylor problem. A motionless heavy plasma of density ρ_h lies above a motionless light plasma of density ρ_l in the gravitational field $\boldsymbol{g} = -g\hat{\boldsymbol{z}}$. The interface displacement ξ varies horizontally with wavevector $k\hat{\boldsymbol{x}}$.

The calculation asks whether gravity returns the ripple toward $z = 0$ or amplifies it. Both plasmas must follow the same moving interface, and their pressures must agree at the displaced interface. These two boundary conditions determine ω.

5.2 Incompressibility fixes the perturbation flow

The calculation considers perturbations that remain irrotational within each uniform half-space. Writing $\boldsymbol{u}'_j = \boldsymbol{\nabla}\phi_j$ automatically gives zero perturbation vorticity. Incompressibility then requires

$$\boldsymbol{\nabla} \cdot \boldsymbol{u}'_j = \nabla^2 \phi_j = 0. \tag{122}$$

The normal-mode ansatz separates the vertical dependence from the common horizontal and temporal factors,

$$\phi_j(x,z,t) = \widetilde{\phi}_j(z) e^{i(kx-\omega t)}, \qquad k > 0. \tag{123}$$

The calculation is two-dimensional, so $\nabla^2 = \partial_x^2 + \partial_z^2$. Substitution into (122) gives

$$\begin{aligned} 0 &= (\partial_x^2 + \partial_z^2)\left[\widetilde{\phi}_j(z) e^{i(kx-\omega t)}\right] \\ &= \left[(ik)^2 \widetilde{\phi}_j + \frac{\mathrm{d}^2\widetilde{\phi}_j}{\mathrm{d}z^2}\right] e^{i(kx-\omega t)} \\ &= \left(\frac{\mathrm{d}^2\widetilde{\phi}_j}{\mathrm{d}z^2} - k^2 \widetilde{\phi}_j\right) e^{i(kx-\omega t)}. \end{aligned} \tag{124}$$

The exponential factor never vanishes, so the vertical amplitude obeys

$$\left(\frac{\mathrm{d}^2}{\mathrm{d}z^2} - k^2\right)\widetilde{\phi}_j = 0. \tag{125}$$

Trying $\widetilde{\phi}_j \propto e^{mz}$ gives the characteristic equation $m^2 - k^2 = 0$, with roots $m = \pm k$. The general vertical solution in either plasma is therefore

$$\widetilde{\phi}_j(z) = C_j^+ e^{kz} + C_j^- e^{-kz}, \tag{126}$$

where C_j^+ and C_j^- are constants. In the upper half-space $z > 0$, boundedness as $z \to +\infty$ removes e^{+kz}. In the lower half-space $z < 0$, boundedness as $z \to -\infty$ removes e^{-kz}. Consequently,

$$\begin{aligned} \phi_{\mathrm{h}} &= A_{\mathrm{h}} e^{-kz} e^{i(kx-\omega t)}, \quad z > 0, \\ \phi_{\mathrm{l}} &= A_{\mathrm{l}} e^{+kz} e^{i(kx-\omega t)}, \quad z < 0. \end{aligned} \tag{127}$$

The constants A_{h} and A_{l} are velocity-potential amplitudes. The vertical e-folding depth is k^{-1}, while the horizontal wavelength is $\lambda = 2\pi/k$; the two lengths therefore differ only by the factor 2π.

The interface must move with the vertical velocity of each plasma. The kinematic boundary condition is therefore

$$\partial_t \xi = \partial_z \phi_{\mathrm{h}}\big|_{z=0}, \qquad \partial_t \xi = \partial_z \phi_{\mathrm{l}}\big|_{z=0}. \tag{128}$$

Using the normal modes in (121) and (127) gives

$$\begin{aligned} -i\omega\widehat{\xi} &= -kA_{\mathrm{h}}, & -i\omega\widehat{\xi} &= +kA_{\mathrm{l}}, \\ A_{\mathrm{h}} &= \frac{i\omega}{k}\widehat{\xi}, & A_{\mathrm{l}} &= -\frac{i\omega}{k}\widehat{\xi}. \end{aligned} \tag{129}$$

5.3 Pressure continuity selects a growing mode

After hydrostatic balance removes the equilibrium forces, the linearized momentum equation in either plasma is

$$\rho_j \partial_t \boldsymbol{\nabla}\phi_j = -\boldsymbol{\nabla} p_j', \tag{130}$$

where p_j' is the Eulerian pressure perturbation. Because ρ_j is constant, (130) can be written as

$$\boldsymbol{\nabla}\left(\rho_j \partial_t \phi_j + p_j'\right) = 0. \tag{131}$$

The quantity in parentheses can depend on time but not on position. A time-dependent shift of ϕ_j absorbs that spatially uniform term, leaving the linearized Bernoulli relation

$$p_j' = -\rho_j \partial_t \phi_j. \tag{132}$$

Writing the pressure at the interface as $p_j'(x,0,t) = \widehat{p}_j e^{i(kx-\omega t)}$, substitution of (129) gives

$$\widehat{p}_{\mathrm{h}} = -\frac{\rho_{\mathrm{h}}\omega^2}{k}\widehat{\xi}, \qquad \widehat{p}_{\mathrm{l}} = +\frac{\rho_{\mathrm{l}}\omega^2}{k}\widehat{\xi}. \tag{133}$$

Pressure continuity must hold at the displaced surface $z = \xi$, not at the original surface $z = 0$. Expanding the total pressure to first order gives

$$p_{0\mathrm{h}}(0) + \xi\frac{\mathrm{d}p_{0\mathrm{h}}}{\mathrm{d}z} + p_{\mathrm{h}}'(x,0,t) = p_{0\mathrm{l}}(0) + \xi\frac{\mathrm{d}p_{0\mathrm{l}}}{\mathrm{d}z} + p_{\mathrm{l}}'(x,0,t). \tag{134}$$

The shift of the perturbation pressure would contribute $\xi\,\partial_z p'_j$, a product of two first-order quantities, so it does not enter the linear boundary condition. The equilibrium pressure is continuous at $z = 0$. Using hydrostatic balance from (120) and removing the common normal-mode factor therefore reduces (134) to

$$\widehat{p}_{\mathrm{h}} - \widehat{p}_{\mathrm{l}} = g(\rho_{\mathrm{h}} - \rho_{\mathrm{l}})\widehat{\xi}. \tag{135}$$

Substitution of (133) yields

$$-\frac{\rho_{\mathrm{h}} + \rho_{\mathrm{l}}}{k}\omega^2\widehat{\xi} = g(\rho_{\mathrm{h}} - \rho_{\mathrm{l}})\widehat{\xi}. \tag{136}$$

Defining the dimensionless Atwood number

$$A = \frac{\rho_{\mathrm{h}} - \rho_{\mathrm{l}}}{\rho_{\mathrm{h}} + \rho_{\mathrm{l}}}, \qquad 0 < A < 1, \tag{137}$$

gives the dispersion relation and its two roots.

$$\boxed{\omega^2 = -Agk}, \qquad\qquad \omega = \pm i\sqrt{Agk}. \tag{138}$$

The positive-imaginary root grows as $e^{\gamma_{\mathrm{RT}} t}$ with

$$\boxed{\gamma_{\mathrm{RT}} = \sqrt{Agk}.} \tag{139}$$

The sign contains the physics. Interchanging heavy material above with light material below lowers the gravitational potential energy, so gravity drives the displacement instead of restoring it. The limit $A \to 0$ removes the density contrast and the instability, whereas $A \to 1$ describes an upper plasma much denser than the lower one. The ideal discontinuous interface contains no short length scale, so $\gamma_{\mathrm{RT}} \propto k^{1/2}$ increases without bound. A finite density-transition width, viscosity, surface tension, or magnetic tension changes this short-wavelength prediction. Appendix B restores arbitrary tangential velocities and magnetic fields. Chapter 3, Sections 3.5–3.7 of Drazin (2002) and Chapter X, Sections 90–92 and 97 of Chandrasekhar (1961) develop the hydrodynamic Rayleigh–Taylor problem.

A useful check. Why does a horizontal wavenumber determine the inertia of the motion? A ripple of wavenumber k moves plasma through a vertical depth of order k^{-1}. Shorter ripples therefore accelerate less mass per unit interface area, which helps explain why their ideal growth rate is larger.

Physical point. The introductory Rayleigh–Taylor calculation needs three steps. Incompressibility fixes how the perturbation decays away from the interface, the kinematic condition makes both plasmas follow the same ripple, and pressure continuity at the displaced surface gives $\omega^2 < 0$. The unstable density ordering supplies gravitational potential energy for exponential growth.

Part II

Hydrodynamic turbulence

The wave and instability calculations above stop at first order, where Fourier modes evolve independently. Turbulence begins with the discarded self-advection term. It couples modes, stretches vorticity, and transfers kinetic energy from large motions to much smaller scales.

6 Navier–Stokes dynamics and the creation of small scales

Momentum conservation at constant density, together with incompressibility, isolates a central turbulence question of how self-advection can conserve the total kinetic energy while creating the gradients required for viscous dissipation?

6.1 Incompressible competition between inertia and viscosity

The model treats a Newtonian plasma of constant mass density ρ and kinematic viscosity ν. The fields $\boldsymbol{u}(\boldsymbol{x}, t)$ and $p(\boldsymbol{x}, t)$ denote velocity and pressure at position $\boldsymbol{x}$ and time t. An external acceleration $\boldsymbol{f}(\boldsymbol{x}, t)$ injects or removes momentum and energy. The incompressible Navier–Stokes equations are

$$\partial_t \boldsymbol{u} + \boldsymbol{u} \cdot \boldsymbol{\nabla} \boldsymbol{u} = -\frac{1}{\rho} \boldsymbol{\nabla} p + \nu \nabla^2 \boldsymbol{u} + \boldsymbol{f}, \qquad \boldsymbol{\nabla} \cdot \boldsymbol{u} = 0. \tag{140}$$

In index notation, repeated Cartesian indices imply summation, and Equation 140 becomes

$$\partial_t u_i + u_j \partial_j u_i = -\rho^{-1} \partial_i p + \nu \partial_j \partial_j u_i + f_i, \qquad \partial_i u_i = 0. \tag{141}$$

Here u_i, f_i, and $\partial_i \equiv \partial / \partial x_i$ denote the ith components of $\boldsymbol{u}$, $\boldsymbol{f}$, and the spatial gradient, respectively.

Nondimensionalization uses a characteristic velocity U, length L, and turnover time $T = L/U$. The substitutions

$$\boldsymbol{x} = L \boldsymbol{x}^*, \qquad t = T t^*, \qquad \boldsymbol{u} = U \boldsymbol{u}^*, \qquad p = \rho U^2 p^*, \qquad \boldsymbol{f} = \frac{U^2}{L} \boldsymbol{f}^* \tag{142}$$

and division by U^2/L transform Equation 140 into

$$\partial_{t^*} \boldsymbol{u}^* + \boldsymbol{u}^* \cdot \boldsymbol{\nabla}^* \boldsymbol{u}^* = -\boldsymbol{\nabla}^* p^* + \frac{1}{\mathrm{Re}} \nabla^{*2} \boldsymbol{u}^* + \boldsymbol{f}^*, \qquad \boldsymbol{\nabla}^* \cdot \boldsymbol{u}^* = 0, \tag{143}$$

where

$$\boxed{\mathrm{Re} \equiv \frac{UL}{\nu}} \tag{144}$$

is the Reynolds number.

Numerical diffusion from an ideal equation. Discretization does not preserve continuum ideality automatically. The constant-speed advection equation

$$\partial_t q + a \, \partial_x q = 0, \qquad a > 0, \tag{145}$$

contains no physical diffusion. A first-order upwind discretization on a grid with spacing Δx and timestep Δt is

$$\frac{q_j^{n+1}-q_j^n}{\Delta t}+a\,\frac{q_j^n-q_{j-1}^n}{\Delta x}=0,\qquad C\equiv\frac{a\Delta t}{\Delta x}, \tag{146}$$

where q_j^n approximates $q(j\Delta x, n\Delta t)$ and C is the Courant number. Taylor expansion about $(j\Delta x, n\Delta t)$ gives

$$\frac{q_j^{n+1}-q_j^n}{\Delta t}=\partial_t q+\frac{\Delta t}{2}\partial_t^2 q+\cdots,\qquad\qquad \frac{q_j^n-q_{j-1}^n}{\Delta x}=\partial_x q-\frac{\Delta x}{2}\partial_x^2 q+\cdots. \tag{147}$$

The leading ideal equation implies $\partial_t^2 q = a^2\partial_x^2 q$. Substitution into Equation 147 yields the modified equation

$$\boxed{\partial_t q + a\,\partial_x q = \nu_{\rm num}\partial_x^2 q + \mathcal{O}\big(\Delta x^2\big)\,,\qquad \nu_{\rm num}\equiv\frac{a\Delta x}{2}(1-C).} \tag{148}$$

For $0 \le C < 1$, the positive numerical diffusivity $\nu_{\rm num}$ smooths variations near the grid scale. Thus this discretized ideal model solves an advection–diffusion equation to leading order. Other schemes can add higher-order diffusion, dispersion, or nonlinear grid-scale operators, so their numerical regularization need not have this exact Laplacian form.

Large Re makes physical viscous diffusion weak on the outer scale L; it does not remove viscosity from all scales because gradients steepen during the cascade. Even when the continuum model sets $\nu = 0$, a discrete calculation still modifies the smallest resolved scales through a scheme-dependent numerical operator.

The pressure does not obey an independent thermodynamic evolution equation in this incompressible system. Taking the divergence of the momentum equation and using $\partial_i u_i = 0$ gives

$$\boxed{\nabla^2 p = -\rho\,\partial_i u_j\,\partial_j u_i + \rho\,\boldsymbol{\nabla}\cdot\boldsymbol{f}.} \tag{149}$$

Pressure therefore enforces incompressibility nonlocally. It redistributes momentum and energy among directions without changing the volume-integrated kinetic energy when the boundary flux vanishes.

Chapter 2, Sections 2.4–2.5 of Pope (2000) derive the momentum and pressure equations; Chapter 2, Section 2.1 of Frisch (1995) derives their projected and vorticity forms.

> **Physical point.** The self-advection nonlinearity, $\boldsymbol{u}\cdot\boldsymbol{\nabla}\boldsymbol{u}$, contains no dimensionless coefficient. It transports energy among positions and scales, while viscosity becomes decisive only after the nonlinear dynamics have created sufficiently sharp velocity gradients.

6.2 Vortex stretching creates gradients without changing total energy

The nonlinear term conserves the volume-integrated kinetic energy under the boundary conditions introduced below. Turbulent dissipation nevertheless requires ever sharper velocity gradients. The vorticity equation reveals how the same nonlinear term creates those gradients in three dimensions.

The curl of the velocity defines the vorticity,

$$\boldsymbol{\omega}\equiv\boldsymbol{\nabla}\times\boldsymbol{u}. \tag{150}$$

Taking the curl of Equation 140 removes the pressure gradient. The identity

$$\boldsymbol{\nabla}\times(\boldsymbol{u}\cdot\boldsymbol{\nabla}\boldsymbol{u})=\boldsymbol{u}\cdot\boldsymbol{\nabla}\boldsymbol{\omega}-\boldsymbol{\omega}\cdot\boldsymbol{\nabla}\boldsymbol{u}\qquad(\boldsymbol{\nabla}\cdot\boldsymbol{u}=\boldsymbol{\nabla}\cdot\boldsymbol{\omega}=0) \tag{151}$$

gives

$$\boxed{\partial_t \boldsymbol{\omega} + \boldsymbol{u} \cdot \boldsymbol{\nabla} \boldsymbol{\omega} = \underbrace{\boldsymbol{\omega} \cdot \boldsymbol{\nabla} \boldsymbol{u}}_{\text{vortex stretching}} + \nu \nabla^2 \boldsymbol{\omega} + \boldsymbol{\nabla} \times \boldsymbol{f}.} \tag{152}$$

The velocity-gradient tensor $A_{ij} = \partial_j u_i$ separates into the symmetric strain S_{ij} and antisymmetric rotation Ω_{ij},

$$S_{ij} \equiv \frac{1}{2}(\partial_j u_i + \partial_i u_j), \qquad \Omega_{ij} \equiv \frac{1}{2}(\partial_j u_i - \partial_i u_j), \qquad A_{ij} = S_{ij} + \Omega_{ij}. \tag{153}$$

Because $\Omega_{ij}\omega_j = 0$, the stretching term is $S_{ij}\omega_j$. The material derivative

$$\frac{D}{Dt} \equiv \partial_t + \boldsymbol{u} \cdot \boldsymbol{\nabla} \tag{154}$$

follows a fluid particle. Away from viscous diffusion and rotational forcing, contraction of the vorticity equation with $\widehat{\omega}_i \equiv \omega_i / |\boldsymbol{\omega}|$ gives

$$\frac{D|\boldsymbol{\omega}|}{Dt} = |\boldsymbol{\omega}| \, \widehat{\omega}_i S_{ij} \widehat{\omega}_j. \tag{155}$$

Alignment with an extensional eigenvector of S_{ij} therefore increases $|\boldsymbol{\omega}|$, whereas alignment with a compressive eigenvector decreases it.

The geometrical meaning follows directly from the motion of two neighboring fluid particles. Let $\delta \boldsymbol{\ell}$ denote their infinitesimal separation. Subtracting their trajectory equations and retaining the term linear in $\delta \boldsymbol{\ell}$ gives

$$\frac{D \, \delta \ell_i}{Dt} = \delta \ell_j \partial_j u_i. \tag{156}$$

In the inviscid limit with $\boldsymbol{\nabla} \times \boldsymbol{f} = 0$, the vorticity equation has precisely the same form,

$$\frac{D\omega_i}{Dt} = \omega_j \partial_j u_i. \tag{157}$$

Thus the flow carries a vortex-line element like a material line element. Axial strain lengthens the line and amplifies its vorticity, while incompressibility compresses the cross-section of the associated vortex tube.

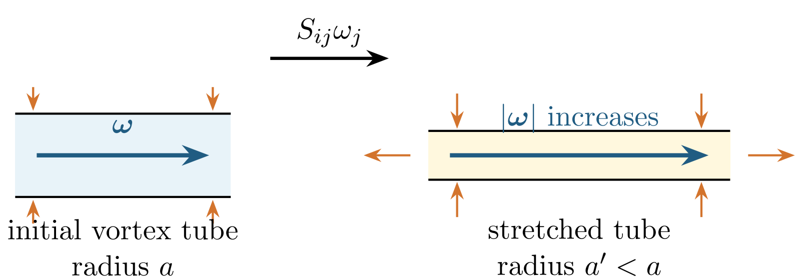

Figure 7. Strain stretches a vortex tube along its axis and compresses its cross-section. The stretching term $S_{ij}\omega_j$ can therefore amplify vorticity even when viscosity is small. The arrows normal to the tube indicate the transverse compression required by $\boldsymbol{\nabla} \cdot \boldsymbol{u} = 0$.

Squaring the vorticity makes the production of small-scale gradients explicit. The *enstrophy density* is $q_\omega \equiv |\boldsymbol{\omega}|^2/2$. Taking the scalar product of Equation 152 with $\boldsymbol{\omega}$ produces the stretching and forcing contributions directly. Antisymmetry gives $\omega_i \Omega_{ij} \omega_j = 0$, so $\omega_i \omega_j \partial_j u_i = \omega_i S_{ij} \omega_j$. The viscous contribution obeys

$$\omega_i \nabla^2 \omega_i = \nabla^2 \left(\frac{|\boldsymbol{\omega}|^2}{2} \right) - (\partial_j \omega_i)(\partial_j \omega_i) \tag{158}$$

Collecting the terms gives the local enstrophy balance

$$\boxed{\frac{D}{Dt}\left(\frac{|\boldsymbol{\omega}|^2}{2}\right) = \underbrace{\omega_i S_{ij}\omega_j}_{\text{stretching}} + \underbrace{\nu\nabla^2\left(\frac{|\boldsymbol{\omega}|^2}{2}\right)}_{\text{viscous diffusion}} - \underbrace{\nu(\partial_j\omega_i)^2}_{\text{viscous destruction}} + \underbrace{\boldsymbol{\omega}\cdot(\boldsymbol{\nabla}\times\boldsymbol{f})}_{\text{vorticity forcing}}.} \tag{159}$$

The viscous-diffusion term has conservative form $\nu\nabla^2 q_\omega = -\boldsymbol{\nabla}\cdot\boldsymbol{J}_\omega$, where $\boldsymbol{J}_\omega \equiv -\nu\boldsymbol{\nabla}q_\omega$ is the diffusive enstrophy flux. This flux redistributes enstrophy in physical space, but its volume integral reduces to a boundary flux and vanishes in a periodic domain or under zero normal diffusive flux. The stretching production $\omega_i S_{ij}\omega_j$ has no fixed sign pointwise, but it can increase enstrophy without changing the total kinetic energy. The volume average of a field $q(\boldsymbol{x},t)$ over a fixed domain $\mathcal{D}$ of positive volume $\mathcal{V}$ is

$$\langle q\rangle_{\mathcal{D}} \equiv \frac{1}{\mathcal{V}}\int_{\mathcal{D}} q(\boldsymbol{x},t)\,\mathrm{d}V. \tag{160}$$

For a periodic domain, or boundaries with vanishing advective and diffusive enstrophy fluxes, the mean enstrophy

$$\mathcal{Z} \equiv \frac{1}{2}\left\langle|\boldsymbol{\omega}|^2\right\rangle_{\mathcal{D}} \tag{161}$$

therefore obeys

$$\boxed{\frac{\mathrm{d}\mathcal{Z}}{\mathrm{d}t} = \langle\omega_i S_{ij}\omega_j\rangle_{\mathcal{D}} - \nu\left\langle(\partial_j\omega_i)^2\right\rangle_{\mathcal{D}} + \langle\boldsymbol{\omega}\cdot(\boldsymbol{\nabla}\times\boldsymbol{f})\rangle_{\mathcal{D}}.} \tag{162}$$

Here $\mathrm{d}\mathcal{Z}/\mathrm{d}t$ is the ordinary derivative of one domain-averaged quantity, whereas D/Dt in Equation 154 follows a moving fluid particle. Nonlinear advection consequently plays two complementary roles. It preserves the global kinetic energy, yet vortex stretching allows it to build the gradients that viscosity ultimately dissipates.

If a velocity field is exactly two-dimensional, $\boldsymbol{u} = (u_x, u_y, 0)$ and $\partial_z = 0$, then $\boldsymbol{\omega} = \omega_z\hat{\boldsymbol{z}}$ and $\boldsymbol{\omega}\cdot\boldsymbol{\nabla}\boldsymbol{u} = 0$. In an inviscid, unforced two-dimensional flow, $D\omega_z/Dt = 0$, and the dynamics conserve both kinetic energy and $\mathcal{Z}$. This additional invariant prevents a straightforward copy of the three-dimensional forward energy cascade. The analysis below concerns three-dimensional turbulence.

Chapter 2, Sections 2.7–2.8 of Pope (2000) develop vortex stretching, strain, and rotation. Chapter 2, Sections 2.1 and 2.3 of Frisch (1995) derive the vorticity and global enstrophy balances.

7 Kolmogorov phenomenology from flux and viscosity

Vortex stretching explains how three-dimensional advection creates progressively sharper velocity gradients. K41 turns that mechanism into a scale-by-scale estimate. The argument assumes a high-Reynolds-number, statistically stationary cascade with a scale-independent mean energy flux and then asks what dimensional analysis alone predicts. Energy budgets, the exact third-order law, and the spectral transfer equation later put those estimates on a precise footing.

7.1 Cascade ranges from injection to dissipation

Turbulent motion contains a broad range of length scales. The symbols L and U denote an energy-containing scale and its characteristic velocity, while $\tau_L = L/U$ is its turnover time. The symbol ℓ denotes a generic size of a turbulent motion, whereas r will denote the separation between two sampling points. Scale-local estimates identify $\ell \sim r$ without asserting that an individual eddy belongs uniquely to either description. The symbols u_ℓ and $\tau_\ell \equiv \ell/u_\ell$ denote the characteristic velocity and turnover time at scale ℓ, so $u_L \sim U$ and $\tau_L = L/U$ at the outer scale. The symbol ε denotes the mean kinetic-energy transfer rate per unit mass; the energy budget in section 8 derives its injection and viscous-dissipation forms. In the statistically stationary cascade considered here, those equations will show that the same rate passes through three distinct processes, namely injection at large scales, nonlinear transfer through the inertial range, and viscous dissipation at small scales. External forcing or mean-flow production supplies kinetic energy primarily at scales comparable with L. The nonlinear term transfers this energy through intermediate scales, and viscosity dissipates it near the much smaller Kolmogorov length η_{K}. The subscript K distinguishes this viscous cutoff from the magnetic diffusivity η.

If the energy transfer time at the outer scale is comparable with τ_L, the transfer rate per unit mass scales as

$$\varepsilon \sim \frac{U^2}{\tau_L} \sim \frac{U^3}{L}. \tag{163}$$

At high Reynolds number, the mean dissipation can therefore approach a finite value that does not contain ν explicitly. Viscosity still determines the terminal scale η_{K} at which the cascade deposits this energy as heat.

Vortex stretching provides a physical-space route by which the forward cascade builds small scales. The stretching contribution in Equation 162 amplifies velocity gradients while the nonlinear term preserves total kinetic energy; successive amplification brings those gradients to scales at which viscous destruction balances their production.

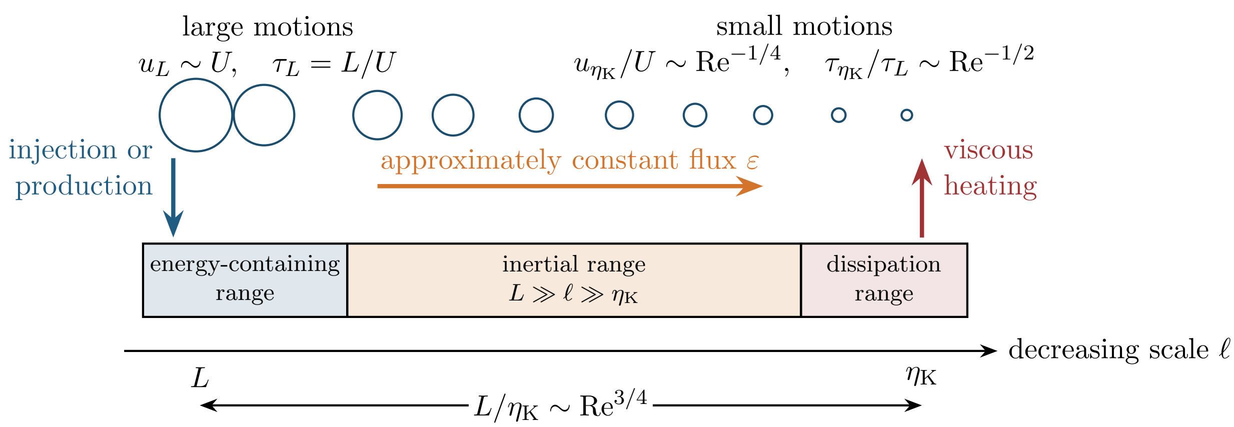

Figure 8. The three-dimensional cascade transfers kinetic energy from an energy-containing range near L, through an inertial range with nearly constant flux ε, to a dissipation range near η_{K}. The Reynolds-number annotations anticipate the scale separation derived later in this section. The spatial range grows as $\mathrm{Re}^{3/4}$, while the terminal velocity and turnover time decrease as $\mathrm{Re}^{-1/4}$ and $\mathrm{Re}^{-1/2}$, respectively. The circles indicate motions of successively smaller size; they do not imply that turbulence consists of isolated, rigid vortices.

The language of eddies provides intuition but not a unique mathematical decomposition. Velocity increments and Fourier modes give two precise, complementary ways to separate scales. Chapter 6, Sections 6.1.1–6.1.2 of Pope (2000) develop the energy-cascade picture and the Kolmogorov hypotheses. Chapter 2, Section 2.4 of Frisch (1995) constructs a scale-by-scale budget with explicit low- and high-pass filters, while Chapter 7, Sections 7.2–7.3 develop the turnover-time phenomenology and examine cascade locality.

7.2 Velocity increments turn over faster at smaller scales

K41 turns the constant-flux cascade picture into a similarity hypothesis. The exact third-order law derived later tests the flux and its sign, but dimensional phenomenology does not require that derivation as its starting point. At separations $L \gg r \gg \eta_{\mathrm{K}}$, K41 assumes that the statistics lose their dependence on forcing details and viscosity.

The separation vector, its magnitude, and its direction are

$$\boldsymbol{r} = r\hat{\boldsymbol{r}}, \qquad r \equiv |\boldsymbol{r}|, \qquad \hat{\boldsymbol{r}} \equiv \frac{\boldsymbol{r}}{r}. \tag{164}$$

For two points separated by $\boldsymbol{r}$, the signed longitudinal velocity increment is

$$\delta u_L(\boldsymbol{x}, \boldsymbol{r}, t) \equiv [\boldsymbol{u}(\boldsymbol{x}+\boldsymbol{r}, t) - \boldsymbol{u}(\boldsymbol{x}, t)] \cdot \hat{\boldsymbol{r}}. \tag{165}$$

Section 9 places this increment within the hierarchy of structure functions and probability distributions. The symbol δu_r instead denotes a characteristic magnitude at scale r, not the signed random variable δu_L.

K41 assumes that δu_r depends only on the mean energy flux ε and the separation r. Their dimensions are

$$[\delta u_r] = LT^{-1}, \qquad [\varepsilon] = L^2T^{-3}, \qquad [r] = L. \tag{166}$$

A general power-law combination of the available dimensional quantities has the form

$$\delta u_r \sim \varepsilon^a r^b. \tag{167}$$

Matching its length and time dimensions gives

$$LT^{-1} = L^{2a+b}T^{-3a}, \qquad -3a = -1, \qquad 2a + b = 1, \tag{168}$$

$$a = \frac{1}{3}, \qquad b = \frac{1}{3}. \tag{169}$$

Therefore

$$\boxed{\delta u_r \sim (\varepsilon r)^{1/3}, \qquad \tau_r \sim \frac{r}{\delta u_r} \sim \left(\frac{r^2}{\varepsilon}\right)^{1/3}.} \tag{170}$$

The smaller inertial-range motions have smaller velocity differences and shorter turnover times. Their energy flux remains independent of scale because

$$\frac{(\delta u_r)^2}{\tau_r} \sim \frac{(\delta u_r)^3}{r} \sim \varepsilon. \tag{171}$$

For the statistical quantities below, angle brackets denote an ensemble average. A statistically homogeneous and ergodic flow permits a volume or time average to estimate this ensemble average. Writing $S_p^{|\cdot|}(r) \equiv \langle|\delta u_L|^p\rangle$, if the entire probability distribution of $\delta u_L/(\varepsilon r)^{1/3}$ is independent of r, the longitudinal structure functions obey

$$S_p^{|\cdot|}(r) = C_p(\varepsilon r)^{p/3}, \qquad \zeta_p^{\mathrm{K41}} = \frac{p}{3}, \tag{172}$$

where C_p is dimensionless and the relation $S_p^{|\cdot|} \propto r^{\zeta_p}$ defines the scaling exponent ζ_p. The second-order prediction is

$$S_{2,L}(r) \equiv \left\langle(\delta u_L)^2\right\rangle = C_2(\varepsilon r)^{2/3}. \tag{173}$$

Unlike the four-fifths coefficient, C_2 does not follow from dimensional analysis.

7.3 Dimensional prediction of the $k^{-5/3}$ energy spectrum

The same dimensional argument determines the spectrum. Defining the one-dimensional spectrum by $\langle |\boldsymbol{u}|^2 \rangle /2 = \int_0^\infty E(k)\mathrm{d}k$ gives $[E] = L^3T^{-2}$. In an inertial range, the similarity hypothesis makes $E(k)$ depend only on ε and the scalar wavenumber k, whose dimensions are L^{-1}. Writing $E(k) \sim \varepsilon^a k^b$ and matching dimensions gives

$$[E] = L^3T^{-2} = (L^2T^{-3})^a L^{-b}, \qquad -3a = -2, \qquad 2a - b = 3. \tag{174}$$

This gives $a = 2/3$ and $b = -5/3$, so

$$\boxed{E(k) = C_K \varepsilon^{2/3} k^{-5/3}, \qquad L^{-1} \ll k \ll \eta_{\mathrm{K}}^{-1}.} \tag{175}$$

The dimensionless Kolmogorov constant C_K is not fixed by this argument. Wavenumbers near L^{-1} retain information about forcing and geometry, while wavenumbers near η_{K}^{-1} feel viscosity. The spectrum follows the $-5/3$ power law only between these ranges. The shorthand $k_L \equiv L^{-1}$ and $k_{\eta_{\mathrm{K}}} \equiv \eta_{\mathrm{K}}^{-1}$ denotes the corresponding outer and dissipative wavenumbers.

Chapter 6, Sections 6.1.2–6.1.4, 6.2, and 6.5.2 of Pope (2000) develop the Kolmogorov hypotheses, structure-function scaling, and the Kolmogorov spectrum. Chapter 6, Section 6.3.1 of Frisch (1995) presents the K41 structure functions and spectrum.

7.4 Kolmogorov scales at unit local Reynolds number

The inertial-range estimate cannot continue to arbitrarily small scales. Viscosity becomes competitive when the local Reynolds number reaches order unity, selecting the terminal length, velocity, and time scales of the K41 cascade.

In the dissipative range, both the mean flux ε and the kinematic viscosity ν can enter. Writing $\eta_{\mathrm{K}} = \nu^a \varepsilon^b$ identifies the unique length built from them. Because $[\nu] = L^2T^{-1}$ and $[\varepsilon] = L^2T^{-3}$, dimensional matching gives

$$2a + 2b = 1, \qquad -a - 3b = 0, \qquad a = \frac{3}{4}, \qquad b = -\frac{1}{4}. \tag{176}$$

Repeating the calculation for a velocity and a time, or combining η_{K}, ν, and ε, gives the Kolmogorov scales

$$\boxed{\eta_{\mathrm{K}} = \left(\frac{\nu^3}{\varepsilon}\right)^{1/4}, \qquad u_{\eta_{\mathrm{K}}} = (\nu\varepsilon)^{1/4}, \qquad \tau_{\eta_{\mathrm{K}}} = \left(\frac{\nu}{\varepsilon}\right)^{1/2}.} \tag{177}$$

They satisfy

$$\frac{u_{\eta_{\mathrm{K}}}\eta_{\mathrm{K}}}{\nu} = 1, \qquad \frac{u_{\eta_{\mathrm{K}}}}{\eta_{\mathrm{K}}} = \tau_{\eta_{\mathrm{K}}}^{-1}, \qquad \nu\left(\frac{u_{\eta_{\mathrm{K}}}}{\eta_{\mathrm{K}}}\right)^2 = \varepsilon. \tag{178}$$

Thus the local Reynolds number becomes order unity at η_{K}, and gradients of order $u_{\eta_{\mathrm{K}}}/\eta_{\mathrm{K}}$ dissipate energy at the cascade rate.

Chapter 6, Section 6.1.2 of Pope (2000) derives these scales, and Section 6.5.4 develops the dissipation spectrum. Chapter 6, Section 6.3.2 of Frisch (1995) derives the dissipative cutoff.

7.5 Growth of the inertial range with Reynolds number

Combining $\varepsilon \sim U^3/L$ with Equation 177 and $\mathrm{Re} = UL/\nu$ gives

$$\frac{\eta_\mathrm{K}}{L} = \frac{1}{L}\left(\frac{\nu^3 L}{U^3}\right)^{1/4} = \left(\frac{\nu}{UL}\right)^{3/4} = \mathrm{Re}^{-3/4}, \tag{179}$$

$$\frac{u_{\eta_\mathrm{K}}}{U} = \frac{(\nu U^3/L)^{1/4}}{U} = \mathrm{Re}^{-1/4}, \qquad \frac{\tau_{\eta_\mathrm{K}}}{\tau_L} = \frac{(\nu L/U^3)^{1/2}}{L/U} = \mathrm{Re}^{-1/2}. \tag{180}$$

Increasing Re widens the scale interval $L/\eta_\mathrm{K} \sim \mathrm{Re}^{3/4}$ and shortens the fastest turnover time relative to τ_L. A three-dimensional direct numerical simulation that resolves η_K throughout a box of size L therefore needs at least

$$N_\mathrm{space} \sim \left(\frac{L}{\eta_\mathrm{K}}\right)^3 \sim \mathrm{Re}^{9/4} \tag{181}$$

spatial degrees of freedom even before accounting for the increasingly small time step. Section 7.4 of Frisch (1995) derives the same scale-separation and spatial-cost estimates and discusses the assumptions behind interpreting $\mathrm{Re}^{9/4}$ as a number of turbulent degrees of freedom.

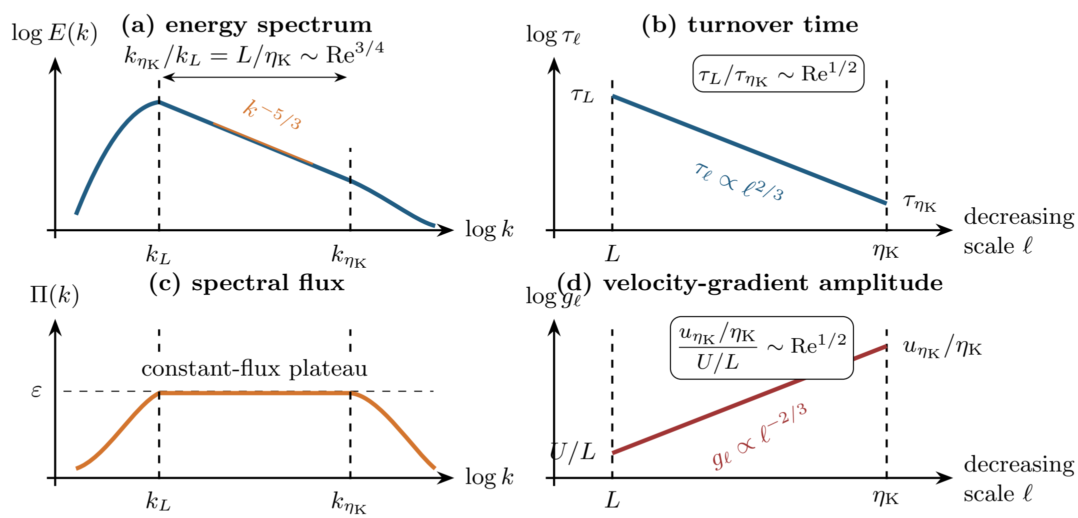

Figure 9. The left panels show the inertial-range $k^{-5/3}$ spectrum and corresponding positive spectral-flux plateau between k_L and k_{η_K}. The right panels use $\tau_\ell \sim (\ell^2/\varepsilon)^{1/3}$ and $g_\ell \equiv \delta u_\ell/\ell \sim \varepsilon^{1/3}\ell^{-2/3}$ to show that smaller motions turn over faster and carry larger velocity gradients. The Reynolds-number annotations connect these scale trends to section 7. The relations are $L/\eta_\mathrm{K} \sim \mathrm{Re}^{3/4}$, $\tau_L/\tau_{\eta_\mathrm{K}} \sim \mathrm{Re}^{1/2}$, and $(u_{\eta_\mathrm{K}}/\eta_\mathrm{K})/(U/L) \sim \mathrm{Re}^{1/2}$. Curved spectral transitions emphasize that finite-Re ranges do not meet through sharp corners.

7.6 Dissipation anomaly from sharper velocity gradients

The dimensionless dissipation coefficient is

$$C_\varepsilon \equiv \frac{\varepsilon L}{U^3}. \tag{182}$$

The cascade picture predicts that C_ε approaches a nonzero value as $\mathrm{Re} \to \infty$ for fully developed three-dimensional turbulence. For incompressible flow in the periodic or zero-flux domains used here, the kinetic-energy identity derived in section 8 and integration by parts imply

$$\varepsilon = \nu \langle \partial_j u_i \, \partial_j u_i \rangle \quad \Longrightarrow \quad \langle |\boldsymbol{\nabla} \boldsymbol{u}|^2 \rangle \sim \frac{\varepsilon}{\nu} \to \infty \qquad (\nu \to 0). \tag{183}$$

The mean dissipation remains finite because vortex stretching and nonlinear scale transfer develop increasingly intense small-scale gradients, as anticipated by Equation 162. This singular high-Reynolds-number behavior is the *dissipation anomaly*. Chapter 5, Section 5.2 of Frisch (1995) states the finite-dissipation law and reviews its experimental and numerical evidence. Chapter 6, Sections 6.1.2, 6.5.4, and 6.5.7 of Pope (2000) develop the associated Kolmogorov scales, dissipation spectrum, and finite-Reynolds-number effects.

Figure 9 collects the main K41 scale trends at the end of the phenomenological argument. Its lower-left panel anticipates the spectral flux $\Pi(k)$, the net nonlinear transfer rate from wavenumbers below k to wavenumbers above k. The Fourier-space derivation in section 11 will show why a stationary inertial range has the plateau $\Pi(k) \simeq \varepsilon$.

8 Kinetic-energy injection, transport, and dissipation

The K41 argument used ε as the mean rate carried through the cascade. The kinetic-energy equations now derive that rate from Navier–Stokes dynamics, determine where energy enters, and separate physical-space transport from viscous conversion into heat. Injection, mean-shear production, physical-space transport, interscale transfer, and dissipation describe different operations; equality of their mean rates in a stationary state does not make the operations interchangeable.

8.1 Instantaneous energy supplied by forcing and removed by viscosity

The instantaneous kinetic energy per unit mass is

$$e_{\mathrm{k}}(\boldsymbol{x}, t) \equiv \frac{1}{2} u_i u_i = \frac{1}{2} |\boldsymbol{u}|^2. \tag{184}$$

Multiplying Equation 141 by u_i and using incompressibility gives

$$u_i \partial_t u_i = \partial_t e_{\mathrm{k}}, \qquad u_i u_j \partial_j u_i = \partial_j (u_j e_{\mathrm{k}}), \qquad -\rho^{-1} u_i \partial_i p = -\rho^{-1} \partial_i (p u_i). \tag{185}$$

For the viscous term, the identity $\nu \nabla^2 u_i = \partial_j (2\nu S_{ij})$ gives

$$2\nu u_i \partial_j S_{ij} = \partial_j (2\nu u_i S_{ij}) - 2\nu S_{ij} S_{ij}, \tag{186}$$

because the symmetric tensor S_{ij} has zero contraction with Ω_{ij}. Combining these terms yields the local kinetic-energy equation

$$\boxed{\partial_t e_{\mathrm{k}} + \partial_j \left[u_j \left(e_{\mathrm{k}} + \frac{p}{\rho} \right) - 2\nu u_i S_{ij} \right] = u_i f_i - \varepsilon(\boldsymbol{x}, t), \qquad \varepsilon(\boldsymbol{x}, t) \equiv 2\nu S_{ij} S_{ij}.} \tag{187}$$

The non-negative field $\varepsilon(\boldsymbol{x}, t)$ is the instantaneous viscous dissipation rate per unit mass. Viscosity converts kinetic energy into internal energy; it does not destroy total energy.

Using the fixed-domain average in Equation 160, a periodic domain, or boundaries whose net energy flux vanishes, turns Equation 187 into

$$\boxed{\frac{\mathrm{d}}{\mathrm{d}t} \langle e_{\mathrm{k}} \rangle_{\mathcal{D}} = \varepsilon_{\mathrm{in}} - \varepsilon, \qquad \varepsilon_{\mathrm{in}} \equiv \langle \boldsymbol{u} \cdot \boldsymbol{f} \rangle_{\mathcal{D}}, \qquad \varepsilon \equiv \langle 2\nu S_{ij} S_{ij} \rangle_{\mathcal{D}}.} \tag{188}$$

Here ε_{in} is the mean power injected per unit mass, and ε without an argument denotes the mean dissipation rate. Statistical stationarity makes the left-hand side vanish, so

$$\boxed{\varepsilon_{\text{in}} = \varepsilon \qquad \text{in a statistically stationary state.}} \tag{189}$$

The equality does not mean that forcing acts at the dissipative scales. Nonlinear transfer carries the injected energy from the forced scales to the scales at which viscosity acts. Together with the inertial-range result in Equation 226, the stationary balance reads $\varepsilon_{\text{in}} = \Pi(k) = \varepsilon$. One common rate links three spatially and physically distinct stages of the cascade.

Chapter 5, Section 5.3 of Pope (2000) derives the instantaneous and averaged kinetic-energy balances, while Chapter 2, Section 2.3 of Frisch (1995) derives the global energy balance and dissipation identity.

8.2 Momentum transport by fluctuations

For the Reynolds decomposition, $\langle\cdot\rangle$ retains the ensemble meaning used for the K41 structure functions, or an equivalent average in a statistically stationary and ergodic flow. Every field separates into a mean and a fluctuation,

$$u_i = \overline{u}_i + u_i', \qquad p = \overline{p} + p', \qquad f_i = \overline{f}_i + f_i', \tag{190}$$

where $\overline{u}_i \equiv \langle u_i \rangle$ and therefore $\langle u_i' \rangle = \langle p' \rangle = \langle f_i' \rangle = 0$. The analysis assumes that averaging commutes with spatial and time derivatives. Incompressibility then gives

$$\partial_i \overline{u}_i = 0, \qquad \partial_i u_i' = 0. \tag{191}$$

The nonlinear momentum flux becomes

$$\langle u_i u_j \rangle = \overline{u}_i\, \overline{u}_j + \underbrace{\langle u_i' u_j' \rangle}_{R_{ij}}, \tag{192}$$

where R_{ij} denotes the Reynolds-stress tensor per unit density. Averaging Equation 141 therefore gives

$$\boxed{\partial_t \overline{u}_i + \overline{u}_j \partial_j \overline{u}_i = -\rho^{-1} \partial_i \overline{p} + \nu \nabla^2 \overline{u}_i - \partial_j R_{ij} + \overline{f}_i.} \tag{193}$$

The term $-\rho R_{ij}$ acts as an additional stress in the mean momentum equation. It arises because fluctuations carry the ith component of momentum through a surface whose normal points in the jth direction. Equation (193) is exact but not closed because an equation for the mean velocity introduces the new unknown R_{ij}. Sections 4.1–4.2 of Pope (2000) derive this mean-flow equation, interpret the Reynolds stress as momentum flux, and introduce its closure problem.

8.3 Production of turbulent energy by mean shear

The turbulent kinetic energy per unit mass is half the trace of the Reynolds stress,

$$K \equiv \frac{1}{2} R_{ii} = \frac{1}{2} \langle u_i' u_i' \rangle . \tag{194}$$

Subtracting Equation 193 from the instantaneous equation gives the fluctuation equation

$$\partial_t u_i' + \overline{u}_j \partial_j u_i' + u_j' \partial_j \overline{u}_i + \left(u_j' \partial_j u_i' - \partial_j R_{ij} \right)$$

$$= -\rho^{-1}\partial_i p' + \nu\nabla^2 u'_i + f'_i. \tag{195}$$

Multiplication by u'_i, averaging, and use of Equation 191 gather all divergences into a transport flux and give

$$\boxed{\partial_t K + \overline{u}_j \partial_j K = \mathcal{P} - \varepsilon_{\mathrm{t}} - \partial_j \mathcal{J}_{K,j} + \left\langle u'_i f'_i \right\rangle,} \tag{196}$$

where

$$\mathcal{P} \equiv -R_{ij}\partial_j \overline{u}_i, \qquad \varepsilon_{\mathrm{t}} \equiv 2\nu \left\langle s'_{ij} s'_{ij} \right\rangle, \tag{197}$$

$$\mathcal{J}_{K,j} \equiv \frac{1}{2}\left\langle u'_i u'_i u'_j \right\rangle + \frac{1}{\rho}\left\langle p' u'_j \right\rangle - 2\nu \left\langle u'_i s'_{ij} \right\rangle, \qquad s'_{ij} \equiv \frac{1}{2}(\partial_j u'_i + \partial_i u'_j). \tag{198}$$

The production $\mathcal{P}$ transfers kinetic energy from the mean flow to the fluctuations. The transport vector $\mathcal{J}_{K,j}$ redistributes turbulent energy in physical space through triple-velocity, pressure, and viscous fluxes. The dissipation ε_{t} converts fluctuating kinetic energy into internal energy.

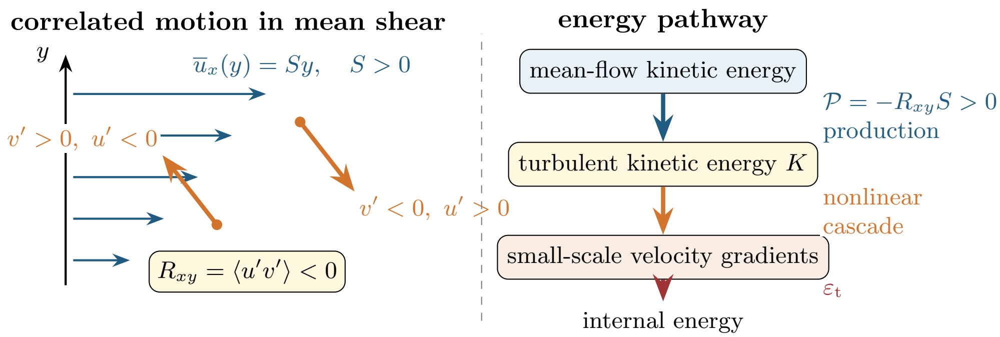

Figure 10. A positive mean shear, $S = \mathrm{d}\overline{u}_x/\mathrm{d}y > 0$, correlates the streamwise and cross-stream fluctuations, denoted by $u' \equiv u'_x$ and $v' \equiv u'_y$, respectively. Upward-moving parcels carry a streamwise velocity deficit, while downward-moving parcels carry an excess, so $R_{xy} = \langle u'v' \rangle < 0$ and $\mathcal{P} = -R_{xy}S > 0$. Production transfers energy from the mean flow into K; the nonlinear cascade then redistributes that turbulent energy across scales before viscosity converts it into internal energy.

In homogeneous turbulence with zero mean velocity, $\mathcal{P} = 0$ and $\partial_j \mathcal{J}_{K,j} = 0$, so forcing and dissipation give

$$\frac{\mathrm{d}K}{\mathrm{d}t} = \left\langle u'_i f'_i \right\rangle - \varepsilon_{\mathrm{t}}. \tag{199}$$

In this limit $u'_i = u_i$, $K = \langle e_{\mathrm{k}} \rangle$, and $\varepsilon_{\mathrm{t}} = \varepsilon$, so Equation 199 recovers the global kinetic-energy balance in Equation 188.

A useful check. Can mean-shear production be identified with the nonlinear cascade? No. Mean shear produces turbulent energy through $-R_{ij}\partial_j \overline{u}_i$, whereas nonlinear interactions redistribute that energy among scales without changing its sum.

Chapter 5, Section 5.3 of Pope (2000) derives the mean-flow and turbulent-kinetic-energy equations and identifies production, transport, and dissipation.

9 Statistical descriptions using increments, correlations, and spectra

K41 needs only a characteristic velocity increment and an energy spectrum. Exact laws need more care. We therefore define averaged random-field statistics, distinguish signed from absolute moments, and state the symmetries used in the real-space calculation. Correlations then connect physical-space separations to Fourier wavenumbers.

9.1 Statistical symmetries of stationarity, homogeneity, and isotropy

Statistical simplification of a two-point equation requires explicit symmetry assumptions. A turbulent field is

- *stationary* if its joint statistics do not change under a shift in time;
- *homogeneous* if its joint statistics do not change under a common translation of all spatial points; and
- *isotropic* if its joint statistics do not change under a common rotation of all positions and vector components.

These properties describe an ensemble, not an individual snapshot. For example, isotropy does not require every vortex to be spherical. Homogeneity makes a two-point statistic depend on the separation $\boldsymbol{r}$ but not on the base point $\boldsymbol{x}$, and isotropy reduces scalar statistics further to dependence on $r = |\boldsymbol{r}|$.

The term *local isotropy* describes sufficiently small scales that lose the directional information imposed by forcing, boundaries, or a mean flow. Local isotropy is an asymptotic hypothesis, not a consequence of incompressibility. It can fail in flows with insufficient scale separation or persistent rotation, stratification, shear, shocks, or magnetic fields.

Chapter 3, Sections 3.7–3.8 of Pope (2000) formalize random fields and averaging. Chapter 4, Sections 4.2–4.4 of Frisch (1995) define stationarity, homogeneity, isotropy, and ergodicity.

9.2 Velocity increments isolate a scale

The characteristic K41 increment now becomes an exact random variable. For two points $\boldsymbol{x}$ and $\boldsymbol{x}' = \boldsymbol{x} + \boldsymbol{r}$, the velocity and forcing increments are

$$\delta \boldsymbol{u}(\boldsymbol{x}, \boldsymbol{r}, t) \equiv \boldsymbol{u}(\boldsymbol{x} + \boldsymbol{r}, t) - \boldsymbol{u}(\boldsymbol{x}, t), \qquad \delta \boldsymbol{f}(\boldsymbol{x}, \boldsymbol{r}, t) \equiv \boldsymbol{f}(\boldsymbol{x} + \boldsymbol{r}, t) - \boldsymbol{f}(\boldsymbol{x}, t). \tag{200}$$

The unit separation vector is $\hat{\boldsymbol{r}} = \boldsymbol{r}/r$. Decomposing the velocity increment into a longitudinal component parallel to $\boldsymbol{r}$ and a transverse vector perpendicular to it gives

$$\delta u_L \equiv \delta \boldsymbol{u} \cdot \hat{\boldsymbol{r}}, \qquad \delta \boldsymbol{u}_T \equiv \delta \boldsymbol{u} - \delta u_L \hat{\boldsymbol{r}}. \tag{201}$$

The longitudinal structure functions are

$$S_{2,L}(r) \equiv \left\langle (\delta u_L)^2 \right\rangle, \qquad S_{3,L}(r) \equiv \left\langle (\delta u_L)^3 \right\rangle, \qquad S_p^{|\cdot|}(r) \equiv \langle |\delta u_L|^p \rangle . \tag{202}$$

Appendix C reviews raw and central moments and applies them to velocity increments. At fixed separation r, homogeneity gives $\mathbb{E}[\delta u_L] = 0$. The function $S_{2,L}$ is therefore the variance of the longitudinal increment, while $S_{3,L}$ is its unnormalized signed third central moment.

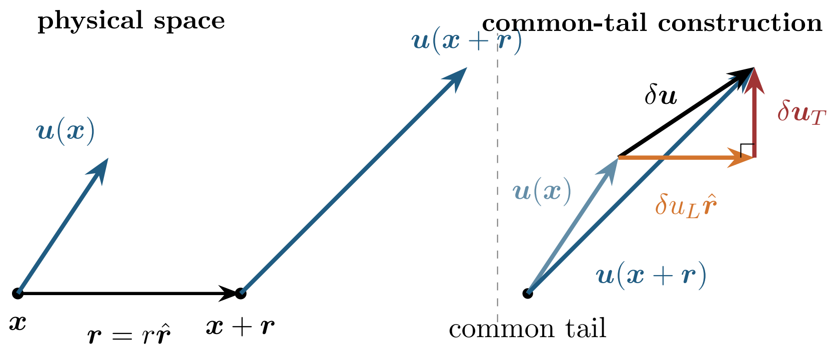

Figure 11. A velocity increment compares the velocity at two points separated by $\boldsymbol{r}$. The right panel translates both velocity vectors to a common tail. The arrow from the tip of $\boldsymbol{u}(\boldsymbol{x})$ to the tip of $\boldsymbol{u}(\boldsymbol{x}+\boldsymbol{r})$ is therefore the exact difference $\delta\boldsymbol{u} = \boldsymbol{u}(\boldsymbol{x}+\boldsymbol{r}) - \boldsymbol{u}(\boldsymbol{x})$. Its longitudinal component $\delta u_L\hat{\boldsymbol{r}}$ lies along the separation, while $\delta\boldsymbol{u}_T$ lies perpendicular to it. These quantities isolate variation on scales of order r without identifying individual eddies.

The signed third-order function $S_{3,L}$ retains the direction of energy transfer; the absolute moment $S_3^{|\cdot|}$ must not replace it. For a sufficiently smooth velocity field, $\delta u_L \sim r$ as $r \to 0$. In an inertial range, rough turbulent fluctuations produce a different power law.

Chapter 6, Section 6.2 of Pope (2000) defines longitudinal and transverse structure functions; Chapter 5, Section 5.1 of Frisch (1995) compares the two-thirds law with measurements.

9.3 Correlations and spectra as complementary scale measures

For homogeneous turbulence with zero mean velocity, the two-point correlation tensor is

$$C_{ij}(\boldsymbol{r}) \equiv \langle u_i(\boldsymbol{x}) u_j(\boldsymbol{x}+\boldsymbol{r})\rangle \,. \tag{203}$$

The identity below connects the increment and correlation.

$$\left\langle |\delta\boldsymbol{u}|^2 \right\rangle = 2\left[C_{ii}(\boldsymbol{0}) - C_{ii}(\boldsymbol{r})\right]. \tag{204}$$

Large correlation means that the velocities remain similar across $\boldsymbol{r}$; a large second-order increment means that they differ strongly.

The three-dimensional energy spectrum $E(k)$ satisfies

$$K \equiv \frac{1}{2}\left\langle |\boldsymbol{u}|^2 \right\rangle = \int_0^\infty E(k)\,\mathrm{d}k, \qquad \varepsilon = 2\nu \int_0^\infty k^2 E(k)\,\mathrm{d}k. \tag{205}$$

Because the mean velocity vanishes here, $u_i' = u_i$, and K is the turbulent kinetic energy defined in Equation 194. Here $k = |\boldsymbol{k}|$ is the wavenumber magnitude, and $E(k)\mathrm{d}k$ is the kinetic energy per unit mass in a spherical Fourier shell between k and $k + \mathrm{d}k$. Thus $E(k)$ has dimensions $[E] = L^3T^{-2}$. The factor k^2 in the dissipation integral weights small spatial scales, which correspond to large wavenumbers.

Appendix D derives the Fourier-transform relation between $E(k)$ and the second-order structure functions. Under homogeneity, isotropy, and incompressibility, it gives the inertial-range correspondence

$$\boxed{E(k) \propto k^{-5/3} \quad \Longleftrightarrow \quad S_2(r),\, S_{2,L}(r) \propto r^{2/3}.} \tag{206}$$

A separation r samples a range of wavenumbers around $k \sim r^{-1}$; it does not select a single Fourier mode.

Chapter 6, Sections 6.3 and 6.5.1 of Pope (2000) develop correlations and the three-dimensional energy spectrum. Chapter 4, Section 4.5 of Frisch (1995) supplies the underlying spectral representation for stationary random functions.

10 Exact third-order flux in the scale-space energy balance

With a precise language for scale in hand, the two-point Navier–Stokes equation can identify the nonlinear flux directly. Its third-order term measures transfer through separation space without assuming a spectral slope.

10.1 Navier–Stokes dynamics as a two-point scale balance

Writing one copy of Equation 141 at $\boldsymbol{x}$ and a second at $\boldsymbol{x}' = \boldsymbol{x} + \boldsymbol{r}$, subtracting them, multiplying the difference by $2\delta u_i$, and averaging gives an increment equation. Homogeneity converts derivatives with respect to the two positions into derivatives with respect to $\boldsymbol{r}$, while incompressibility removes the pressure contribution. Appendix E shows every step. The resulting Kármán–Howarth–Monin equation is

$$\boxed{\partial_t \left\langle |\delta \boldsymbol{u}|^2 \right\rangle + \boldsymbol{\nabla}_{\boldsymbol{r}} \cdot \left\langle \delta \boldsymbol{u} \, |\delta \boldsymbol{u}|^2 \right\rangle = 2\nu \nabla_{\boldsymbol{r}}^2 \left\langle |\delta \boldsymbol{u}|^2 \right\rangle - 4\varepsilon + 2 \left\langle \delta \boldsymbol{u} \cdot \delta \boldsymbol{f} \right\rangle .} \tag{207}$$

Each term has units of kinetic energy per unit mass per unit time. The divergence of the third-order vector

$$\boldsymbol{Y}(\boldsymbol{r}) \equiv \left\langle \delta \boldsymbol{u} \, |\delta \boldsymbol{u}|^2 \right\rangle \tag{208}$$

measures nonlinear transfer through separation space. The term does not create or destroy total kinetic energy; it redistributes energy across r. Viscosity acts through the separation-space Laplacian, -4ε records the mean dissipation at the two points, and the final term records forcing increments. In MHD the corresponding flux acquires a $\pm$ label for the two Elsasser pseudo-energies.

For stationary turbulence, $\partial_t \left\langle |\delta \boldsymbol{u}|^2 \right\rangle = 0$. If forcing varies on the outer scale L, then $|\delta \boldsymbol{f}|/|\boldsymbol{f}| = \mathcal{O}(r/L)$ for $r \ll L$. At inertial-range separations $L \gg r \gg \eta_{\mathrm{K}}$, both the forcing-increment and viscous terms become negligible, and Equation 207 reduces to

$$\boxed{\boldsymbol{\nabla}_{\boldsymbol{r}} \cdot \boldsymbol{Y}(\boldsymbol{r}) = -4\varepsilon.} \tag{209}$$

This is a constant-flux law in physical scale space.

10.2 Four-thirds and four-fifths laws under isotropy

Under isotropy, the only available direction is $\hat{\boldsymbol{r}}$, so $\boldsymbol{Y}(\boldsymbol{r}) = Y_L(r)\hat{\boldsymbol{r}}$, where

$$Y_L(r) = \left\langle \delta u_L |\delta \boldsymbol{u}|^2 \right\rangle . \tag{210}$$

The radial divergence in three dimensions is

$$\boldsymbol{\nabla}_{\boldsymbol{r}} \cdot [Y_L(r)\hat{\boldsymbol{r}}] = \frac{1}{r^2} \frac{\mathrm{d}}{\mathrm{d}r} \left(r^2 Y_L \right) . \tag{211}$$

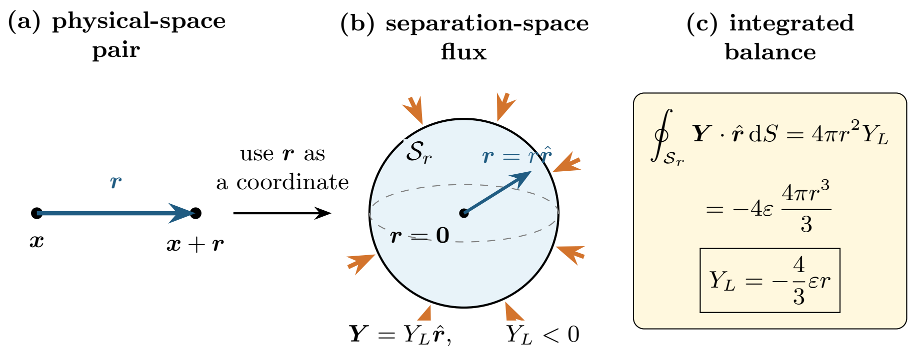

Figure 12. The two-point separation $\boldsymbol{r}$ becomes a coordinate in separation space. For an isotropic downscale cascade, the third-order flux points inward on every point of $\mathcal{S}_r$, so $Y_L<0$. Applying the divergence theorem to $\boldsymbol{\nabla}_{\boldsymbol{r}}\cdot\boldsymbol{Y}=-4\varepsilon$ over $\mathcal{B}_r$ equates the flux through the surface, $4\pi r^2Y_L$, with the constant divergence integrated over the enclosed volume, $-4\varepsilon(4\pi r^3/3)$, and produces the four-thirds coefficient.

Let $\mathcal{B}_r$ denote the ball of radius r in separation space and let $\mathcal{S}_r=\partial\mathcal{B}_r$ denote its spherical boundary.

Substituting Equation 211 into Equation 209, integrating from 0 to r, and requiring a finite flux at the origin gives

$$\frac{\mathrm{d}}{\mathrm{d}r}(r^2Y_L)=-4\varepsilon r^2,\qquad r^2Y_L=-\frac{4}{3}\varepsilon r^3,\qquad \boxed{Y_L(r)=-\frac{4}{3}\varepsilon r.}\tag{212}$$

Equation (212) is the four-thirds law for the mixed third-order structure function.

Isotropy and incompressibility also relate this mixed moment to the longitudinal third-order structure function.

$$Y_L(r)=\frac{1}{3r^3}\frac{\mathrm{d}}{\mathrm{d}r}\left[r^4S_{3,L}(r)\right].\tag{213}$$

Appendix F derives this kinematic identity. Inserting the four-thirds law and integrating once more gives

$$\frac{\mathrm{d}}{\mathrm{d}r}\left(r^4S_{3,L}\right)=-4\varepsilon r^4,\qquad r^4S_{3,L}=-\frac{4}{5}\varepsilon r^5,\qquad \boxed{S_{3,L}(r)=-\frac{4}{5}\varepsilon r.}\tag{214}$$

This is Kolmogorov's four-fifths law. The numerical coefficient is not a fitted constant. It follows from the three-dimensional radial geometry, incompressibility, and the longitudinal projection. The negative sign states that the mean flux is from large scales to small scales.

Before neglecting viscosity, the stationary, homogeneous, isotropic equation gives the exact finite-viscosity relation

$$\boxed{S_{3,L}(r)-6\nu\frac{\mathrm{d}S_{2,L}}{\mathrm{d}r}=-\frac{4}{5}\varepsilon r+\mathcal{I}_f(r),\qquad \mathcal{I}_f(r)\equiv\frac{6}{r^4}\int_0^r s\,\mathrm{d}s\int_0^s\xi^2\left\langle\delta\boldsymbol{u}(\xi)\cdot\delta\boldsymbol{f}(\xi)\right\rangle\mathrm{d}\xi.}\tag{215}$$

The function $\mathcal{I}_f(r)$ carries the accumulated contribution from forcing increments. For smooth forcing concentrated near L, it vanishes faster than r as $r/L\to0$, so

$$S_{3,L}(r)-6\nu\frac{\mathrm{d}S_{2,L}}{\mathrm{d}r}\simeq-\frac{4}{5}\varepsilon r\qquad(r\ll L).\tag{216}$$

At $r \gg \eta_{\mathrm{K}}$, the viscous derivative also becomes subleading and Equation 215 reduces to Equation 214 in the inertial range. At $r \lesssim \eta_{\mathrm{K}}$, the viscous term regularizes the velocity field. Chapter 6, Section 6.3 of Pope (2000) derives the Kármán–Howarth equation and its inertial-range consequence. Chapter 6, Sections 6.2.1–6.2.5 of Frisch (1995) derive the homogeneous and isotropic flux laws, the four-fifths coefficient, and the precise limits of the result.

> **Physical point.** The four-fifths law is exact within its stated assumptions; the familiar $-5/3$ spectrum is a similarity prediction. The exact law constrains the similarity prediction, but the two results do not have the same logical status.

11 Fourier-space redistribution of energy by triads

The real-space laws describe transfer through a separation r. Fourier space describes the same process as conservative redistribution among interacting wavevector triads and makes the spectral flux directly visible.

11.1 Energy conservation under nonlinear triadic transfer

On a periodic domain $\mathcal{D}$ of volume $\mathcal{V}$, the volume-normalized Fourier-series pair is

$$\widehat{u}_i(\boldsymbol{k},t) = \frac{1}{\mathcal{V}}\int_{\mathcal{D}} u_i(\boldsymbol{x},t)e^{-i\boldsymbol{k}\cdot\boldsymbol{x}}\,\mathrm{d}V, \qquad\qquad u_i(\boldsymbol{x},t) = \sum_{\boldsymbol{k}} \widehat{u}_i(\boldsymbol{k},t)e^{i\boldsymbol{k}\cdot\boldsymbol{x}}. \tag{217}$$

Here $\boldsymbol{x}$ denotes position, $\boldsymbol{k}$ is a reciprocal-lattice wavevector, and the i in the exponential is the imaginary unit. Component indices also use i, j, ℓ, with repeated component indices summed. Incompressibility gives $\partial_j u_j = 0$, so the advective nonlinearity has the conservative form $u_j\partial_j u_\ell = \partial_j(u_j u_\ell)$. Applying the Fourier transform in Equation 217 gives

$$\begin{aligned}
(\widehat{u_j\partial_j u_\ell})(\boldsymbol{k},t) &= \frac{1}{\mathcal{V}}\int_{\mathcal{D}} \partial_j(u_j u_\ell)e^{-i\boldsymbol{k}\cdot\boldsymbol{x}}\,\mathrm{d}V \\
&= ik_j(\widehat{u_j u_\ell})(\boldsymbol{k},t) \\
&= ik_j\sum_{\boldsymbol{q}} \widehat{u}_j(\boldsymbol{q},t)\widehat{u}_\ell(\boldsymbol{k}-\boldsymbol{q},t).
\end{aligned} \tag{218}$$

The first line uses the conservative form, the second follows by integration by parts with periodic surface terms cancelling, and the third applies the convolution theorem. In each term of the final sum, $\boldsymbol{q}$ is the wavevector of one input mode and $\boldsymbol{p} \equiv \boldsymbol{k}-\boldsymbol{q}$ is the wavevector of the other. Consequently,

$$\boldsymbol{k} = \boldsymbol{q} + \boldsymbol{p}. \tag{219}$$

The convolution therefore couples every pair $(\boldsymbol{q}, \boldsymbol{p})$ that closes a wavevector triangle with the receiving mode $\boldsymbol{k}$.

The incompressible projection tensor

$$P_{i\ell}(\boldsymbol{k}) \equiv \delta_{i\ell} - \frac{k_i k_\ell}{k^2} \tag{220}$$

satisfies $P_{i\ell}k_\ell = 0$ and removes the Fourier-space pressure gradient, which is parallel to $\boldsymbol{k}$. The momentum equation places the advective term on its right-hand side with a minus sign. Applying $P_{i\ell}$ to Equation 218 therefore gives the projected nonlinear tendency of mode $\boldsymbol{k}$.

$$\widehat{\mathcal{N}}_i(\boldsymbol{k},t) \equiv -iP_{i\ell}(\boldsymbol{k})k_j \sum_{\boldsymbol{q}} \widehat{u}_j(\boldsymbol{q},t)\widehat{u}_\ell(\boldsymbol{k}-\boldsymbol{q},t). \tag{221}$$

Each summand in Equation 221 is one Equation 219 triad, in which modes $\boldsymbol{q}$ and $\boldsymbol{p} = \boldsymbol{k}-\boldsymbol{q}$ generate the nonlinear tendency of $\boldsymbol{k}$. The complete mode equation appears in Appendix G. The modal nonlinear power and its shell-integrated transfer spectrum are

$$\mathcal{T}(\boldsymbol{k},t) \equiv \mathrm{Re}\Big[\widehat{u}_i^*(\boldsymbol{k},t)\widehat{\mathcal{N}}_i(\boldsymbol{k},t)\Big], \qquad \boxed{T(k,t) \equiv \sum_{\boldsymbol{k}} \mathcal{T}(\boldsymbol{k},t)\delta_{\mathrm{D}}(k-|\boldsymbol{k}|)\,.} \tag{222}$$

Here the asterisk denotes complex conjugation, Re selects the real part, and δ_{D} denotes the Dirac delta. Thus $T(k,t)\mathrm{d}k$ is the net rate per unit mass at which nonlinearity gives energy to the Fourier shell $[k, k+\mathrm{d}k]$. Positive T denotes a receiving shell and negative T denotes a donating shell. The appendix derives these expressions from the projected Navier–Stokes equation. Transfer into one mode or shell can have either sign, but the sum over all modes vanishes.

$$\int_0^\infty T(k)\,\mathrm{d}k = 0. \tag{223}$$

Nonlinearity therefore conserves total kinetic energy while redistributing it among wavenumbers.

11.2 The constant-flux plateau in the inertial range

The shell-integrated spectral energy equation is

$$\boxed{\partial_t E(k,t) = T(k,t) + F(k,t) - 2\nu k^2 E(k,t),} \tag{224}$$

where $F(k,t)$ is the power injected per unit wavenumber and $2\nu k^2 E$ is the dissipation spectrum. The flux through wavenumber k is

$$\boxed{\Pi(k,t) \equiv -\int_0^k T(q,t)\,\mathrm{d}q = \int_k^\infty T(q,t)\,\mathrm{d}q.} \tag{225}$$

The equality follows from Equation 223. Positive $\Pi(k)$ means that nonlinearity removes energy from modes below k and gives it to modes above k.

In a stationary state, integrating Equation 224 from 0 to k at wavenumbers above the forcing range but below the dissipation range gives

$$0 \simeq \varepsilon_{\mathrm{in}} + \int_0^k T(q)\,\mathrm{d}q = \varepsilon - \Pi(k), \qquad \boxed{\Pi(k) \simeq \varepsilon.} \tag{226}$$

Thus the real-space law $\boldsymbol{\nabla}_{\boldsymbol{r}} \cdot \boldsymbol{Y} = -4\varepsilon$ and the Fourier-space plateau $\Pi(k) = \varepsilon$ express the same conservative cascade in two different scale coordinates.

Chapter 6, Sections 6.4.2–6.4.3 and 6.6 of Pope (2000) derive modal energy transfer and the spectral cascade. The filtered budget in Chapter 2, Section 2.4 and the Fourier-space Kármán–Howarth analysis in Chapter 6, Sections 6.2.2–6.2.3 of Frisch (1995) provide the corresponding cutoff-flux and triadic descriptions.

12 Intermittency and the breakdown of simple similarity

12.1 Anomalous exponents from fluctuating dissipation

The four-fifths law fixes one signed third-order moment, and the spectral plateau fixes the mean flux, but neither result requires the complete increment probability density to retain one scale-independent shape. The K41 argument makes that additional similarity assumption when it replaces the fluctuating local transfer rate by its mean ε. In a real turbulent flow, intense gradients occupy a small and irregular fraction of space. The coarse-grained dissipation $\varepsilon_r(\boldsymbol{x})$ averages the instantaneous dissipation over a region of size r around $\boldsymbol{x}$. Refined similarity replaces the simple estimate by

$$\delta u_r \sim (\varepsilon_r r)^{1/3}. \tag{227}$$

Because the probability distribution of ε_r changes with r, the structure-function exponents need not equal $p/3$.

$$S_p^{|\cdot|}(r) \propto r^{\zeta_p}, \qquad \zeta_p \neq \frac{p}{3} \quad \text{in general.} \tag{228}$$

The signed third-order law still fixes $\zeta_3 = 1$ under its assumptions, even though higher and lower orders show anomalous scaling. A simple measure of increasingly non-Gaussian increments is the scale-dependent flatness

$$\mathcal{F}(r) \equiv \frac{\langle(\delta u_L)^4\rangle}{\langle(\delta u_L)^2\rangle^2}. \tag{229}$$

A Gaussian increment has $\mathcal{F} = 3$. In intermittent turbulence, $\mathcal{F}(r)$ grows as r decreases because rare, intense increments contribute strongly to the fourth moment. For comparison across scales, the normalized longitudinal increment $\widetilde{u}_r \equiv \delta u_L/\sigma_r$, where $\sigma_r^2 \equiv \langle(\delta u_L)^2\rangle$, has zero mean and unit variance in homogeneous isotropic turbulence. The symbol $p_r(\widetilde{u}_r)$ denotes its scale-dependent probability density.

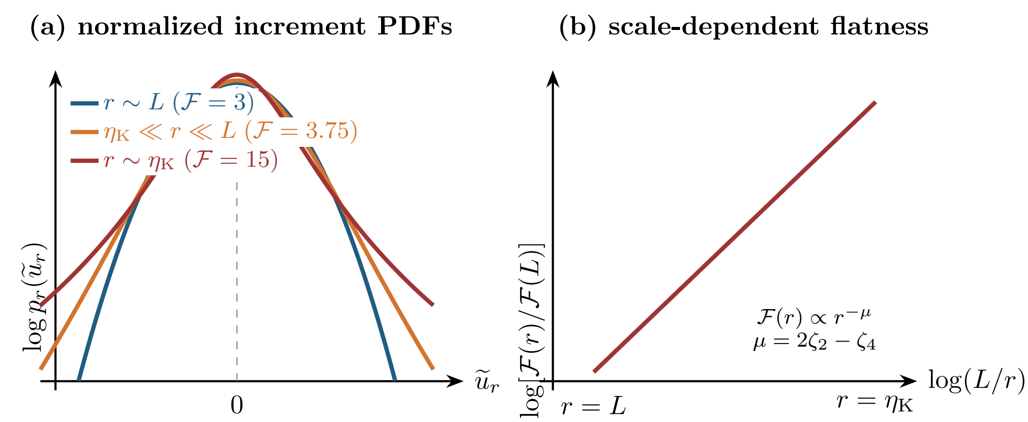

Figure 13. The left panel compares smooth model probability densities of the normalized increment $\widetilde{u}_r$. It shows a unit-variance Gaussian at $r \sim L$ and standardized unit-variance Student-t densities with 12 and 4.5 degrees of freedom at successively smaller r. Their flatness values are 3, 3.75, and 15, respectively. The common plotting scales show the faster Gaussian tail decay as a narrower visible curve and separate the two heavy-tailed cases without introducing shoulders. The right panel plots Equation 230 on logarithmic axes, so an inertial-range power law becomes a straight line of slope μ; forcing- and dissipation-range crossovers need not follow that line.

Combining Equation 229 with Equation 228 gives the inertial-range prediction

$$\boxed{\frac{\mathcal{F}(r)}{\mathcal{F}(L)} \sim \left(\frac{r}{L}\right)^{\zeta_4 - 2\zeta_2} = \left(\frac{L}{r}\right)^{\mu}, \qquad \mu \equiv 2\zeta_2 - \zeta_4 > 0.} \tag{230}$$

The outer-scale value satisfies $\mathcal{F}(L) \simeq 3$ when the large-scale increment is nearly Gaussian.

Chapter 6, Sections 6.7.2–6.7.4 of Pope (2000) compare higher-order statistics and internal intermittency with the Kolmogorov hypotheses and introduce refined similarity. Chapter 8, Sections 8.1–8.4 of Frisch (1995) develop scale-dependent flatness, anomalous structure-function exponents, experimental evidence, and exact constraints on those exponents.

12.2 Exact laws and similarity hypotheses

Statement	Status	Required conditions
Navier–Stokes energy balance	Exact	Constant density and Newtonian viscosity, with the stated boundary flux
Reynolds momentum and energy equations	Exact but unclosed	Averaging commutes with derivatives
Kármán–Howarth–Monin equation	Exact	Homogeneous incompressible turbulence
$S_{3,L} = -(4/5)\varepsilon r$	Exact inertial-range consequence	Homogeneity, isotropy, stationarity, $L \gg r \gg \eta_{\mathrm{K}}$, and large-scale forcing
$S_{2,L} \propto (\varepsilon r)^{2/3}$	Similarity prediction	K41 universality and negligible intermittency corrections
$E(k) = C_K \varepsilon^{2/3} k^{-5/3}$	Similarity prediction	Homogeneous, locally isotropic, constant-flux inertial range
$\eta_{\mathrm{K}} = (\nu^3/\varepsilon)^{1/4}$	Dimensional dissipative scale	Small-scale statistics controlled by ν and ε

12.3 Shocks and magnetic fields beyond incompressible hydrodynamics

Compressibility reintroduces density and thermodynamic fluctuations. The kinetic-energy budget then contains pressure dilatation, $-p\boldsymbol{\nabla}\cdot\boldsymbol{u}$, and shocks can convert kinetic energy directly into heat without following the incompressible cascade picture at every scale. Density weighting and additional flux terms replace the simple incompressible increment law.

Magnetic fields introduce magnetic energy, magnetic tension, and an Alfvén propagation time. Kinetic and magnetic energies exchange reversibly, and the cascade becomes anisotropic with respect to the local magnetic field. Scale-by-scale transfer then depends on both the nonlinear turnover time and the Alfvén time.

Part III

Magnetohydrodynamic turbulence

A magnetic field changes more than the energy budget. Alfvén waves carry information along the field, and nonlinear transfer requires oppositely directed wave packets. The competition between propagation and distortion produces an anisotropic cascade.

Notation for magnetized turbulence

Bold symbols denote vectors. The symbols $\boldsymbol{x}$, $\boldsymbol{r}$, $\boldsymbol{k}$, $\boldsymbol{u}$, and $\boldsymbol{f}$ denote position, separation, wavevector, velocity, and acceleration per unit mass. The calligraphic symbol $\mathcal{V}$ denotes a volume, ν denotes kinematic viscosity, and η denotes magnetic diffusivity. The Kolmogorov length is therefore written η_{K}. Formal ordering parameters use ϵ with a descriptive subscript, whereas ε denotes an energy injection, cascade, or dissipation rate per unit mass. The symbol $\Pi(k)$ denotes spectral flux, while P_{tot} denotes total kinematic pressure.

Uppercase $\boldsymbol{B}$ always denotes a physical magnetic field in SI units. Lowercase $\boldsymbol{b}$ in this part denotes a magnetic fluctuation converted to velocity units; it does not denote the binormal of a field-line basis. Plane waves use the convention $\exp[i(\boldsymbol{k}\cdot\boldsymbol{x}-\omega t)]$.

13 Elsasser variables and mutual advection in MHD

13.1 Incompressible MHD in shared velocity units

The model describes a plasma with constant mass density ρ_0, kinematic viscosity ν, and magnetic diffusivity η. A uniform guide field $\boldsymbol{B}_0 = B_0\hat{\boldsymbol{e}}_\parallel$ selects the parallel direction $\hat{\boldsymbol{e}}_\parallel$. The fluctuating magnetic field $\delta\boldsymbol{B}(\boldsymbol{x},t)$ enters in velocity units through

$$\boldsymbol{b}(\boldsymbol{x},t) \equiv \frac{\delta\boldsymbol{B}(\boldsymbol{x},t)}{\sqrt{\mu_0\rho_0}}, \qquad v_{\mathrm{A}} \equiv \frac{B_0}{\sqrt{\mu_0\rho_0}}, \qquad \partial_\parallel \equiv \hat{\boldsymbol{e}}_\parallel\cdot\boldsymbol{\nabla}, \tag{231}$$

where μ_0 denotes the vacuum permeability and v_{A} denotes the guide-field Alfvén speed. The solenoidal fields $\boldsymbol{u}$ and $\boldsymbol{b}$ obey

$$\partial_t\boldsymbol{u} + \boldsymbol{u}\cdot\boldsymbol{\nabla}\boldsymbol{u} = -\boldsymbol{\nabla}P_{\mathrm{tot}} + v_{\mathrm{A}}\partial_\parallel\boldsymbol{b} + \boldsymbol{b}\cdot\boldsymbol{\nabla}\boldsymbol{b} + \nu\nabla^2\boldsymbol{u} + \boldsymbol{f}_u, \qquad \boldsymbol{\nabla}\cdot\boldsymbol{u} = 0, \tag{232}$$

$$\partial_t\boldsymbol{b} + \boldsymbol{u}\cdot\boldsymbol{\nabla}\boldsymbol{b} = v_{\mathrm{A}}\partial_\parallel\boldsymbol{u} + \boldsymbol{b}\cdot\boldsymbol{\nabla}\boldsymbol{u} + \eta\nabla^2\boldsymbol{b} + \boldsymbol{f}_b, \qquad \boldsymbol{\nabla}\cdot\boldsymbol{b} = 0. \tag{233}$$

The total kinematic pressure

$$P_{\mathrm{tot}} \equiv \frac{p}{\rho_0} + \frac{|\boldsymbol{B}_0+\delta\boldsymbol{B}|^2}{2\mu_0\rho_0} \tag{234}$$

combines the plasma pressure p and magnetic pressure; any spatially uniform part drops out of its gradient. The accelerations $\boldsymbol{f}_u$ and $\boldsymbol{f}_b$ represent mechanical and magnetic forcing. They denote the solenoidal parts of those forcings; the total pressure absorbs any gradient part. Mechanical forcing alone corresponds to $\boldsymbol{f}_b = \boldsymbol{0}$.

13.2 Mutual advection by counterpropagating Elsasser fields

The Elsasser fields and their forcings are

$$\boldsymbol{z}^{+} \equiv \boldsymbol{u} + \boldsymbol{b}, \qquad \boldsymbol{z}^{-} \equiv \boldsymbol{u} - \boldsymbol{b}, \qquad \boldsymbol{f}^{\pm} \equiv \boldsymbol{f}_u \pm \boldsymbol{f}_b. \tag{235}$$

Adding and subtracting Equation 232 and Equation 233 exposes the nonlinear factorization

$$-\boldsymbol{u}\cdot\boldsymbol{\nabla}\boldsymbol{u} \mp \boldsymbol{u}\cdot\boldsymbol{\nabla}\boldsymbol{b} + \boldsymbol{b}\cdot\boldsymbol{\nabla}\boldsymbol{b} \pm \boldsymbol{b}\cdot\boldsymbol{\nabla}\boldsymbol{u} = -\big(\boldsymbol{u} \mp \boldsymbol{b}\big)\cdot\boldsymbol{\nabla}\big(\boldsymbol{u} \pm \boldsymbol{b}\big) = -\boldsymbol{z}^{\mp}\cdot\boldsymbol{\nabla}\boldsymbol{z}^{\pm}. \tag{236}$$

The viscous and resistive terms similarly become

$$\nu\nabla^2\boldsymbol{u} \pm \eta\nabla^2\boldsymbol{b} = \frac{\nu+\eta}{2}\nabla^2\boldsymbol{z}^{\pm} + \frac{\nu-\eta}{2}\nabla^2\boldsymbol{z}^{\mp}. \tag{237}$$

The complete Elsasser equations therefore read

$$\boxed{\begin{gathered}\partial_t\boldsymbol{z}^{\pm} \mp v_{\mathrm{A}}\partial_{\parallel}\boldsymbol{z}^{\pm} + \boldsymbol{z}^{\mp}\cdot\boldsymbol{\nabla}\boldsymbol{z}^{\pm} = -\boldsymbol{\nabla}P_{\mathrm{tot}} + \frac{\nu+\eta}{2}\nabla^2\boldsymbol{z}^{\pm} + \frac{\nu-\eta}{2}\nabla^2\boldsymbol{z}^{\mp} + \boldsymbol{f}^{\pm},\\ \boldsymbol{\nabla}\cdot\boldsymbol{z}^{\pm} = 0.\end{gathered}} \tag{238}$$

Taking the divergence supplies the pressure constraint

$$\boxed{\nabla^2 P_{\mathrm{tot}} = -\partial_i z_j^{\mp}\,\partial_j z_i^{\pm},} \tag{239}$$

where repeated Cartesian indices imply summation. Equality of the two apparent right-hand sides follows after relabeling the dummy indices. Pressure projects the nonlinear interaction onto divergence-free fields.

> **Physical point.** Hydrodynamics contains the self-advection nonlinearity, $\boldsymbol{u}\cdot\boldsymbol{\nabla}\boldsymbol{u}$. Incompressible MHD instead contains a mutual-advection nonlinearity. The field $\boldsymbol{z}^{-}$ distorts $\boldsymbol{z}^{+}$, and $\boldsymbol{z}^{+}$ distorts $\boldsymbol{z}^{-}$.

13.3 Absence of interactions between co-propagating wave packets

Setting $\boldsymbol{z}^{-} = \boldsymbol{0}$ removes the nonlinearity from the $\boldsymbol{z}^{+}$ equation. In the ideal, unforced limit, any solenoidal transverse profile satisfying

$$\boldsymbol{z}^{+} = \boldsymbol{F}\big(\boldsymbol{x}_{\perp}, x_{\parallel} + v_{\mathrm{A}}t\big)\,, \qquad \boldsymbol{\nabla}_{\perp}\cdot\boldsymbol{F} = 0, \tag{240}$$

solves Equation 238; it propagates in the $-\hat{\boldsymbol{e}}_{\parallel}$ direction under the sign convention in Equation 235. Similarly,

$$\boldsymbol{z}^{-} = \boldsymbol{G}\big(\boldsymbol{x}_{\perp}, x_{\parallel} - v_{\mathrm{A}}t\big)\,, \qquad \boldsymbol{\nabla}_{\perp}\cdot\boldsymbol{G} = 0, \tag{241}$$

propagates in the $+\hat{\boldsymbol{e}}_{\parallel}$ direction. These arbitrary-amplitude, arbitrary-shape solutions extend the linear shear-Alfvén waves derived earlier. Nonlinear distortion requires spatial overlap between both propagation families.

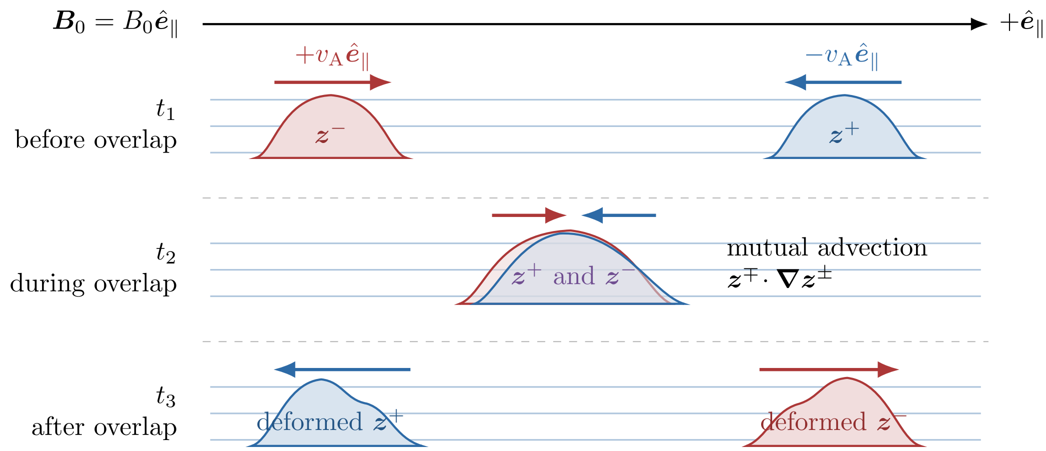

Figure 14. A collision of counterpropagating Alfvén packets at times $t_1 < t_2 < t_3$. The guide field $\boldsymbol{B}_0 = B_0\hat{\boldsymbol{e}}_\parallel$ defines the positive parallel direction. The Elsasser fields $\boldsymbol{z}^\pm = \boldsymbol{u} \pm \boldsymbol{b}$ propagate at velocities $\mp v_A\hat{\boldsymbol{e}}_\parallel$, respectively, where v_A is the guide-field Alfvén speed. Before and after overlap, each packet propagates without self-distortion; during overlap, the term $\boldsymbol{z}^\mp \cdot \boldsymbol{\nabla} \boldsymbol{z}^\pm$ deforms both outgoing packets.

14 Cascade geometry set by a strong guide field

The Elsasser equations identify which fluctuations interact, but not the strength or geometry of that interaction. A strong guide field supplies both ingredients. Alfvénic propagation selects a parallel direction, while nonlinear mixing acts primarily across that direction. Reduced MHD isolates this anisotropic Alfvénic dynamics.

14.1 Parallel propagation and perpendicular shearing

Reduced MHD targets the low-frequency, anisotropic Alfvénic fluctuations supported by a strong guide field. The word "reduced" does not mean that the fields become independent of the parallel coordinate. The packets still vary and propagate along $\boldsymbol{B}_0$, but their dominant velocity and magnetic perturbations point across $\boldsymbol{B}_0$ and vary more rapidly across it.

Let $Z_\perp$ denote a characteristic perpendicular Elsasser amplitude, and let $L_\perp$ and $L_\parallel$ denote the packet widths across and along the guide field. Two independent small ratios describe this regime.

$$\boxed{\epsilon_z \equiv \frac{Z_\perp}{v_A} \ll 1,} \qquad \boxed{\epsilon_k \equiv \frac{L_\perp}{L_\parallel} \sim \frac{k_\parallel}{k_\perp} \ll 1.} \tag{242}$$

The amplitude ratio ϵ_z states that the Alfvénic perturbation is small compared with the guide-field Alfvén speed. For an Alfvénic fluctuation, this also means that the fluctuating magnetic field tilts the total field through only a small angle. The geometric ratio ϵ_k states that a packet is elongated along $\boldsymbol{B}_0$. These two statements do not yet require $\epsilon_z = \epsilon_k$.

Splitting each field and the gradient into perpendicular and parallel parts gives

$$\boldsymbol{z}^\pm = \boldsymbol{z}_\perp^\pm + z_\parallel^\pm \hat{\boldsymbol{e}}_\parallel, \qquad \boldsymbol{\nabla} = \boldsymbol{\nabla}_\perp + \hat{\boldsymbol{e}}_\parallel \partial_\parallel. \tag{243}$$

The perpendicular projection of the nonlinear term is therefore

$$\left(\boldsymbol{z}^\mp \cdot \boldsymbol{\nabla}\right) \boldsymbol{z}_\perp^\pm = \underbrace{\boldsymbol{z}_\perp^\mp \cdot \boldsymbol{\nabla}_\perp \boldsymbol{z}_\perp^\pm}_{\text{perpendicular mutual shearing}} + \underbrace{z_\parallel^\mp \partial_\parallel \boldsymbol{z}_\perp^\pm}_{\text{smaller by } \epsilon_k}. \tag{244}$$

provided the parallel fluctuation is no larger than the perpendicular one. The first term dominates because the packet changes much more rapidly across the guide field than along it. Parallel or pseudo-Alfvén fluctuations may still be present, but the perpendicular fields mix them without requiring them to feed back on the leading perpendicular cascade.

Solenoidality and the anisotropic geometry similarly give

$$\boldsymbol{\nabla}_\perp \cdot \boldsymbol{z}_\perp^\pm = -\partial_\parallel z_\parallel^\pm \simeq 0, \qquad \nabla^2 = \nabla_\perp^2 + \partial_\parallel^2 \simeq \nabla_\perp^2. \tag{245}$$

Thus the leading perpendicular fields are divergence-free within each plane normal to $\boldsymbol{B}_0$, while diffusion is controlled by the shorter perpendicular scale. Applying these approximations to the perpendicular projection of Equation 238 gives

$$\boxed{\begin{gathered}\partial_t \boldsymbol{z}_\perp^\pm \mp v_\mathrm{A}\partial_\parallel \boldsymbol{z}_\perp^\pm + \boldsymbol{z}_\perp^\mp \cdot \boldsymbol{\nabla}_\perp \boldsymbol{z}_\perp^\pm = -\boldsymbol{\nabla}_\perp P_\mathrm{tot} + \nu \nabla_\perp^2 \boldsymbol{z}_\perp^\pm + \boldsymbol{f}_\perp^\pm, \\ \boldsymbol{\nabla}_\perp \cdot \boldsymbol{z}_\perp^\pm = 0.\end{gathered}} \tag{246}$$

The displayed common diffusion coefficient assumes $\nu = \eta$, or $\mathrm{Pm} = 1$. Unequal ν and η restore the two terms in Equation 238. Taking the perpendicular divergence yields

$$\boxed{\nabla_\perp^2 P_\mathrm{tot} = -\partial_i^\perp z_j^\mp \, \partial_j^\perp z_i^\pm.} \tag{247}$$

The four retained terms have distinct roles. The derivative ∂_t records evolution, $\mp v_\mathrm{A}\partial_\parallel$ propagates a packet along the guide field, $\boldsymbol{z}_\perp^\mp \cdot \boldsymbol{\nabla}_\perp$ lets the counterpropagating field shear it across the guide field, and $-\boldsymbol{\nabla}_\perp P_\mathrm{tot}$ projects that shearing back onto a perpendicularly divergence-free field.

For an Alfvén packet, the propagation and nonlinear terms have characteristic magnitudes

$$\left|v_\mathrm{A}\partial_\parallel \boldsymbol{z}_\perp^\pm\right| \sim \frac{v_\mathrm{A} Z}{L_\parallel}, \qquad \left|\boldsymbol{z}_\perp^\mp \cdot \boldsymbol{\nabla}_\perp \boldsymbol{z}_\perp^\pm\right| \sim \frac{Z^2}{L_\perp}. \tag{248}$$

Their ratio is

$$\boxed{\frac{\text{nonlinear distortion}}{\text{Alfvén propagation}} \sim \frac{Z L_\parallel}{v_\mathrm{A} L_\perp} = \frac{\epsilon_z}{\epsilon_k}.} \tag{249}$$

The standard strong-RMHD ordering takes $\epsilon_z \sim \epsilon_k$ and makes this ratio order unity. Weak RMHD instead has $\epsilon_z \ll \epsilon_k$. The same perpendicular nonlinearity is retained, but it produces only a small change during one Alfvén crossing.

> **Physical point.** Reduced MHD keeps the parallel coordinate but reduces the leading dynamics to perpendicular fields. Alfvén packets propagate *along* $\boldsymbol{B}_0$ and mutually shear one another *across* $\boldsymbol{B}_0$.

The derivation in Appendix H carries the strong distinguished ordering through the full equations. Section 3 of Schekochihin (2022) and Sections 2.6 and 5.3 of Biskamp (2003) develop the same Alfvénic framework.

14.2 Nondimensional distinction between weak and strong interactions

The two independent small ratios in Equation 242 specify the RMHD amplitude and geometry. Their ratio specifies the interaction strength. At the outer perpendicular scale $L_\perp$, parallel coherence length

$L_\parallel$, and Elsasser amplitude Z, the corresponding times and ratio are

$$\tau_{\mathrm{A}0} \equiv \frac{L_\parallel}{v_\mathrm{A}}, \qquad \tau_{\mathrm{nl}0} \equiv \frac{L_\perp}{Z}, \qquad \boxed{\chi_0 \equiv \frac{\tau_{\mathrm{A}0}}{\tau_{\mathrm{nl}0}} = \frac{ZL_\parallel}{v_\mathrm{A} L_\perp} = \frac{\epsilon_z}{\epsilon_k}.} \tag{250}$$

The substitutions

$$\boldsymbol{x}_\perp = L_\perp \boldsymbol{x}_\perp^*, \quad x_\parallel = L_\parallel x_\parallel^*, \quad t = \tau_{\mathrm{A}0} t^*, \quad \boldsymbol{z}_\perp^\pm = Z \boldsymbol{z}_\perp^{\pm *}, \quad P_\mathrm{tot} = Z^2 P_\mathrm{tot}^* \tag{251}$$

transform Equation 246 into

$$\begin{gathered}\partial_{t^*} \boldsymbol{z}_\perp^{\pm *} \mp \partial_\parallel^* \boldsymbol{z}_\perp^{\pm *} + \chi_0 \left(\boldsymbol{z}_\perp^{\mp *} \cdot \boldsymbol{\nabla}_\perp^* \boldsymbol{z}_\perp^{\pm *} + \boldsymbol{\nabla}_\perp^* P_\mathrm{tot}^* \right) = \frac{\chi_0}{\mathrm{Re}_\perp} \nabla_\perp^{*2} \boldsymbol{z}_\perp^{\pm *} + \boldsymbol{f}_\perp^{\pm *}, \\ \boldsymbol{\nabla}_\perp^* \cdot \boldsymbol{z}_\perp^{\pm *} = 0.\end{gathered} \tag{252}$$

where $\mathrm{Re}_\perp = ZL_\perp/\nu$ and $\boldsymbol{f}_\perp^{\pm *} = \tau_{\mathrm{A}0} \boldsymbol{f}_\perp^\pm / Z$. Thus $\chi_0 \ll 1$ describes weak interactions during one wave crossing, while $\chi_0 \sim 1$ describes strong interactions. The limit $\chi_0 \gg 1$ cannot maintain parallel coherence over $L_\parallel$ because signals travel only $v_\mathrm{A}\tau_{\mathrm{nl}0}$ before nonlinear distortion resets the structure.

> **A useful check.** Can two systems with the same Elsasser-amplitude ratio Z/v_A have different interaction strengths? Yes. Their geometry supplies the additional factor $\chi_0 = (Z/v_\mathrm{A})(L_\parallel/L_\perp)$.

The interaction parameter separates weak and strong cascades. The symbols $\varepsilon^\pm$ denote the stationary fluxes per unit mass of the two Elsasser pseudo-energies $\mathcal{E}^\pm \equiv \left\langle |\boldsymbol{z}^\pm|^2 \right\rangle /2$, and ε denotes their common flux in balanced turbulence. Section 19 derives these fluxes from global conservation and two-point statistics. The phenomenological arguments first ask which cascade time can carry them.

The total kinetic-plus-magnetic energy per unit mass is $\mathcal{E} \equiv \left\langle |\boldsymbol{u}|^2 + |\boldsymbol{b}|^2 \right\rangle /2$. The one-dimensional spectrum used throughout the phenomenology follows the hydrodynamical-turbulence normalization.

$$\mathcal{E} = \int_0^\infty E(k)\,\mathrm{d}k, \qquad [E] = L^3 T^{-2}. \tag{253}$$

The reduced spectra $E(k_\perp)$ and $E(k_\parallel)$ integrate over their displayed wavenumber after the remaining directions have been summed. Relations such as $\delta z_\lambda^2 \sim kE(k)$ suppress only convention-dependent factors of order unity.

15 Weak collisions in the Iroshnikov–Kraichnan model

Equation 252 shows that a weak interaction produces only a small change during one Alfvén crossing. The Iroshnikov–Kraichnan model asks how many such crossings a packet must experience before nonlinear distortion changes it by order unity? The answer supplies the collision-counting argument used again in weak MHD turbulence. Its isotropic assumption fails once the guide-field direction affects the cascade.

15.1 Small nonlinear change during one collision

At scale λ, balanced turbulence has comparable Elsasser-increment amplitudes, $\delta z_\lambda^+ \sim \delta z_\lambda^- \sim \delta z_\lambda$. The original Iroshnikov–Kraichnan model treats a packet as isotropic, so its parallel and perpendicular sizes are both of order λ. The nonlinear term in the Elsasser equation then has magnitude

$$\left|\delta \boldsymbol{z}_\lambda^\mp \cdot \boldsymbol{\nabla} \delta \boldsymbol{z}_\lambda^\pm\right| \sim \frac{\delta z_\lambda^2}{\lambda} \equiv \frac{\delta z_\lambda}{\tau_{\rm nl}}, \qquad \tau_{\rm nl} \sim \frac{\lambda}{\delta z_\lambda}. \tag{254}$$

Thus $\tau_{\rm nl}$ is the time that uninterrupted nonlinear shearing would need to produce an order-unity change.

Counterpropagating packets pass through one another instead of remaining together for $\tau_{\rm nl}$. They propagate at $+v_{\rm A}$ and $-v_{\rm A}$, so their relative speed is $2v_{\rm A}$. The overlap time is therefore of order $\lambda/(2v_{\rm A})$. Cascade phenomenology drops fixed numerical factors, so the Alfvén crossing time and the change accumulated during it are

$$\tau_{\rm A} \sim \frac{\lambda}{v_{\rm A}}, \qquad \left|\Delta_1 \boldsymbol{z}_\lambda^\pm\right| \sim \tau_{\rm A} \frac{\delta z_\lambda^2}{\lambda}, \qquad \boxed{\chi_\lambda \equiv \frac{\left|\Delta_1 \boldsymbol{z}_\lambda^\pm\right|}{\delta z_\lambda} \sim \frac{\tau_{\rm A}}{\tau_{\rm nl}} \sim \frac{\delta z_\lambda}{v_{\rm A}} \ll 1.} \tag{255}$$

Here $\Delta_1 \boldsymbol{z}_\lambda^\pm$ is the vector change produced by one collision, and χ_λ is its fractional size. Weak interaction means that the packet emerges from one encounter only slightly deformed.

15.2 Random-walk accumulation over many collisions

The model assumes that each new collision partner has an unrelated phase. Consequently, the vector changes $\Delta_j \boldsymbol{z}_\lambda^\pm$ have no systematic sign and are mutually uncorrelated. After N collisions, the cumulative change $\boldsymbol{D}_N \equiv \sum_{j=1}^N \Delta_j \boldsymbol{z}_\lambda^\pm$ satisfies

$$\left\langle |\boldsymbol{D}_N|^2 \right\rangle = \sum_{i=1}^N \sum_{j=1}^N \left\langle \Delta_i \boldsymbol{z}_\lambda^\pm \cdot \Delta_j \boldsymbol{z}_\lambda^\pm \right\rangle \sim N \left(\chi_\lambda \delta z_\lambda\right)^2, \tag{256}$$

$$D_{N,\rm rms} \equiv \left\langle |\boldsymbol{D}_N|^2 \right\rangle^{1/2} \sim \sqrt{N}\, \chi_\lambda \delta z_\lambda. \tag{257}$$

The cross terms with $i \neq j$ vanish because different collisions are uncorrelated. A cascade step is complete when the cumulative change becomes comparable to the packet itself.

$$D_{N,\rm rms} \sim \delta z_\lambda \quad \Longrightarrow \quad N \sim \chi_\lambda^{-2} \sim \left(\frac{\tau_{\rm nl}}{\tau_{\rm A}}\right)^2, \qquad \boxed{\tau_{\rm cas} \sim N \tau_{\rm A} \sim \frac{\tau_{\rm nl}^2}{\tau_{\rm A}}.} \tag{258}$$

Because $\tau_{\rm A} \ll \tau_{\rm nl}$, many encounters are required and $\tau_{\rm cas} \gg \tau_{\rm nl}$.

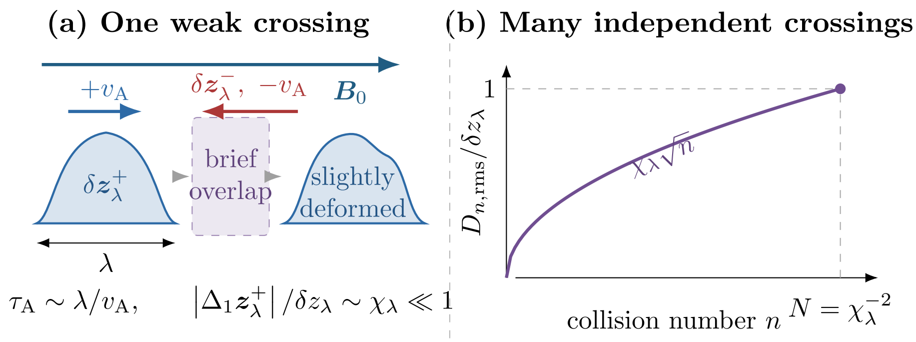

Figure 15. One cascade step in the Iroshnikov–Kraichnan model. (a) A $\delta \boldsymbol{z}_\lambda^+$ packet of size λ propagates along the guide field $\boldsymbol{B}_0$ at v_{A} and briefly overlaps a counterpropagating $\delta \boldsymbol{z}_\lambda^-$ packet. The crossing lasts $\tau_{\mathrm{A}} \sim \lambda/v_{\mathrm{A}}$ and changes the blue packet by only the fraction $\chi_\lambda \ll 1$. (b) The root-mean-square cumulative change $D_{n,\mathrm{rms}}$ grows as $\sqrt{n}\,\chi_\lambda \delta z_\lambda$ when successive changes are independent. It reaches the original amplitude after $N = \chi_\lambda^{-2}$ collisions.

A useful check. If successive distortions had the same sign, they would add as $N\chi_\lambda$ rather than $\sqrt{N}\chi_\lambda$. Order-unity distortion would then take $N \sim \chi_\lambda^{-1}$ and $\tau_{\mathrm{cas}} \sim \tau_{\mathrm{nl}}$. The longer Iroshnikov–Kraichnan cascade time therefore follows specifically from the assumption of independent collision phases.

15.3 The constant-flux isotropic spectrum $k^{-3/2}$

In stationary turbulence, the common pseudo-energy flux ε is the energy δz_λ^2 transferred per cascade time. Substituting both times from Equation 255 into Equation 258 gives

$$\tau_{\mathrm{cas}} \sim \frac{\lambda v_{\mathrm{A}}}{\delta z_\lambda^2}, \qquad \varepsilon \sim \frac{\delta z_\lambda^2}{\tau_{\mathrm{cas}}} \sim \frac{\delta z_\lambda^4}{v_{\mathrm{A}}\lambda}. \tag{259}$$

Solving the right-hand relation for the increment gives

$$\boxed{\delta z_\lambda \sim (\varepsilon v_{\mathrm{A}} \lambda)^{1/4}.} \tag{260}$$

For a scale-local power law, fluctuations at scales no larger than λ satisfy

$$\delta z_\lambda^2 \sim \int_k^\infty E(q)\,\mathrm{d}q \sim kE(k), \qquad k \sim \lambda^{-1}. \tag{261}$$

Combining this relation with Equation 260 produces the isotropic Iroshnikov–Kraichnan spectrum

$$\boxed{E(k) \sim (\varepsilon v_{\mathrm{A}})^{1/2} k^{-3/2}.} \tag{262}$$

Physical point. The $-3/2$ exponent follows from a specific chain of assumptions. One crossing produces a fractional change $\chi_\lambda \ll 1$, independent changes accumulate as $\sqrt{N}$, and a scale-local stationary cascade carries constant ε. Wave propagation alone does not determine the exponent.

The model's central limitation is now visible. It uses the guide field to define v_A and the crossing time, but simultaneously assumes that every packet has one isotropic size λ. A guide field distinguishes parallel from perpendicular directions, so $\ell_\|$ and λ need not scale together. Modern weak MHD turbulence keeps the small change per collision and its random-walk accumulation while treating the two directions separately. Its resonances then show that the leading transfer changes $k_\perp$ while leaving $k_\|$ fixed. Sections 2.1–2.2 of Schekochihin (2022), Section 12.3 of Galtier (2016), and Section 5.3.2 of Biskamp (2003) develop this historical model and explain its anisotropy problem.

16 Cross-field transfer by weak resonant interactions

16.1 Three-wave resonance with a zero-parallel-wavenumber participant

Weak reduced-MHD turbulence satisfies

$$\chi_\lambda \equiv \frac{\tau_A}{\tau_{nl}} = \frac{\ell_\| \, \delta z_\lambda}{v_A \lambda} \ll 1, \qquad \tau_A = \frac{\ell_\|}{v_A}, \qquad \tau_{nl} = \frac{\lambda}{\delta z_\lambda}. \tag{263}$$

Writing the Alfvén-wave frequency as $\omega_s(\boldsymbol{k}) = s k_\| v_A$ for propagation label $s = \pm 1$, a resonant interaction that scatters an s wave from a counterpropagating $-s$ fluctuation obeys

$$\boldsymbol{k} = \boldsymbol{p} + \boldsymbol{q}, \qquad\qquad \omega_s(\boldsymbol{k}) = \omega_{-s}(\boldsymbol{p}) + \omega_s(\boldsymbol{q}). \tag{264}$$

The parallel components of these two conditions give

$$k_\| = p_\| + q_\|, \qquad\qquad s k_\| v_A = -s p_\| v_A + s q_\| v_A, \tag{265}$$

and hence

$$\boxed{p_\| = 0, \qquad k_\| = q_\|.} \tag{266}$$

A strictly resonant three-wave interaction therefore uses a two-dimensional mediator and changes perpendicular wavenumber without changing the wave frequency or parallel wavenumber. The systematic weak-turbulence theory of Galtier et al. (2000) derives the associated kinetic equations; Section 4 of Schekochihin (2022) gives a critical modern discussion.

16.2 The $k_\perp^{-2}$ perpendicular spectrum of weak turbulence

The absence of a parallel cascade keeps $\ell_\|$ and τ_A approximately fixed. The random-walk result Equation 258 remains valid, but $\tau_{nl} = \lambda/\delta z_\lambda$ now uses the perpendicular scale. Thus

$$\tau_{cas} \sim \frac{\lambda^2}{\delta z_\lambda^2 \tau_A}, \qquad\qquad \varepsilon \sim \frac{\delta z_\lambda^2}{\tau_{cas}} \sim \frac{\delta z_\lambda^4 \tau_A}{\lambda^2}. \tag{267}$$

Solving for the increment and one-dimensional perpendicular spectrum gives

$$\boxed{\delta z_\lambda \sim \left(\frac{\varepsilon}{\tau_A}\right)^{1/4} \lambda^{1/2},} \qquad \boxed{E(k_\perp) \sim \left(\frac{\varepsilon}{\tau_A}\right)^{1/2} k_\perp^{-2}.} \tag{268}$$

The interaction strength grows toward smaller perpendicular scales,

$$\chi_\lambda = \frac{\tau_A \delta z_\lambda}{\lambda} \sim \varepsilon^{1/4} \tau_A^{3/4} \lambda^{-1/2}. \tag{269}$$

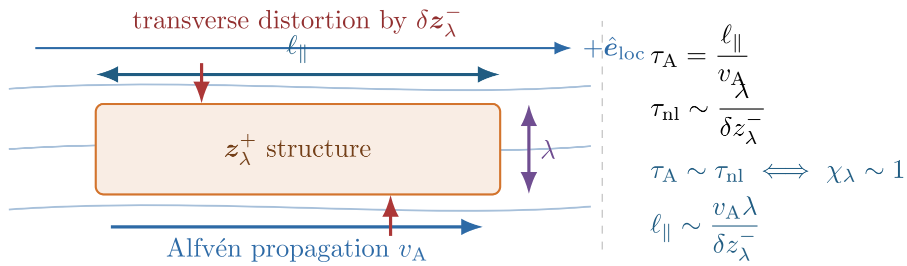

Figure 16. The geometry and competing times of a critically balanced $\boldsymbol{z}_\lambda^+$ structure. The unit vector $\hat{\boldsymbol{e}}_{\mathrm{loc}}$ follows the local magnetic field; $\ell_\parallel$ and λ are the structure's parallel length and perpendicular width. An Alfvén signal crosses the structure at speed v_{A} in time $\tau_{\mathrm{A}} = \ell_\parallel / v_{\mathrm{A}}$, while the counterpropagating increment $\delta \boldsymbol{z}_\lambda^-$ distorts it across λ in $\tau_{\mathrm{nl}} \sim \lambda / \delta z_\lambda^-$. Critical balance sets these times equal, so decreasing λ changes $\ell_\parallel / \lambda$ and produces scale-dependent anisotropy.

Consequently, a weak cascade drives itself toward the critical-balance scale

$$\boxed{\chi_{\lambda_{\mathrm{CB}}} \sim 1 \quad \Longrightarrow \quad \lambda_{\mathrm{CB}} \sim \varepsilon^{1/2} \tau_{\mathrm{A}}^{3/2}.} \tag{270}$$

Weak turbulence can occupy a finite interval, but it does not remain asymptotically weak as λ decreases. The weak cascade therefore generates its own transition to the strong regime. Critical balance determines what replaces random-walk accumulation once $\chi_\lambda \sim 1$.

17 Critical balance between propagation and distortion

17.1 Causal limit on parallel coherence in strong interactions

At perpendicular scale λ, an Alfvénic structure remains coherent along the local magnetic field over a distance $\ell_\parallel$. Propagation communicates information across that distance in $\tau_{\mathrm{A}} = \ell_\parallel / v_{\mathrm{A}}$, while the opposing Elsasser field distorts the structure in $\tau_{\mathrm{nl}} \sim \lambda / \delta z_\lambda$. Critical balance states

$$\boxed{\chi_\lambda \equiv \frac{\tau_{\mathrm{A}}}{\tau_{\mathrm{nl}}} = \frac{\ell_\parallel \delta z_\lambda}{v_{\mathrm{A}} \lambda} \sim 1.} \tag{271}$$

The weak cascade approaches this state from $\chi_\lambda \ll 1$. The opposite inequality $\chi_\lambda \gg 1$ makes a proposed parallel structure too long to communicate before nonlinear disruption. Propagation over one nonlinear time reaches only $\ell_\parallel \sim v_{\mathrm{A}} \tau_{\mathrm{nl}}$, restoring Equation 271. This causal argument makes critical balance an attractor in scale space rather than a numerical coincidence.

17.2 Kolmogorov scaling from a constant perpendicular flux

Strong balanced interactions lose order-unity coherence in one nonlinear time, so

$$\tau_{\mathrm{cas}} \sim \tau_{\mathrm{nl}} \sim \frac{\lambda}{\delta z_\lambda}. \tag{272}$$

The constant-flux condition becomes

$$\varepsilon \sim \frac{\delta z_\lambda^2}{\tau_{\mathrm{cas}}} \sim \frac{\delta z_\lambda^3}{\lambda}. \tag{273}$$

Solving for the increment and spectrum gives the Goldreich–Sridhar perpendicular scaling

$$\boxed{\delta z_\lambda \sim (\varepsilon\lambda)^{1/3},} \qquad \boxed{E(k_\perp) \sim C_{\mathrm{A}}\varepsilon^{2/3}k_\perp^{-5/3},} \tag{274}$$

where the dimensionless constant C_{A} depends on the spectral convention and flow class. The guide-field strength does not enter the perpendicular scaling directly; it sets the parallel coherence associated with each perpendicular scale.

17.3 The $k_\parallel^{-2}$ parallel spectrum under critical balance

Substitution of Equation 274 into critical balance yields

$$\begin{gathered} \frac{\ell_\parallel}{v_{\mathrm{A}}} \sim \frac{\lambda}{(\varepsilon\lambda)^{1/3}}, \\ \boxed{\ell_\parallel \sim v_{\mathrm{A}}\varepsilon^{-1/3}\lambda^{2/3},} \qquad \boxed{k_\parallel \sim \frac{\varepsilon^{1/3}}{v_{\mathrm{A}}}k_\perp^{2/3}.} \end{gathered} \tag{275}$$

Smaller structures become more elongated because $\ell_\parallel/\lambda \propto \lambda^{-1/3}$. Expressing the flux in terms of the parallel propagation time gives

$$\varepsilon \sim \frac{\delta z_{\ell_\parallel}^2}{\ell_\parallel/v_{\mathrm{A}}} \quad \Longrightarrow \quad \delta z_{\ell_\parallel}^2 \sim \frac{\varepsilon\ell_\parallel}{v_{\mathrm{A}}}. \tag{276}$$

Using $\delta z_{\ell_\parallel}^2 \sim k_\parallel E(k_\parallel)$ produces

$$\boxed{E(k_\parallel) \sim \frac{\varepsilon}{v_{\mathrm{A}}}k_\parallel^{-2}.} \tag{277}$$

The strong-turbulence theory of Goldreich and Sridhar (1995) introduced critical balance and the resulting anisotropic cascade. Sections 2.3 and 5 of Schekochihin (2022), Section 12.6 of Galtier (2016), and Section 5.3.3 of Biskamp (2003) provide complementary developments.

18 Geometrical weakening of the strong cascade by alignment

Critical balance relates parallel and perpendicular scales, but the estimate $\tau_{\mathrm{nl}} \sim \lambda/\delta z_\lambda$ also assumes order-unity mutual shearing in the perpendicular plane. Alignment can weaken that shearing and change the strong-cascade spectrum.

18.1 Reduced mutual shearing in aligned sheets

The estimate $\tau_{\mathrm{nl}} \sim \lambda/\delta z_\lambda$ assumes that the advecting Elsasser increment crosses the sharpest gradient. In the perpendicular plane, the identity

$$\boldsymbol{z}_\perp^+ \cdot \boldsymbol{\nabla}_\perp \boldsymbol{z}_\perp^- - \boldsymbol{z}_\perp^- \cdot \boldsymbol{\nabla}_\perp \boldsymbol{z}_\perp^+ = \boldsymbol{\nabla}_\perp \times \left(\boldsymbol{z}_\perp^- \times \boldsymbol{z}_\perp^+\right) \tag{278}$$

shows that near alignment suppresses the difference between the two nonlinear distortions. If θ_λ denotes the angle between $\delta\boldsymbol{z}_\lambda^+$ and $\delta\boldsymbol{z}_\lambda^-$, their cross product has magnitude $\delta z_\lambda^+\delta z_\lambda^- \sin\theta_\lambda$. An unaligned

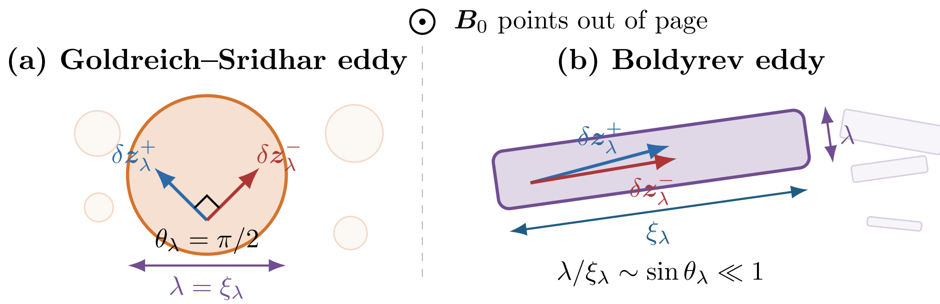

Figure 17. Perpendicular cross-sections of the Goldreich–Sridhar and Boldyrev eddies. The circled dot shows that the guide field $\boldsymbol{B}_0$ points out of the page. Small faded eddies at the sides place each annotated eddy within a multiscale population. The circles in panel (a) show that a Goldreich–Sridhar eddy remains perpendicularly isotropic at every scale. The progressively thinner sheets in panel (b) show the increasing perpendicular anisotropy of smaller Boldyrev eddies, $\xi_\lambda/\lambda \propto \lambda^{-1/4}$. The vectors $\delta\boldsymbol{z}_\lambda^+$ and $\delta\boldsymbol{z}_\lambda^-$ are the two perpendicular Elsasser increments, and θ_λ is their mutual alignment angle. For the foreground Goldreich–Sridhar eddy, $\lambda = \xi_\lambda$ and $\theta_\lambda = \pi/2$. For the foreground Boldyrev eddy, λ is its thickness, while the in-plane length ξ_λ follows the fluctuation direction. The advecting field therefore samples ξ_λ rather than λ, reducing the nonlinear rate by $\sin\theta_\lambda \sim \lambda/\xi_\lambda$.

Goldreich–Sridhar eddy has a single perpendicular scale, $\lambda = \xi_\lambda$, and $\theta_\lambda = \pi/2$. In Boldyrev's theory, an aligned eddy has sheet thickness λ and fluctuation-direction length ξ_λ, with

$$\frac{\lambda}{\xi_\lambda} \sim \sin\theta_\lambda, \qquad \boxed{\tau_{\rm nl}^{\pm} \sim \frac{\lambda}{\delta z_\lambda^{\mp}\sin\theta_\lambda}.} \tag{279}$$

Alignment lengthens the nonlinear time and makes the perpendicular eddy sheet-like. The multi-scale comparison in Figure 17 keeps Goldreich–Sridhar eddies perpendicularly isotropic at every scale, whereas Boldyrev eddies become relatively more elongated toward smaller scales.

18.2 Dynamic alignment as a possible route to a $-3/2$ perpendicular spectrum

For balanced aligned turbulence, the constant-flux estimate becomes

$$\varepsilon \sim \frac{\delta z_\lambda^2}{\tau_{\rm nl}} \sim \frac{\delta z_\lambda^3 \sin\theta_\lambda}{\lambda}. \tag{280}$$

The scale-dependent-alignment conjecture

$$\sin\theta_\lambda \propto \lambda^{1/4} \tag{281}$$

then gives

$$\delta z_\lambda \propto \lambda^{1/4}, \qquad E(k_\perp) \propto k_\perp^{-3/2}, \qquad \ell_\parallel \propto \lambda^{1/2} \quad \text{under critical balance.} \tag{282}$$

Boldyrev (2006) introduced this phenomenology to explain how an anisotropic strong cascade can share the $-3/2$ slope historically associated with IK without restoring isotropy.

The competing predictions produced a long-running $-3/2$ versus $-5/3$ debate. Mason et al. (2006) measured a velocity–magnetic alignment angle close to $\lambda^{1/4}$, while Mason et al. (2008) and Perez et al. (2012) reported perpendicular spectra consistent with $k_\perp^{-3/2}$. In contrast, Beresnyak (2011) argued that alignment saturates and that increasing resolution favors $k_\perp^{-5/3}$; simulations up to 4096^3 subsequently gave the best dissipative-range collapse for a slope near -1.70 (Beresnyak, 2014). The two analyses normalized their dissipation ranges with different candidate cutoff scales, and their raw spectra often differed less than their interpretations; Schekochihin (2022, Sec. 6.3) makes this point explicitly. Short inertial ranges and the non-equivalence of different alignment averages further limited the discrimination. A spectrum alone cannot identify the cascade mechanism because the exact flux vector in Equation 292 can absorb geometrical alignment without selecting either slope. Sections 6.3–6.6 of Schekochihin (2022) review the numerical controversy, the symmetry objection to the original alignment argument, and the modern connection to intermittency and conditioned higher-order statistics.

Figure 18 collects the complete phenomenological path. Resonant weak interactions transfer energy perpendicular to the field at fixed $k_\parallel$ and drive χ_λ toward unity. Beyond critical balance, the Goldreich–Sridhar and aligned strong-cascade models predict different perpendicular slopes.

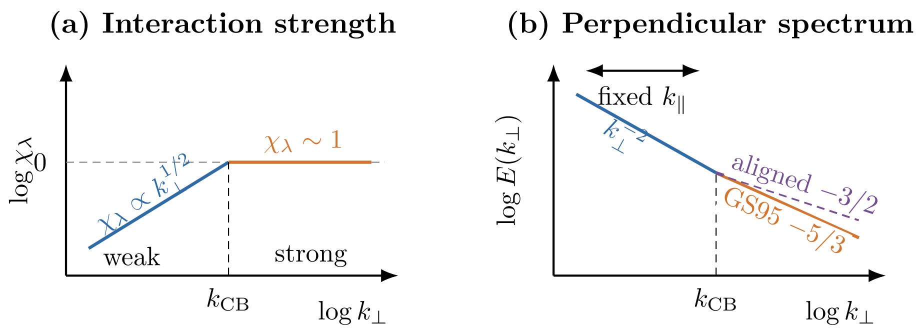

Figure 18. The weak-to-strong transition at the critical-balance wavenumber k_{CB}. Here $k_\perp$ and $k_\parallel$ are wavenumbers perpendicular and parallel to the local magnetic field, $E(k_\perp)$ is the one-dimensional perpendicular spectrum, and $\chi_\lambda = \tau_{\mathrm{A}}/\tau_{\mathrm{nl}}$ measures interaction strength at $\lambda \sim k_\perp^{-1}$. Resonant weak interactions keep $k_\parallel$ fixed, so $\chi_\lambda \propto k_\perp^{1/2}$ and $E(k_\perp) \propto k_\perp^{-2}$ until $\chi_\lambda \sim 1$. The solid orange and dashed purple continuations show the Goldreich–Sridhar $E(k_\perp) \propto k_\perp^{-5/3}$ prediction and the aligned $E(k_\perp) \propto k_\perp^{-3/2}$ alternative, respectively. Both are strong, anisotropic cascades; neither restores the isotropic IK picture.

19 Exact pseudo-energy flux from third-order moments

The cascade models above use a cascade time and a constant mean flux to predict second-order spectra. The MHD equations also give a scale-space flux without assuming a cascade time. Phenomenological spectra depend on a model for the cascade time, whereas exact third-order constraints do not.

19.1 Conservation of Elsasser pseudo-energies by ideal nonlinearity

Angle brackets denote a volume average.

$$\langle q \rangle \equiv \frac{1}{\mathcal{V}} \int_{\mathcal{V}} q(\boldsymbol{x}, t)\, \mathrm{d}V. \tag{283}$$

On a periodic domain, or for fields that decay sufficiently rapidly, surface fluxes vanish. Multiplication of the ideal, unforced $\boldsymbol{z}^{\pm}$ equation by $\boldsymbol{z}^{\pm}$, followed by volume averaging and use of $\boldsymbol{\nabla} \cdot \boldsymbol{z}^{\mp} = 0$, gives

$$\left\langle \boldsymbol{z}^{\pm} \cdot (\boldsymbol{z}^{\mp} \cdot \boldsymbol{\nabla} \boldsymbol{z}^{\pm}) \right\rangle = \frac{1}{2} \left\langle \boldsymbol{\nabla} \cdot (\boldsymbol{z}^{\mp} |\boldsymbol{z}^{\pm}|^2) \right\rangle = 0. \tag{284}$$

The ideal nonlinear interaction therefore conserves each Elsasser pseudo-energy

$$\mathcal{E}^{\pm} \equiv \frac{1}{2} \left\langle |\boldsymbol{z}^{\pm}|^2 \right\rangle. \tag{285}$$

Their half-sum is the physical kinetic-plus-magnetic energy per unit mass,

$$\mathcal{E} \equiv \frac{1}{2} \left\langle |\boldsymbol{u}|^2 + |\boldsymbol{b}|^2 \right\rangle = \frac{\mathcal{E}^+ + \mathcal{E}^-}{2}. \tag{286}$$

For $\nu = \eta$, forcing and diffusion give

$$\frac{\mathrm{d}\mathcal{E}^{\pm}}{\mathrm{d}t} = \underbrace{\left\langle \boldsymbol{z}^{\pm} \cdot \boldsymbol{f}^{\pm} \right\rangle}_{\varepsilon_{\mathrm{in}}^{\pm}} - \underbrace{\nu \left\langle |\boldsymbol{\nabla} \boldsymbol{z}^{\pm}|^2 \right\rangle}_{\varepsilon_{\mathrm{d}}^{\pm}}. \tag{287}$$

The symbols $\varepsilon_{\mathrm{in}}^{\pm}$ and $\varepsilon_{\mathrm{d}}^{\pm}$ denote the injection and dissipation rates of $\mathcal{E}^{\pm}$. Statistical stationarity equates these rates to the inertial-range fluxes $\varepsilon^{\pm}$. The scalar rate used in the balanced phenomenology is

$$\varepsilon \equiv \frac{\varepsilon^+ + \varepsilon^-}{2}, \qquad \varepsilon^+ = \varepsilon^- = \varepsilon \quad \text{for balanced turbulence.} \tag{288}$$

Thus, the following two-point budget describes the scale-by-scale transfer of the quantities that the ideal nonlinear interaction conserves globally.

19.2 Scale-space divergence from two-point increments

Two points $\boldsymbol{x}$ and $\boldsymbol{x}' = \boldsymbol{x} + \boldsymbol{r}$ define the increments

$$\delta \boldsymbol{z}^{\pm}(\boldsymbol{x}, \boldsymbol{r}, t) \equiv \boldsymbol{z}^{\pm}(\boldsymbol{x} + \boldsymbol{r}, t) - \boldsymbol{z}^{\pm}(\boldsymbol{x}, t), \qquad \delta \boldsymbol{f}^{\pm} \equiv \boldsymbol{f}^{\pm}(\boldsymbol{x} + \boldsymbol{r}, t) - \boldsymbol{f}^{\pm}(\boldsymbol{x}, t). \tag{289}$$

The second-order structure functions and third-order flux vectors are

$$S_2^{\pm}(\boldsymbol{r}) \equiv \left\langle |\delta \boldsymbol{z}^{\pm}|^2 \right\rangle, \qquad \boldsymbol{Y}^{\pm}(\boldsymbol{r}) \equiv \left\langle \delta \boldsymbol{z}^{\mp} \, |\delta \boldsymbol{z}^{\pm}|^2 \right\rangle. \tag{290}$$

Appendix C reviews the raw and central moments of a probability density. The vector $\boldsymbol{Y}^{\pm}$ in Equation 290 is a signed mixed third-order moment. Its direction retains information that an absolute moment discards.

Subtracting the Elsasser equation at the two points, dotting the result with $2\delta \boldsymbol{z}^{\pm}$, and imposing statistical homogeneity gives

$$\boxed{\partial_t S_2^{\pm} + \boldsymbol{\nabla}_{\boldsymbol{r}} \cdot \boldsymbol{Y}^{\pm} = 2\nu \nabla_{\boldsymbol{r}}^2 S_2^{\pm} - 4\varepsilon_{\mathrm{d}}^{\pm} + 2 \left\langle \delta \boldsymbol{z}^{\pm} \cdot \delta \boldsymbol{f}^{\pm} \right\rangle.} \tag{291}$$

The calculation in Appendix I derives every term. The guide-field propagation term vanishes under homogeneity because it differentiates the two-point average with respect to the midpoint. The pressure term also becomes a midpoint divergence and vanishes. Nonlinearity survives as a divergence with respect to separation $\boldsymbol{r}$ and therefore transports pseudo-energy through scale.

In a statistically steady state, at separations much smaller than the forcing scale and much larger than the dissipation scale, Equation 291 reduces to

$$\boxed{\boldsymbol{\nabla}_{\boldsymbol{r}} \cdot \boldsymbol{Y}^{\pm} = -4\varepsilon^{\pm},} \tag{292}$$

where the stationary inertial-range flux equals the mean dissipation rate, $\varepsilon^{\pm} = \varepsilon_{\mathrm{d}}^{\pm} = \varepsilon_{\mathrm{in}}^{\pm}$. This exact result requires incompressibility, homogeneity, stationarity, and scale separation; it does not require a phenomenological cascade time.

19.3 Four-thirds coefficient from three-dimensional isotropy

Under full three-dimensional isotropy, the flux vector points along the separation vector, $\boldsymbol{Y}^{\pm} = Y_L^{\pm}(r)\hat{\boldsymbol{r}}$. Its divergence is

$$\boldsymbol{\nabla}_{\boldsymbol{r}} \cdot \boldsymbol{Y}^{\pm} = \frac{1}{r^2}\frac{\mathrm{d}}{\mathrm{d}r}\left(r^2 Y_L^{\pm}\right), \qquad Y_L^{\pm} \equiv \left\langle \delta z_L^{\mp} |\delta \boldsymbol{z}^{\pm}|^2 \right\rangle, \tag{293}$$

where $\delta z_L^{\mp} \equiv \delta \boldsymbol{z}^{\mp} \cdot \hat{\boldsymbol{r}}$ denotes the longitudinal increment. Substitution of Equation 292, multiplication by r^2, and integration from 0 to r give

$$r^2 Y_L^{\pm}(r) - \lim_{s\to 0} s^2 Y_L^{\pm}(s) = -4\varepsilon^{\pm}\int_0^r s^2\,\mathrm{d}s = -\frac{4}{3}\varepsilon^{\pm} r^3. \tag{294}$$

Here s is a dummy radial separation. Regularity at zero separation makes the limit vanish. Dividing by r^2 produces the Politano–Pouquet four-thirds laws

$$\boxed{\left\langle \delta z_L^{\mp} |\delta \boldsymbol{z}^{\pm}|^2 \right\rangle = -\frac{4}{3}\varepsilon^{\pm} r,} \tag{295}$$

which Politano and Pouquet (1998) first derived in this form. The negative sign records a forward mean flux. The law constrains a mixed third-order moment, not the second-order spectrum, so several spectral phenomenologies can satisfy it.

> **Physical point.** The exact law identifies what crosses scale. The $\boldsymbol{z}^{\mp}$ increment transports the squared $\boldsymbol{z}^{\pm}$ increment. The same counterpropagating interaction that appears in the equation also appears in the flux.

The earlier IK, weak-turbulence, and critical-balance arguments yield different cascade times and therefore different second-order spectra. The exact law instead fixes a signed mixed third-order moment. It confirms the mean flux and its direction without selecting a $-5/3$ or $-3/2$ perpendicular spectrum, exactly as the preceding alignment comparison requires. Local-field statistics next make the predicted anisotropic eddy geometry measurable.

20 Local-field statistics for field-following eddies

Critical balance predicts an eddy shape relative to the field along which the Alfvén signal propagates. The choice of reference field is therefore part of the physical measurement, not only a choice of coordinates.

Measurements in a magnetized flow can ask two different questions. A *global* spectrum resolves wavevectors relative to the fixed guide-field direction $\hat{\boldsymbol{e}}_0 \equiv \boldsymbol{B}_0/B_0 = \hat{\boldsymbol{e}}_\parallel$. A *local* statistic instead asks how a fluctuation at separation $\boldsymbol{r}$ is organized relative to the magnetic field that threads that same pair of points. The distinction matters because larger-scale magnetic fluctuations bend the local field and rotate smaller eddies away from $\hat{\boldsymbol{e}}_0$.

This choice prompted an important debate about measured MHD anisotropy. Global Fourier statistics can mix eddies with different local orientations and thereby obscure scale-dependent anisotropy. Cho and Vishniac (2000, Secs. 3.2–4) demonstrated this mixing and recovered increasing small-scale anisotropy with local two-point structure functions; Maron and Goldreich (2001) found the same local-field organization in simulations. Horbury et al. (2008) later used scale-dependent local-field conditioning to measure distinct parallel and perpendicular solar-wind spectra. Global statistics remain valid fixed-frame statistics because they answer a different question. As Oughton and Matthaeus (2020, Sec. 6) emphasize, local conditioning generally defines a higher-order statistic because the direction used for binning depends on the fluctuating field itself. In the strict reduced-MHD limit $\delta b/B_0 \ll 1$, the local and global directions nearly coincide.

The local two-point mean magnetic field at lag $\boldsymbol{r}$ and its unit vector are

$$\boldsymbol{B}_{\rm loc}(\boldsymbol{x};\boldsymbol{r}) \equiv \frac{\boldsymbol{B}(\boldsymbol{x}) + \boldsymbol{B}(\boldsymbol{x}+\boldsymbol{r})}{2}, \qquad \hat{\boldsymbol{e}}_{\rm loc}(\boldsymbol{x};\boldsymbol{r}) \equiv \frac{\boldsymbol{B}_{\rm loc}(\boldsymbol{x};\boldsymbol{r})}{|\boldsymbol{B}_{\rm loc}(\boldsymbol{x};\boldsymbol{r})|}. \tag{296}$$

Here $\boldsymbol{B}(\boldsymbol{x})$ and $\boldsymbol{B}(\boldsymbol{x}+\boldsymbol{r})$ are the physical magnetic fields at the two endpoints. Their arithmetic mean defines the local direction associated with that lag; this definition introduces no separate spatial or spectral filter. The Elsasser increment across the pair and the local components of its separation are

$$\delta\boldsymbol{z}^{\pm}(\boldsymbol{x};\boldsymbol{r}) \equiv \boldsymbol{z}^{\pm}(\boldsymbol{x}+\boldsymbol{r}) - \boldsymbol{z}^{\pm}(\boldsymbol{x}), \qquad r_\parallel \equiv \boldsymbol{r}\cdot\hat{\boldsymbol{e}}_{\rm loc}, \qquad r_\perp \equiv \left|\boldsymbol{r} - r_\parallel \hat{\boldsymbol{e}}_{\rm loc}\right|. \tag{297}$$

Rotating every pair into its own local frame before averaging defines the conditional second-order structure function

$$S^{\pm}_{2,\rm loc}(r_\perp, r_\parallel) \equiv \left\langle |\delta\boldsymbol{z}^{\pm}(\boldsymbol{x};\boldsymbol{r})|^2 \right\rangle_{\substack{\boldsymbol{r}\cdot\hat{\boldsymbol{e}}_{\rm loc}=r_\parallel \\ |\boldsymbol{r}-r_\parallel\hat{\boldsymbol{e}}_{\rm loc}|=r_\perp}}. \tag{298}$$

By contrast, a global structure function $S^{\pm}_{2,\rm g}(r^0_\perp, r^0_\parallel)$ bins the same increments using the fixed components

$$r^0_\parallel \equiv \boldsymbol{r}\cdot\hat{\boldsymbol{e}}_0, \qquad r^0_\perp \equiv \left|\boldsymbol{r} - r^0_\parallel \hat{\boldsymbol{e}}_0\right|. \tag{299}$$

One operational definition of the local eddy aspect ratio follows a constant-structure-function contour.

$$\boxed{S^{\pm}_{2,\rm loc}(\lambda, 0) = S^{\pm}_{2,\rm loc}\big(0, \ell_\parallel(\lambda)\big)\,.} \tag{300}$$

Thus, the parallel distance $\ell_\parallel(\lambda)$ and perpendicular distance λ produce the same mean-square increment when measured in the field-following frame.

Field wandering explains why the two measurements can differ strongly. A larger-scale magnetic perturbation of amplitude δb_L in velocity units tilts the field through $\theta_L \sim \delta b_L/v_{\rm A} = \delta B_L/B_0$. Following the fixed global direction for a distance $\ell_\parallel$ then misses the local field line by

$$\Delta r_\perp \sim \ell_\parallel \theta_L \sim \ell_\parallel \frac{\delta b_L}{v_{\rm A}}. \tag{301}$$

Critical balance gives $\ell_\parallel/v_{\rm A} \sim \lambda/\delta z_\lambda$, and therefore $\Delta r_\perp/\lambda \sim \delta b_L/\delta z_\lambda$. If larger scales dominate the field direction, a nominally parallel global separation crosses many eddy widths and samples perpendicular decorrelation.

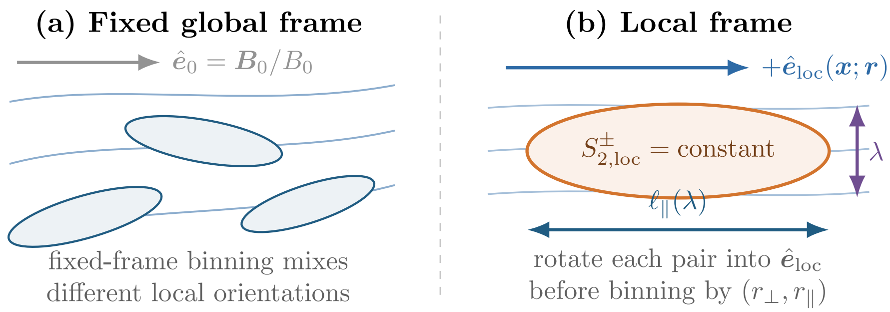

Figure 19. Global and local measurements answer different anisotropy questions. Panel (a) uses the fixed guide-field direction $\hat{\boldsymbol{e}}_0 = \boldsymbol{B}_0/B_0$; averaging eddies that follow differently oriented local fields can blur their scale-dependent aspect ratios in $S^{\pm}_{2,\rm g}(r^0_\perp, r^0_\|)$. Panel (b) uses the local unit vector $\hat{\boldsymbol{e}}_{\rm loc} = \boldsymbol{B}_{\rm loc}/|\boldsymbol{B}_{\rm loc}|$, where $\boldsymbol{B}_{\rm loc} = [\boldsymbol{B}(\boldsymbol{x}) + \boldsymbol{B}(\boldsymbol{x}+\boldsymbol{r})]/2$, and bins each Elsasser increment by its local separation components $r_\perp$ and $r_\|$. A contour of $S^{\pm}_{2,\rm loc}(r_\perp, r_\|)$ then defines the perpendicular width λ and parallel length $\ell_\|(\lambda)$ without mixing local field directions.

Physical point. Global spectra describe anisotropy relative to a fixed mean field. Local conditional structure functions test scale-dependent eddy geometry and critical balance because Alfvén propagation and magnetic tension act along the field threading each eddy.

21 Order-dependent scaling from intermittent current sheets

The exact flux law constrains one signed third-order moment, while the local-field statistics resolve anisotropic second-order geometry. Higher-order moments ask how unevenly the cascade occupies space.

MHD turbulence concentrates magnetic gradients and dissipation into sparse current sheets. For perpendicular increments, structure functions of order p take the form

$$S^{\pm}_p(\lambda) \equiv \left\langle |\delta \boldsymbol{z}^{\pm}_\lambda|^p \right\rangle \propto \lambda^{\zeta^{\pm}_p}. \tag{302}$$

These perpendicular structure functions apply the moment definition introduced in section 19 to an increment probability density at scale λ. A self-similar field would give $\zeta_p = ph$ for one exponent h. Intermittency produces a nonlinear function ζ_p, so increasingly rare structures dominate high-order moments. The scale-dependent flatness

$$\mathcal{F}^{\pm}(\lambda) \equiv \frac{S^{\pm}_4(\lambda)}{[S^{\pm}_2(\lambda)]^2} \propto \lambda^{\zeta^{\pm}_4 - 2\zeta^{\pm}_2} \tag{303}$$

grows toward small scales when $\zeta^{\pm}_4 < 2\zeta^{\pm}_2$. A single energy spectrum probes only second-order statistics and cannot determine the geometry or rarity of the structures that carry dissipation.

22 Limits of balanced Alfvénic turbulence

The cascade theories above assume a homogeneous, incompressible plasma with balanced Elsasser fluxes and an MHD-scale separation from kinetic physics. Relaxing those assumptions does not erase the counterpropagating interaction rule, but it introduces additional times, modes, and transfer channels.

22.1 Dependence of the dominant field on the minority field

The normalized cross-helicity

$$\sigma_{\mathrm{c}} \equiv \frac{2\langle \boldsymbol{u}\cdot\boldsymbol{b}\rangle}{\langle |\boldsymbol{u}|^2+|\boldsymbol{b}|^2\rangle} = \frac{\mathcal{E}^+-\mathcal{E}^-}{\mathcal{E}^++\mathcal{E}^-}, \qquad -1\le\sigma_{\mathrm{c}}\le 1, \tag{304}$$

measures the imbalance between the two propagation families. When $\varepsilon^+\neq\varepsilon^-$, the two Elsasser amplitudes differ and $\sigma_{\mathrm{c}}\neq 0$. Balanced turbulence has $\sigma_{\mathrm{c}}\sim 0$, while a pure one-way Elsasser state reaches $|\sigma_{\mathrm{c}}|=1$ and cannot cascade without the missing counterpropagating field. The simplest strong, local estimate gives

$$\tau_{\mathrm{nl}}^{\pm}\sim\frac{\lambda}{\delta z_\lambda^{\mp}}, \qquad \varepsilon^{\pm}\sim\frac{(\delta z_\lambda^{\pm})^2\delta z_\lambda^{\mp}}{\lambda}. \tag{305}$$

The dominant field cascades slowly because only the minority field can distort it. Correlation times, alignment, and parallel coherence complicate this estimate, so imbalanced strong turbulence admits several competing theories. Chapter 4 of Beresnyak and Lazarian (2019) and Section 9 of Schekochihin (2022) extend the cascade theory to unequal Elsasser fluxes and summarize analytical and numerical results for imbalanced turbulence.

22.2 Additional modes and channels from compressibility and kinetic scales

The derivations above assume constant density, solenoidal fluctuations, a strong local mean field, and scales much larger than plasma kinetic lengths. Relaxing those assumptions adds distinct physics.

Extension	New ingredient	Consequence for the cascade
Imbalanced turbulence	$\mathcal{E}^+\neq\mathcal{E}^-$ and $\varepsilon^+\neq\varepsilon^-$	Unequal nonlinear times because each field requires the other.
Compressible MHD	Density, slow and fast modes, shocks	Mode coupling, compressive fluxes, and shock dissipation supplement the Alfvénic cascade.
Reconnection	Intense, thin current sheets	Topology changes and tearing can modify the smallest inertial-range scales.
Kinetic plasma	Ion and electron gyroscales, pressure anisotropy, phase space	MHD invariants give way to kinetic free-energy channels and species-dependent heating.
No imposed mean field	The local field comes entirely from the fluctuations	Reduced MHD may apply locally, but field generation and saturation belong to dynamo theory.

Chapters 5 and 8 of Beresnyak and Lazarian (2019) treat compressibility and turbulent reconnection. Sections 7 and 14 of Schekochihin (2022) explain the reconnection and kinetic frontiers. Dynamo theory replaces the prescribed guide field with a dynamically generated magnetic field.

Part IV

Fluid dynamos

The preceding part treated a guide field as given. Dynamo theory removes that assumption and asks how motion transfers energy into magnetic fields. Small-scale and large-scale dynamos answer different versions of this question and need not grow at the same rate.

Notation for fluid dynamos

The symbols $\boldsymbol{x}$, $\boldsymbol{r}$, and $\boldsymbol{k}$ denote position, separation, and wavevector. Uppercase $\boldsymbol{B}$ denotes the physical magnetic field in SI units, $\boldsymbol{u}$ denotes the full velocity, ρ_0 denotes the constant mass density, μ_0 denotes the vacuum permeability, ν denotes kinematic viscosity, and η denotes magnetic diffusivity. An overbar denotes an average that obeys the Reynolds rules; $\delta\boldsymbol{u}$ and $\boldsymbol{b}$ denote the velocity and magnetic fluctuations about their means. Here $\boldsymbol{b}$ retains SI magnetic-field units; it is neither a velocity-unit magnetic fluctuation nor the binormal of a field-line basis. The calligraphic symbol $\mathcal{V}$ denotes a volume. The symbols δ_{ij} and ϵ_{ijk} denote the Kronecker delta and Levi–Civita tensor, respectively.

The symbols L and U denote a reference length and velocity. At a turbulent scale ℓ, u_ℓ denotes the characteristic velocity increment and $\tau_\ell \sim \ell/u_\ell$ denotes its turnover time. The symbol ε denotes the kinetic-energy cascade power per unit volume, equal to ρ_0 times the corresponding per-unit-mass rate. The volume-averaged kinetic- and magnetic-energy densities are

$$E_{\mathrm{kin}} \equiv \frac{\rho_0}{2}\left\langle u^2\right\rangle_{\mathcal{V}}, \qquad E_{\mathrm{mag}} \equiv \frac{1}{2\mu_0}\left\langle B^2\right\rangle_{\mathcal{V}}.$$

No decomposition into a fixed guide field plus fluctuations is used because the imposed guide field vanishes throughout.

23 What a fluid dynamo does

23.1 Induction and its dimensionless parameters

For a plasma with constant magnetic diffusivity η, the solenoidal magnetic field satisfies

$$\partial_t \boldsymbol{B} = \boldsymbol{\nabla}\times(\boldsymbol{u}\times\boldsymbol{B}) + \eta\nabla^2\boldsymbol{B}, \qquad \boldsymbol{\nabla}\cdot\boldsymbol{B} = 0. \tag{306}$$

The velocity field also obeys $\boldsymbol{\nabla}\cdot\boldsymbol{u} = 0$ in the incompressible model used below. The following scalings introduce dimensionless primed variables.

$$\boldsymbol{x} = L\boldsymbol{x}', \qquad t = \frac{L}{U}t', \qquad \boldsymbol{u} = U\boldsymbol{u}', \qquad \boldsymbol{B} = B_\star\boldsymbol{B}', \tag{307}$$

where L and U denote the reference length and velocity, and $B_\star$ denotes an arbitrary reference magnetic amplitude. Substitution into Equation 306 gives

$$\frac{UB_\star}{L}\,\partial_{t'}\boldsymbol{B}' = \frac{UB_\star}{L}\,\boldsymbol{\nabla}'\times(\boldsymbol{u}'\times\boldsymbol{B}') + \frac{\eta B_\star}{L^2}\nabla'^2\boldsymbol{B}'. \tag{308}$$

Dividing by the inductive scale $UB_\star/L$ produces

$$\partial_{t'}\boldsymbol{B}' = \boldsymbol{\nabla}' \times (\boldsymbol{u}' \times \boldsymbol{B}') + \frac{1}{\mathrm{Rm}}\nabla'^2\boldsymbol{B}', \qquad \boxed{\mathrm{Rm} \equiv \frac{UL}{\eta}.} \tag{309}$$

Thus Rm compares inductive evolution with Ohmic diffusion. The momentum equation similarly defines $\mathrm{Re} = UL/\nu$, so their ratio gives

$$\boxed{\mathrm{Pm} \equiv \frac{\nu}{\eta} = \frac{\mathrm{Rm}}{\mathrm{Re}}.} \tag{310}$$

The magnetic Prandtl number orders the viscous and resistive cutoffs; it does not by itself measure dynamo supercriticality (Rincon, 2019, Secs. 2.2.1–2.2.2). For a fully ionized, collisional plasma of fixed composition, classical transport gives, up to slowly varying Coulomb logarithms,

$$\nu \propto \frac{T^{5/2}}{n_e}, \qquad \eta \propto T^{-3/2}, \qquad \boxed{\mathrm{Pm} = \frac{\nu}{\eta} \propto \frac{T^4}{n_e},} \tag{311}$$

where T denotes the plasma temperature and n_e denotes the electron number density. The steep temperature dependence and inverse density dependence drive hot, diffuse plasmas toward $\mathrm{Pm} \gg 1$. For example, the representative hot ionized interstellar medium tabulated by Ferrière (2020, Sec. 2 and Table 2) has

$$T \sim 10^6\,\mathrm{K}, \qquad n_e \sim 6 \times 10^{-3}\,\mathrm{cm}^{-3}, \qquad \mathrm{Pm} \sim 5 \times 10^{20}. \tag{312}$$

These estimates use collisional transport coefficients; below particle mean free paths, a kinetic description must replace the fluid dissipation model. The calculations below use the high-Pm ordering.

23.2 Dynamo action transfers kinetic energy to magnetic energy

Magnetohydrodynamic turbulence is often studied relative to a uniform guide field. The dynamo problem instead assumes

$$\boldsymbol{B}_{\text{guide}} = \boldsymbol{0}, \qquad \langle \boldsymbol{B}(\boldsymbol{x},0)\rangle_{\mathcal{V}} = \boldsymbol{0}, \qquad \left\langle B^2(\boldsymbol{x},0)\right\rangle_{\mathcal{V}} > 0, \tag{313}$$

where $\langle\cdot\rangle_{\mathcal{V}}$ denotes a volume average over the periodic domain $\mathcal{V}$. Thus a weak seed field exists, but it has no imposed uniform component. Volume averaging the induction equation shows that the zero-wavenumber field remains zero. The mean field introduced later is a dynamically generated, spatially varying large-scale field, not a guide field.

The conservative nonlinear transfer terms change the local kinetic- and magnetic-energy densities according to

$$\begin{aligned}
\partial_t\left(\frac{\rho_0 u^2}{2}\right)\bigg|_{\text{transfer}} &= \underbrace{-\rho_0 u_i u_j \partial_j u_i}_{U\to U} + \underbrace{\frac{1}{\mu_0} u_i B_j \partial_j B_i}_{B\to U}, \\
\partial_t\left(\frac{B^2}{2\mu_0}\right)\bigg|_{\text{transfer}} &= \underbrace{-\frac{1}{\mu_0} B_i u_j \partial_j B_i}_{B\to B} + \underbrace{\frac{1}{\mu_0} B_i B_j \partial_j u_i}_{U\to B}.
\end{aligned} \tag{314}$$

The capital letters in the transfer labels denote the kinetic-energy reservoir U and the magnetic-energy reservoir B. The $U \to U$ and $B \to B$ terms redistribute energy within a single reservoir. The $B \to U$ and $U \to B$ terms exchange energy between the two reservoirs. Pressure, forcing, viscosity, and resistivity do not appear in Equation 314 because this equation isolates the conservative transfer channels.

In an incompressible periodic domain, the same-reservoir contributions vanish after volume averaging.

$$\langle u_i u_j \partial_j u_i \rangle_{\mathcal{V}} = 0, \qquad \langle B_i u_j \partial_j B_i \rangle_{\mathcal{V}} = 0. \tag{315}$$

They can nevertheless carry nonzero flux across a filter scale or wavenumber. Integration by parts, periodicity, and $\boldsymbol{\nabla} \cdot \boldsymbol{B} = 0$ make the two cross-reservoir contributions equal and opposite.

$$\frac{1}{\mu_0} \langle u_i B_j \partial_j B_i \rangle_{\mathcal{V}} = -\frac{1}{\mu_0} \langle B_i B_j \partial_j u_i \rangle_{\mathcal{V}}. \tag{316}$$

The net $U \to B$ conversion power per unit volume is

$$\boldsymbol{J} \equiv \frac{\boldsymbol{\nabla} \times \boldsymbol{B}}{\mu_0}, \tag{317}$$

$$\boxed{\Pi_{U\to B}} \equiv \frac{1}{\mu_0} \langle B_i B_j \partial_j u_i \rangle_{\mathcal{V}} = -\langle \boldsymbol{u} \cdot (\boldsymbol{J} \times \boldsymbol{B}) \rangle_{\mathcal{V}}. \tag{318}$$

With this sign convention, $\Pi_{U\to B} > 0$ transfers energy from the kinetic reservoir to the magnetic reservoir. The same-reservoir fluxes cannot change the total energy contained in either reservoir.

The volume-averaged magnetic-energy equation retains only the conversion and Ohmic-loss terms.

$$\frac{\mathrm{d}E_{\mathrm{mag}}}{\mathrm{d}t} = \Pi_{U\to B} - \varepsilon_\eta, \qquad \varepsilon_\eta \equiv \frac{\eta}{\mu_0} \left\langle |\boldsymbol{\nabla} \times \boldsymbol{B}|^2 \right\rangle_{\mathcal{V}}. \tag{319}$$

The non-negative quantity ε_η is the Ohmic dissipation rate per unit volume. Appendix N derives Equation 319.

For a prescribed velocity field, Equation 306 is linear in $\boldsymbol{B}$. A kinematic dynamo exists when the magnetic energy has an exponentially growing solution,

$$\left\langle B^2 \right\rangle_{\mathcal{V}}(t) \propto e^{2\gamma t}, \qquad \gamma \equiv \lim_{t\to\infty} \frac{1}{2t} \ln\left[\frac{\left\langle B^2\right\rangle_{\mathcal{V}}(t)}{\left\langle B^2\right\rangle_{\mathcal{V}}(0)}\right] > 0. \tag{320}$$

The growth rate γ measures the net result of conversion and Ohmic loss. Once the Lorentz force changes the prescribed flow, the nonlinear dynamo requires the coupled momentum and induction equations (Rincon, 2019, Sec. 2.3.1).

23.3 Small-scale and large-scale questions

Question	Small-scale or fluctuation dynamo	Large-scale or mean-field dynamo
Quantity that grows	Magnetic fluctuations at or below the velocity-correlation scale	A statistically defined mean field on scales larger than the turbulent motions
Mechanism	Random three-dimensional deformation of magnetic fluctuations	A systematic electromotive force produced by correlations of fluctuations
Helicity requirement	Needs no net kinetic helicity	The simplest isotropic α effect requires broken mirror symmetry
First theoretical object	Two-point magnetic correlator or magnetic spectrum	Mean field $\overline{\boldsymbol{B}}$ and turbulent EMF $\boldsymbol{\mathcal{E}} = \overline{\delta \boldsymbol{u} \times \boldsymbol{b}}$

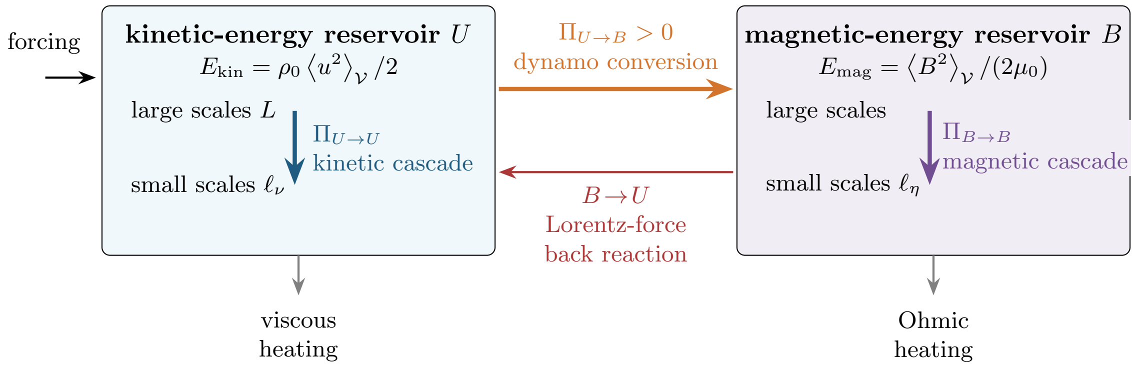

Figure 20. Energy pathways in a forced dynamo. The blue $U \to U$ and purple $B \to B$ arrows denote transfers toward smaller scales within the kinetic and magnetic reservoirs. The orange and red arrows denote exchange between the reservoirs. Viscosity and resistivity convert energy into heat at the cutoff scales ℓ_ν and ℓ_η. Here $E_{\rm kin}$ and $E_{\rm mag}$ are volume-averaged energy densities, L is the outer scale, and $\langle \cdot \rangle_{\mathcal{V}}$ denotes a volume average.

The distinction is useful, but a turbulent plasma can excite both processes at once. The faster small-scale mode can then complicate the interpretation and saturation of the large-scale mode (Rincon, 2019, Sec. 4.5.1).

24 Kinematic small-scale dynamo through stretching, folding, and diffusion

24.1 Magnetic field lines follow material line elements

For incompressible ideal MHD, Equation 41 reduces to

$$\frac{\mathrm{D}B_i}{\mathrm{D}t} = B_j \partial_j u_i. \tag{321}$$

Thus the magnetic field obeys the same local stretching law as a material line element. Appendix L gives the finite-deformation result.

The unit vector along the field is

$$\widehat{\boldsymbol{b}} \equiv \frac{\boldsymbol{B}}{B}. \tag{322}$$

Dotting Equation 321 with $\widehat{\boldsymbol{b}}$ gives

$$\frac{\mathrm{D}\ln B}{\mathrm{D}t} = \widehat{b}_i \widehat{b}_j \partial_j u_i \equiv \sigma_B. \tag{323}$$

The scalar σ_B is the strain along the instantaneous field direction. Along one trajectory,

$$B(t) = B(0) \exp\left[\int_0^t \sigma_B(t')\,\mathrm{d}t'\right]. \tag{324}$$

A positive time-averaged σ_B produces exponential kinematic growth. A turbulent flow must also reorient and fold the growing field so that repeated stretching fits inside a finite domain.

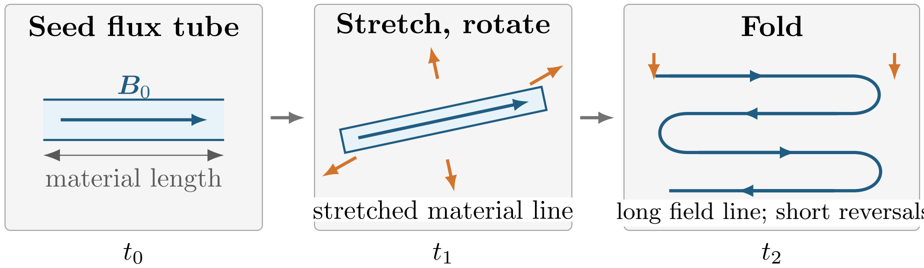

Figure 21. Stretching, reorientation, and folding amplify a frozen-in seed field. The initial field $\boldsymbol{B}_0$ occupies a material flux tube at time t_0. The velocity gradient stretches and rotates the same tube at t_1, and incompressibility narrows it as it lengthens. Subsequent folding at t_2 returns the amplified field to the domain while placing oppositely directed segments next to one another.

The stretching rate fluctuates from one trajectory to another. Its finite-time average is

$$\Lambda_t \equiv \frac{1}{t}\int_0^t \sigma_B(t')\,\mathrm{d}t', \qquad B(t) = B(0)e^{\Lambda_t t}. \tag{325}$$

For a positive moment order q,

$$\langle B^q(t)\rangle = \left\langle B^q(0)e^{q\Lambda_t t}\right\rangle. \tag{326}$$

Large values of q give greater weight to the comparatively rare trajectories that experience unusually strong stretching. The magnetic field therefore becomes intermittent during kinematic growth, and a quoted growth rate must identify the moment being measured—for example, magnetic energy follows the second moment $\left\langle B^2\right\rangle$ (Chertkov et al., 1999).

As a field line lengthens, incompressibility contracts the plasma across it. The transverse magnetic scale therefore decreases, and the Ohmic decay rate η/ℓ^2 increases. Dynamo action requires stretching to outrun that diffusion. Figure 21 summarizes the three-dimensional cycle. Purely axisymmetric magnetic fields and purely two-dimensional flows cannot maintain a dynamo indefinitely; Cowling (1933) and Zel'dovich (1957) make these restrictions precise. Three-dimensionality does not guarantee growth, but it allows the required stretch–fold cycle (Rincon, 2019, Sec. 2.3.2). Appendix M illustrates this distinction with the simplest smooth linear strain.

24.2 Fastest stretching by viscous eddies at high magnetic Prandtl number

For a Kolmogorov inertial range,

$$u_\ell \sim U\left(\frac{\ell}{L}\right)^{1/3}, \qquad \tau_\ell^{-1} \sim \frac{u_\ell}{\ell} \sim \frac{U}{L}\left(\frac{\ell}{L}\right)^{-2/3}. \tag{327}$$

The smallest inertial-range eddies therefore have the largest strain. Balancing their turnover time against viscous diffusion gives

$$\ell_\nu \sim L\mathrm{Re}^{-3/4}, \qquad u_\nu \sim U\mathrm{Re}^{-1/4}, \qquad \gamma_\nu \sim \frac{u_\nu}{\ell_\nu} \sim \frac{U}{L}\mathrm{Re}^{1/2}. \tag{328}$$

When $\mathrm{Pm} \gg 1$, the viscous-scale flow looks smooth at the smaller magnetic-reversal scale. Balancing γ_ν against η/ℓ_η^2 gives

$$\ell_\eta \sim \left(\frac{\eta}{\gamma_\nu}\right)^{1/2} \sim \ell_\nu\mathrm{Pm}^{-1/2}, \qquad k_\eta \sim k_\nu\mathrm{Pm}^{1/2}. \tag{329}$$

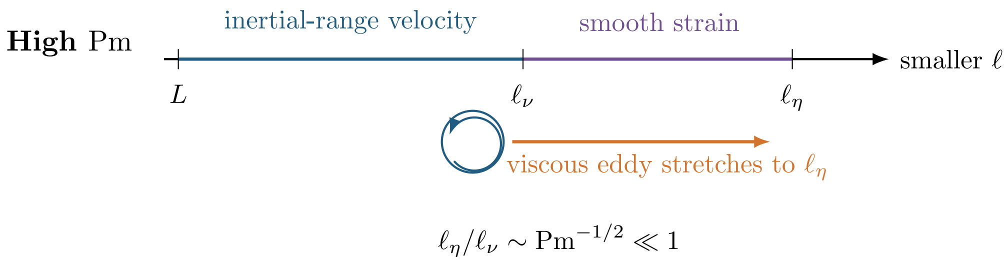

Figure 22. The magnetic Prandtl number $\mathrm{Pm} = \nu/\eta$ orders the viscous scale ℓ_ν and resistive scale ℓ_η below the outer scale L. For $\mathrm{Pm} \gg 1$, the velocity becomes smooth at ℓ_ν and the viscous-scale strain stretches magnetic structure down to $\ell_\eta \ll \ell_\nu$. The blue segment denotes the inertial-range velocity, the purple segment denotes the smooth subviscous strain, and the orange arrow shows a viscous eddy producing magnetic reversals at ℓ_η. The horizontal coordinate represents physical scale ℓ decreasing to the right.

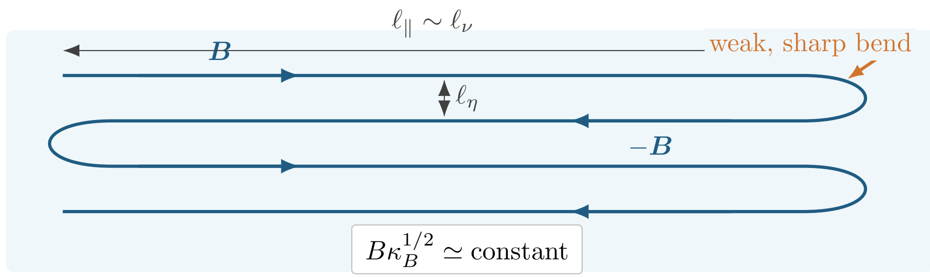

Figure 23. During kinematic large-Pm growth, a folded field remains coherent over the parallel scale $\ell_\parallel \sim \ell_\nu$ but reverses direction across the short resistive scale ℓ_η. Adjacent straight segments therefore carry $\boldsymbol{B}$ and $-\boldsymbol{B}$ with modest curvature, while the bends concentrate curvature and remain comparatively weak. Here $\kappa_B = |(\hat{\boldsymbol{b}} \cdot \boldsymbol{\nabla})\hat{\boldsymbol{b}}|$ is the magnitude of the field-line curvature and $\hat{\boldsymbol{b}} = \boldsymbol{B}/B$.

Here $k_\nu \equiv \ell_\nu^{-1}$ and $k_\eta \equiv \ell_\eta^{-1}$ denote the viscous and resistive wavenumbers. The kinematic growth rate remains of order γ_ν, while magnetic reversals accumulate near ℓ_η (Rincon, 2019, Secs. 3.2–3.3).

24.3 Folded fields with long coherence and short reversals

Large-Pm stretching produces fields that remain coherent along relatively straight segments but reverse across the resistive scale. This folded geometry reconciles a large magnetic gradient with modest curvature (Schekochihin et al., 2004b).

The notation κ_B, rather than κ, distinguishes field-line curvature from the velocity-covariance functions in the Kazantsev model below. The curvature magnitude and normal are

$$\kappa_B \equiv \left|(\widehat{\boldsymbol{b}} \cdot \boldsymbol{\nabla})\widehat{\boldsymbol{b}}\right|, \qquad \widehat{\boldsymbol{n}}_B \equiv \frac{(\widehat{\boldsymbol{b}} \cdot \boldsymbol{\nabla})\widehat{\boldsymbol{b}}}{\kappa_B}. \tag{330}$$

Neglecting Ohmic diffusion and the bending terms involving second spatial derivatives of $\boldsymbol{u}$, the coupled field-strength and curvature equations give

$$\frac{\mathrm{D}}{\mathrm{D}t} \ln\left(B\kappa_B^{1/2}\right) = \frac{1}{2}\hat{n}_{B,i}\hat{n}_{B,j}\partial_j u_i.$$

For isotropic random stretching, the time integral of the right-hand side fluctuates without the secular growth that amplifies B. The resulting statistical prediction is

$$B\kappa_B^{1/2} \simeq \text{constant}, \qquad \Longrightarrow \qquad B \propto \kappa_B^{-1/2}. \tag{331}$$

The prediction explains why strong fields occupy straight portions of a fold and sharp bends contain weaker fields. Simulations find

$$B\kappa_B^{\alpha} \simeq \text{constant}, \qquad\qquad \alpha \simeq 0.47 \tag{332}$$

(Schekochihin et al., 2004b, Sec. 3.2.3).

Magnetic-energy growth and magnetic tension depend on different derivatives.

$$\text{stretching power} \propto B_i B_j \partial_j u_i, \qquad\qquad \text{magnetic tension} \propto (\boldsymbol{B}\cdot\boldsymbol{\nabla})\boldsymbol{B}. \tag{333}$$

The field can therefore store substantial energy in rapid transverse reversals without producing equally large tension everywhere. During the kinematic stage, viscous-scale eddies provide the fastest surviving strain, so the fold geometry has

$$\ell_{\|} \sim \ell_\nu, \qquad\qquad \ell_\eta \sim \ell_\nu \mathrm{Pm}^{-1/2}. \tag{334}$$

Figure 23 separates this strong transverse gradient from the curvature that enters the tension force.

> **A useful check.** At large Pm, viscous eddies set the stretching rate and resistivity sets the reversal scale. How can a velocity field that is smooth below ℓ_ν continue to produce magnetic gradients down to $\ell_\eta \ll \ell_\nu$?

25 Kinematic magnetic spectrum and the Kazantsev result

25.1 The exact spectrum equation is not closed

The induction equation shows how a magnetic field grows at one point. To ask which scales grow, introduce the Fourier transform

$$\widehat{B}_i(\boldsymbol{k},t) \equiv \int_{\mathcal{V}} B_i(\boldsymbol{x},t)e^{-i\boldsymbol{k}\cdot\boldsymbol{x}}\,\mathrm{d}^3x. \tag{335}$$

The component form of the incompressible induction equation is

$$\partial_t B_i = \partial_j(u_i B_j - u_j B_i) + \eta\nabla^2 B_i. \tag{336}$$

Fourier transforming Equation 336 gives

$$\partial_t \widehat{B}_i(\boldsymbol{k}) = \underbrace{ik_j \int \frac{\mathrm{d}^3p}{(2\pi)^3}\left[\widehat{u}_i(\boldsymbol{p})\widehat{B}_j(\boldsymbol{k}-\boldsymbol{p}) - \widehat{u}_j(\boldsymbol{p})\widehat{B}_i(\boldsymbol{k}-\boldsymbol{p})\right]}_{\widehat{\mathcal{I}}_i(\boldsymbol{k})} - \eta k^2 \widehat{B}_i(\boldsymbol{k}). \tag{337}$$

The integration wavevector $\boldsymbol{p}$ labels a velocity mode, while $\boldsymbol{k}-\boldsymbol{p}$ labels the magnetic mode coupled to it. Their sum is the output wavevector $\boldsymbol{k}$. The symbol $\widehat{\mathcal{I}}_i$ denotes the ideal induction term in Fourier space.

For a statistically isotropic field, the one-dimensional magnetic-energy spectrum is

$$M(k,t) \equiv \frac{1}{2\mu_0 \mathcal{V}(2\pi)^3} \int k^2 \, \mathrm{d}\Omega_{\boldsymbol{k}} \, \left\langle \widehat{B}_i^*(\boldsymbol{k},t)\widehat{B}_i(\boldsymbol{k},t) \right\rangle, \tag{338}$$

Here $\mathrm{d}\Omega_{\boldsymbol{k}}$ denotes solid angle in wavevector space, and the star denotes complex conjugation. The integral of the spectrum gives the magnetic-energy density.

$$E_{\mathrm{mag}}(t) = \int_0^\infty M(k,t)\,\mathrm{d}k. \tag{339}$$

Multiplying Equation 337 by $\widehat{B}_i^*$, taking the real part and ensemble average, and integrating over the shell $|\boldsymbol{k}| = k$ gives

$$\partial_t M(k,t) = T_B(k,t) - 2\eta k^2 M(k,t), \tag{340}$$

$$T_B(k,t) \equiv \frac{1}{\mu_0 \mathcal{V}(2\pi)^3} \int k^2 \, \mathrm{d}\Omega_{\boldsymbol{k}} \, \Re \left\langle \widehat{B}_i^*(\boldsymbol{k},t)\widehat{\mathcal{I}}_i(\boldsymbol{k},t) \right\rangle. \tag{341}$$

The transfer T_B contains the third-order correlation $\langle uBB \rangle$. Equation (340) is exact, but it cannot predict M until a model expresses T_B in terms of M. This is the closure problem.

25.2 A random smooth flow closes the spectrum equation

The Kazantsev–Kraichnan model prescribes a velocity field that is Gaussian, homogeneous, isotropic, incompressible, non-helical, and delta-correlated in time. These assumptions are chosen because they close the third-order transfer in Equation 341; they are not a claim that a real turbulent velocity has zero memory. Gaussian integration by parts expresses $\langle uBB \rangle$ in terms of the velocity covariance and the two-point magnetic correlation $\langle BB \rangle$. Appendix O gives that calculation.

For $\mathrm{Pm} \gg 1$, the magnetic reversals lie below the viscous scale, where the velocity is smooth. Expanding its longitudinal and transverse covariances at small separation gives

$$\kappa_L(r) = \kappa_0 - \frac{\kappa_2}{4} r^2 + \mathcal{O}\big(r^4\big), \qquad \kappa_N(r) = \kappa_0 - \frac{\kappa_2}{2} r^2 + \mathcal{O}\big(r^4\big). \tag{342}$$

The constant κ_0 sets the zero-separation covariance, while $\kappa_2 > 0$ measures its curvature. The characteristic viscous-strain rate is

$$\gamma_\nu \equiv \frac{5}{4}\kappa_2 = \frac{5}{2}\left| \frac{\partial^2 \kappa_L}{\partial r^2}(0) \right| \sim \frac{u_\nu}{\ell_\nu}. \tag{343}$$

Fourier transforming the closed two-point equation with this smooth-flow form yields

$$\partial_t M = \frac{\gamma_\nu}{5} \frac{\partial}{\partial k}\left(k^2 \frac{\partial M}{\partial k} - 4kM \right) + 2\gamma_\nu M - 2\eta k^2 M \tag{344}$$

$$= \frac{\gamma_\nu}{5}\left(k^2 \frac{\partial^2 M}{\partial k^2} - 2k\frac{\partial M}{\partial k} + 6M \right) - 2\eta k^2 M. \tag{345}$$

The first line separates spectral transport, stretching production, and Ohmic loss. The second line is the same equation expanded. It describes diffusion and drift in $\ln k$ together with net growth. Kulsrud and Anderson (1992, Sec. 3 and App. C) recover this same large-k operator by expanding a spectral mode-coupling equation for magnetic modes with $k > k_\nu$. Their calculation shows directly how velocity modes near the viscous cutoff redistribute and stretch magnetic energy. If the spectral flux vanishes at the integration boundaries, integrating the first line gives

$$\frac{\mathrm{d}}{\mathrm{d}t}\int_0^\infty M\,\mathrm{d}k = 2\gamma_\nu \int_0^\infty M\,\mathrm{d}k - 2\eta \int_0^\infty k^2 M\,\mathrm{d}k. \tag{346}$$

Random strain therefore amplifies the total magnetic energy while transporting it toward the resistive range. The original calculation appears in Kazantsev (1968); Rincon (2019, Sec. 3.4.8) and Schekochihin et al. (2002a) give detailed modern spectral treatments.

25.3 Why the diffusion-free spectrum contains $k^{3/2}$

The smooth, diffusion-free calculation uses

$$k_\nu \ll k \ll k_\eta, \qquad \eta = 0, \qquad x \equiv \ln(k/k_0). \tag{347}$$

Here k_0 denotes the initial seed wavenumber, taken near the forcing scale. The logarithmic derivatives are

$$k\partial_k = \partial_x, \qquad k^2\partial_k^2 = \partial_x^2 - \partial_x, \tag{348}$$

Equation 345 becomes

$$\partial_t M = \frac{\gamma_\nu}{5}\left(\partial_x^2 M - 3\partial_x M + 6M\right). \tag{349}$$

The substitution

$$M(x,t) = e^{3x/2+3\gamma_\nu t/4}\,\Psi(x,t) \tag{350}$$

cancels the first derivative and leaves an ordinary diffusion equation,

$$\partial_t \Psi = \frac{\gamma_\nu}{5}\,\partial_x^2 \Psi. \tag{351}$$

For an initially narrow spectrum, the initial condition and its total energy are

$$M(k,0) = E_{\mathrm{mag},0}\delta(k-k_0), \qquad E_{\mathrm{mag},0} \equiv \int_0^\infty M(k,0)\,\mathrm{d}k. \tag{352}$$

The Green's function of Equation 351 then gives

$$M(k,t) = \frac{E_{\mathrm{mag},0}}{k_0}\left(\frac{5}{4\pi\gamma_\nu t}\right)^{1/2}\left(\frac{k}{k_0}\right)^{3/2}\exp\left(\frac{3\gamma_\nu t}{4}\right)\exp\left[-\frac{5\ln^2(k/k_0)}{4\gamma_\nu t}\right]. \tag{353}$$

This solution separates four related effects. First, the factor

$$M(k,t) \propto k^{3/2} \tag{354}$$

gives the characteristic Kazantsev spectrum beneath the evolving envelope. Second, completing the square in x gives

$$\sigma_{\ln k}^2 = \frac{2\gamma_\nu t}{5}, \tag{355}$$

so the spectrum broadens diffusively in $\ln k$. Third, differentiating Equation 353 with respect to x locates its peak.

$$\frac{\partial \ln M}{\partial x} = \frac{3}{2} - \frac{5x}{2\gamma_\nu t} = 0 \quad \Longrightarrow \quad \ln\left(\frac{k_\mathrm{p}}{k_0}\right) = \frac{3\gamma_\nu t}{5},$$
$$M_\mathrm{p} \equiv M(k_\mathrm{p}, t) = \frac{E_{\mathrm{mag},0}}{k_0}\left(\frac{5}{4\pi\gamma_\nu t}\right)^{1/2} \exp\left(\frac{6\gamma_\nu t}{5}\right). \tag{356}$$

Thus the peak wavenumber k_p and peak spectral density M_p both increase during the diffusion-free stage. Finally, integrating Equation 353 over k gives

$$E_\mathrm{mag}(t) \equiv \int_0^\infty M(k,t)\,\mathrm{d}k = E_{\mathrm{mag},0}\exp(2\gamma_\nu t). \tag{357}$$

The integral grows faster than the height of the spectrum because its support also broadens and moves toward larger k.

The viscous-scale strain connects all of these temporal rates to the Reynolds number. For Kolmogorov scaling,

$$\frac{\ell_\nu}{L} \sim \mathrm{Re}^{-3/4}, \qquad \frac{u_\nu}{U} \sim \mathrm{Re}^{-1/4}, \qquad \gamma_\nu \sim \frac{u_\nu}{\ell_\nu} \sim \frac{U}{L}\mathrm{Re}^{1/2}. \tag{358}$$

Consequently,

$$\frac{\mathrm{d}\sigma^2_{\ln k}}{\mathrm{d}t} = \frac{2\gamma_\nu}{5}, \qquad \frac{\mathrm{d}\ln k_\mathrm{p}}{\mathrm{d}t} = \frac{3\gamma_\nu}{5},$$
$$\frac{\mathrm{d}}{\mathrm{d}t}\ln\bigl(\sqrt{\gamma_\nu t}\,M_\mathrm{p}\bigr) = \frac{6\gamma_\nu}{5}, \qquad \frac{\mathrm{d}\ln E_\mathrm{mag}}{\mathrm{d}t} = 2\gamma_\nu, \tag{359}$$

Every temporal coefficient in Equation 359 therefore scales as

$$\text{spectral evolution rate} \propto \frac{U}{L}\mathrm{Re}^{1/2}. \tag{360}$$

The factor $(\gamma_\nu t)^{-1/2}$ gives the peak height a weak algebraic correction to its exponential growth.

Ohmic diffusion interrupts the diffusion-free solution when the moving peak approaches

$$k_\eta \sim \left(\frac{\gamma_\nu}{\eta}\right)^{1/2}, \tag{361}$$

consistent with Equation 329. Simulations at $\mathrm{Re} \gtrsim 100$ find

$$k_\mathrm{p} = (1.2 \pm 0.2)k_\eta, \qquad k_\eta \propto k_\nu \mathrm{Pm}^{1/2}, \qquad k_\nu \propto k_\mathrm{turb}\mathrm{Re}^{3/4} \tag{362}$$

(Kriel et al., 2022). The growth rate and terminal peak location therefore have different Reynolds-number scalings.

$$\text{rate of spectral motion} \propto \mathrm{Re}^{1/2}, \qquad \frac{k_{\mathrm{p,terminal}}}{k_\mathrm{turb}} \propto \mathrm{Re}^{3/4}\mathrm{Pm}^{1/2}. \tag{363}$$

Boundary conditions at the forcing and resistive scales select the allowed growth-rate eigenvalues and produce a finite critical Rm (Rincon, 2019, Secs. 3.4.5–3.4.8).

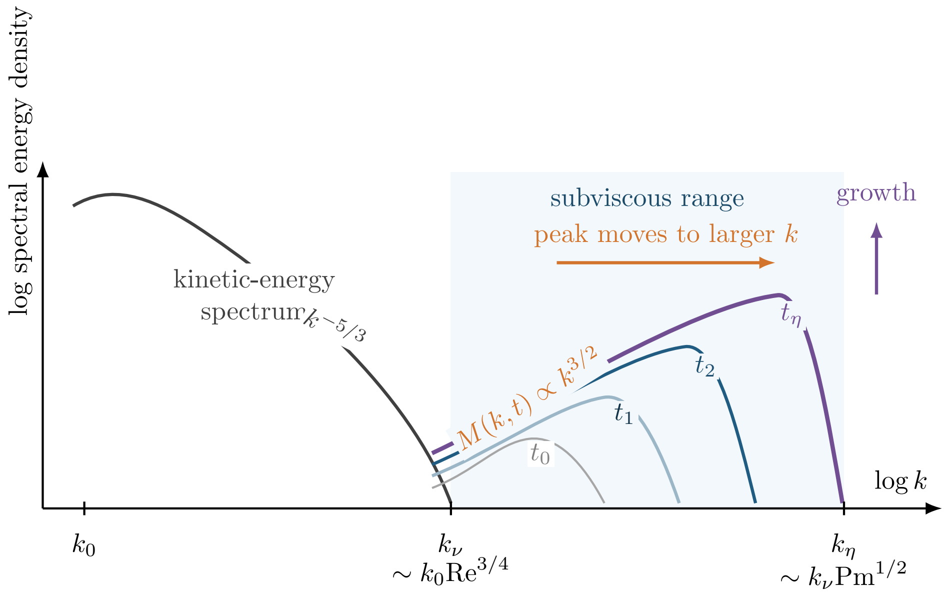

Figure 24. A schematic of the kinematic large-Pm spectral evolution, following Rincon (2019, Sec. 3.4.8 and Figs. 19–20). Viscous-scale strain amplifies the one-dimensional magnetic-energy spectrum $M(k,t)$ and spreads its peak through the subviscous interval $k_\nu < k < k_\eta$ at successive times $t_0 < t_1 < t_2 < t_\eta$. The rising part approaches the Kazantsev $M(k,t) \propto k^{3/2}$ form, and Ohmic diffusion fixes the terminal peak near the resistive wavenumber k_η. Here k_0 denotes the initial seed wavenumber near the forcing scale, while k_ν and k_η denote the viscous and resistive wavenumbers. Magnetic spectral energy at $k \gg k_\nu$ records rapid transverse reversals of the folded field; its parallel coherence and typical bend curvature remain tied to k_ν, as Figure 23 shows. Both schematic axes are logarithmic; $\mathrm{Re} = UL/\nu$ and $\mathrm{Pm} = \nu/\eta$.

Figure 24 gives the spectral counterpart of the folded geometry. viscous-scale strain creates magnetic structure throughout the subviscous range until resistivity arrests the motion of the peak near k_η.

26 Nonlinear small-scale dynamo

26.1 Magnetic tension first affects the smallest eddies

At large Pm, the viscous eddies drive the kinematic dynamo. Their stretching changes once magnetic tension becomes comparable to their inertial force. The rms magnetic field satisfies

$$B_{\mathrm{rms}}^2 \equiv \left\langle B^2 \right\rangle_{\mathcal{V}} = 2\mu_0 E_{\mathrm{mag}}. \tag{364}$$

The first eddies to feel magnetic tension obey the Batchelor-level balance

$$\frac{B_{\mathrm{rms}}^2}{\mu_0 \ell_\nu} \sim \frac{\rho_0 u_\nu^2}{\ell_\nu}, \qquad \frac{B_{\mathrm{rms}}^2}{\mu_0} \sim \rho_0 u_\nu^2. \tag{365}$$

Although the magnetic spectrum peaks near k_η, the force in this balance varies along a fold rather than across its short reversal scale. In particular,

$$\frac{1}{\mu_0} \left|(\boldsymbol{B} \cdot \boldsymbol{\nabla})\boldsymbol{B}\right| \sim \frac{B_{\mathrm{rms}}^2}{\mu_0 \ell_\parallel} \sim \frac{B_{\mathrm{rms}}^2}{\mu_0 \ell_\nu}. \tag{366}$$

The field reverses across ℓ_η, but its direction changes only gradually along $\ell_\parallel \sim \ell_\nu$. A resistive-scale magnetic field can therefore oppose the viscous-scale eddy that produced it. The back reaction couples two separated scales rather than requiring scale-by-scale equipartition (Schekochihin and Cowley, 2007, Sec. 3.2).

Both sides of the first relation are force densities. The mass density ρ_0 therefore multiplies the inertial term; it does not enter the magnetic-energy density. This Batchelor-level balance ends exponential growth but need not give the final magnetic energy. Larger eddies contain more kinetic energy and can continue stretching the field after the magnetic field suppresses the viscous-scale motions (Rincon, 2019, Secs. 3.5.1–3.5.2).

The first nonlinear response need not eliminate every viscous-scale motion. Magnetic tension preferentially reduces the field-aligned strain $\widehat{b}_i\widehat{b}_j\partial_j u_i$ that changes B. Velocity gradients that mix the folds without stretching them can remain, so the surviving velocity statistics become locally anisotropic relative to the fold direction. This selective weakening motivates the phrase "stretching motions remain unsuppressed" below (Schekochihin et al., 2004a).

26.2 Larger eddies continue to amplify the field

The symbol $\ell_*(t)$ denotes the smallest scale whose stretching motions remain unsuppressed. At that scale,

$$\frac{B_{\rm rms}^2(t)}{\mu_0} \sim \rho_0 u_{\ell_*}^2, \qquad \gamma_*(t) \sim \frac{u_{\ell_*}}{\ell_*}. \tag{367}$$

The induction estimate then gives

$$\frac{\mathrm{d}}{\mathrm{d}t}\left(\frac{B_{\rm rms}^2}{2\mu_0}\right) \sim \gamma_* \frac{B_{\rm rms}^2}{\mu_0} \sim \frac{\rho_0 u_{\ell_*}^3}{\ell_*} \sim \varepsilon. \tag{368}$$

Because the inertial-range power density ε does not depend on scale, the magnetic energy grows approximately linearly,

$$E_{\rm mag}(t) \sim E_{\rm mag}(t_{\rm nl}) + \zeta\varepsilon(t - t_{\rm nl}), \qquad 0 < \zeta < 1, \tag{369}$$

where $t_{\rm nl}$ marks the start of nonlinear growth and the dimensionless efficiency ζ measures the fraction of the cascade that feeds magnetic energy. The scale ℓ_* moves toward L until the field reaches a substantial fraction of outer-scale equipartition. Simulations support linear nonlinear growth, although the efficiency, interaction locality, and asymptotic saturation remain active questions (Schekochihin et al., 2002b, 2004b; Beresnyak, 2012).

The same argument predicts how the dynamically active and resistive scales move. The elapsed time and the three required scalings are

$$\begin{aligned} &\tau \equiv t - t_{\rm nl}, && E_{\rm mag} - E_{\rm mag}(t_{\rm nl}) \propto \tau, \\ &\frac{B_{\rm rms}^2}{\mu_0} \sim \rho_0 u_{\ell_*}^2, && \frac{\rho_0 u_{\ell_*}^3}{\ell_*} \sim \varepsilon. \end{aligned} \tag{370}$$

Combining these relations gives, up to constant efficiency factors,

$$u_{\ell_*} \propto \tau^{1/2}, \qquad \ell_* \propto \tau^{3/2}, \qquad \gamma_* \propto \tau^{-1}, \qquad \ell_\eta(t) \sim \left(\frac{\eta}{\gamma_*}\right)^{1/2} \propto (\eta\tau)^{1/2}. \tag{371}$$

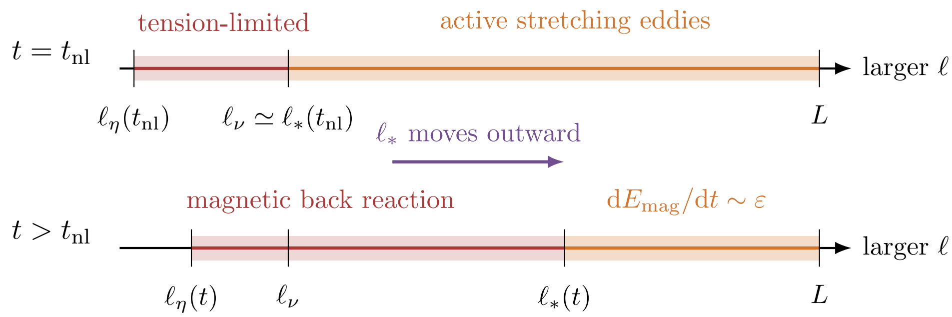

Figure 25. Nonlinear small-scale-dynamo growth advances from small to large eddies. At the onset time $t_{\rm nl}$, magnetic tension first modifies motions near the viscous scale, so $\ell_*(t_{\rm nl}) \simeq \ell_\nu$, while the resistive reversal scale $\ell_\eta(t_{\rm nl})$ remains smaller. At later time t, the boundary $\ell_*(t)$ between tension-limited and actively stretching eddies moves toward the outer scale L, and the weakening strain lets $\ell_\eta(t) \sim [\eta/\gamma_*(t)]^{1/2}$ increase. The remaining active cascade supplies magnetic energy density $E_{\rm mag}$ at a rate of order the inertial-range power density ε.

The weakening strain therefore allows the resistive reversal scale to increase along with the fold length; it does not remain fixed at its kinematic value.

The linear law in Equation 369 describes the subsonic branch rather than a universal law for compressible dynamos. Across a $\mathrm{Pm} = 1$ simulation ensemble, Kriel et al. (2026) measure

$$E_{\rm mag}(t) - E_{\rm mag}(t_{\rm nl}) \propto (t - t_{\rm nl})^{p_{\rm nl}}, \qquad p_{\rm nl} \simeq \begin{cases} 1, & \mathcal{M} < 1, \\ 2, & \mathcal{M} > 1, \end{cases} \tag{372}$$

where the sonic Mach number is

$$\mathcal{M} \equiv \frac{U}{c_s}, \tag{373}$$

and c_s denotes the sound speed. The same simulations find

$$\zeta \sim 10^{-2}, \qquad t_{\rm saturation} - t_{\rm nl} \sim 20\frac{L}{U}. \tag{374}$$

The supersonic quadratic branch shows that compressible dynamics can change the nonlinear growth law even when the kinematic mechanism remains magnetic stretching.

Figure 25 shows why the end of exponential growth at ℓ_ν does not imply immediate outer-scale saturation.

27 Large-scale dynamo from the mean field and turbulent EMF

27.1 Averaging the induction equation introduces the turbulent EMF

The mean field is not an imposed guide field. It is a dynamically generated component that varies on scales longer than the fluctuations and can remain compatible with a vanishing volume average. Split the full fields into means and fluctuations,

$$\boldsymbol{u} = \overline{\boldsymbol{u}} + \delta\boldsymbol{u}, \qquad \boldsymbol{B} = \overline{\boldsymbol{B}} + \boldsymbol{b}, \qquad \overline{\delta\boldsymbol{u}} = \overline{\boldsymbol{b}} = 0. \tag{375}$$

Applying an average that commutes with time and space derivatives to Equation 306 gives the exact mean induction equation

$$\partial_t \overline{\boldsymbol{B}} = \boldsymbol{\nabla} \times \left(\overline{\boldsymbol{u}} \times \overline{\boldsymbol{B}} + \boldsymbol{\mathcal{E}}\right) + \eta \nabla^2 \overline{\boldsymbol{B}}, \qquad \boldsymbol{\mathcal{E}} \equiv \overline{\delta \boldsymbol{u} \times \boldsymbol{b}}. \tag{376}$$

The turbulent electromotive force $\boldsymbol{\mathcal{E}}$ contains all effects of the eliminated fluctuations. Equation (376) remains exact, but it does not close because $\boldsymbol{b}$ depends on the evolving mean field and on its interaction with $\delta \boldsymbol{u}$.

27.2 The simplest local model for the EMF

Suppose the mean field varies on scales much longer than the velocity correlation length and time. Causality and linear response in the kinematic regime permit the local expansion

$$\mathcal{E}_i = a_{ij}\, \overline{B}_j + b_{ij\ell}\, \partial_\ell \overline{B}_j + \cdots . \tag{377}$$

The response tensors a_{ij} and $b_{ij\ell}$ connect the mean field and its first spatial gradient to the EMF. The ellipsis represents higher spatial derivatives and, when the fluctuations retain memory, a temporal convolution with the earlier mean field. Writing those terms as bare derivatives would be dimensionally incomplete because each derivative requires its own response coefficient. Homogeneous isotropic turbulence reduces the response tensors and the EMF to

$$a_{ij} = \alpha \delta_{ij}, \qquad b_{ij\ell} = -\beta \epsilon_{i\ell j}, \tag{378}$$

$$\boldsymbol{\mathcal{E}} = \alpha \overline{\boldsymbol{B}} - \beta \boldsymbol{\nabla} \times \overline{\boldsymbol{B}} + \cdots . \tag{379}$$

The left-hand side of Equation 379 is the turbulent EMF already defined in Equation 376; it is not an additional term in the induction equation. Equation (379) closes that EMF in terms of the mean magnetic field and its large-scale curl. The coefficient α has dimensions of velocity and changes sign under reflection, so mirror-symmetric turbulence forces $\alpha = 0$. The coefficient β has dimensions of diffusivity and augments the molecular magnetic diffusivity. Helical turbulence supplies the simplest route to a nonzero α effect (Rincon, 2019, Secs. 4.2–4.3.4).

27.3 Calculation of α and β by first-order smoothing

Subtracting Equation 376 from the full induction equation gives the exact fluctuation equation. For zero mean flow it reads

$$\partial_t \boldsymbol{b} - \eta \nabla^2 \boldsymbol{b} = \boldsymbol{\nabla} \times (\delta \boldsymbol{u} \times \overline{\boldsymbol{B}}) + \boldsymbol{\nabla} \times \left[\delta \boldsymbol{u} \times \boldsymbol{b} - \overline{\delta \boldsymbol{u} \times \boldsymbol{b}}\right]. \tag{380}$$

The quantity in square brackets has zero mean by construction. Since $\boldsymbol{\mathcal{E}} = \overline{\delta \boldsymbol{u} \times \boldsymbol{b}}$, this explicit mean subtraction is algebraically identical to writing $\delta \boldsymbol{u} \times \boldsymbol{b} - \boldsymbol{\mathcal{E}}$. Omitting it would make the average of the fluctuation equation nonzero.

In the short-correlation, high-Rm limit used here, first-order smoothing neglects the final nonlinear fluctuation term and resistive decay during one correlation time. More precisely, the ordering requires

$$\frac{\eta \tau_c}{\ell_u^2} \ll 1, \qquad \tau_c \ll \tau_{\overline{B}}, \tag{381}$$

where ℓ_u denotes the velocity correlation length and $\tau_{\overline{B}}$ denotes the evolution time of the mean field. For incompressible fields, integration over one correlation interval then gives

$$\boldsymbol{b} \simeq \tau_c \left[(\overline{\boldsymbol{B}} \cdot \boldsymbol{\nabla})\delta \boldsymbol{u} - (\delta \boldsymbol{u} \cdot \boldsymbol{\nabla})\overline{\boldsymbol{B}}\right]. \tag{382}$$

The component form of the turbulent EMF is

$$\mathcal{E}_i = \epsilon_{ijk}\overline{\delta u_j b_k}. \tag{383}$$

Substitution of Equation 382 into this definition yields

$$\mathcal{E}_i = \tau_c \epsilon_{ijk}\left[\overline{\delta u_j \partial_\ell \delta u_k}\,\overline{B}_\ell - \overline{\delta u_j \delta u_\ell}\,\partial_\ell \overline{B}_k\right]. \tag{384}$$

Isotropy permits only

$$\overline{\delta u_j \delta u_\ell} = \frac{1}{3}\overline{|\delta \boldsymbol{u}|^2}\,\delta_{j\ell}, \qquad \overline{\delta u_j \partial_\ell \delta u_k} = \frac{1}{6}\overline{\delta \boldsymbol{u}\cdot\delta\boldsymbol{\omega}}\,\epsilon_{j\ell k}, \qquad \delta\boldsymbol{\omega} \equiv \boldsymbol{\nabla}\times\delta\boldsymbol{u}. \tag{385}$$

The required Levi–Civita contraction is

$$\epsilon_{ijk}\epsilon_{j\ell k} = -2\delta_{i\ell}. \tag{386}$$

It gives

$$\boxed{\alpha = -\frac{\tau_c}{3}\overline{\delta \boldsymbol{u}\cdot\delta\boldsymbol{\omega}}, \qquad \beta = \frac{\tau_c}{3}\overline{|\delta\boldsymbol{u}|^2}.} \tag{387}$$

Thus fluctuating kinetic helicity $\overline{\delta \boldsymbol{u}\cdot\delta\boldsymbol{\omega}}$ produces a mean EMF parallel or antiparallel to $\overline{\boldsymbol{B}}$, while random advection produces turbulent magnetic diffusion. FOSA requires a controlled short-memory or weak-fluctuation ordering; ordinary turbulence often has

$$\mathrm{St} \equiv \frac{\tau_c}{\tau_{\mathrm{nl}}} \sim 1, \tag{388}$$

where τ_{nl} denotes the fluctuation turnover time. Therefore, Equation 387 provides a model rather than a universal identity (Rincon, 2019, Secs. 4.3.6–4.3.7).

The coefficients in Equation 387 close the mean induction equation and permit a direct calculation of large-scale growth.

28 Two elementary large-scale dynamos

28.1 Helicity overcomes diffusion in the α^2 dynamo

The simplest model uses constant α and constant total magnetic diffusivity,

$$\eta_{\mathrm{T}} \equiv \eta + \beta, \tag{389}$$

with zero mean flow. The mean induction equation becomes

$$\partial_t \overline{\boldsymbol{B}} = \alpha \boldsymbol{\nabla}\times\overline{\boldsymbol{B}} + \eta_{\mathrm{T}}\nabla^2\overline{\boldsymbol{B}}. \tag{390}$$

A solenoidal normal mode has the form

$$\overline{\boldsymbol{B}} = \Re\left[\widehat{\boldsymbol{B}}\,e^{\lambda t + i\boldsymbol{k}\cdot\boldsymbol{x}}\right], \qquad \boldsymbol{k}\cdot\widehat{\boldsymbol{B}} = 0 \tag{391}$$

where $\Re$ selects the real part, $\widehat{\boldsymbol{B}}$ denotes the complex magnetic amplitude, and $k = |\boldsymbol{k}|$, gives

$$\lambda\widehat{\boldsymbol{B}} = i\alpha\boldsymbol{k}\times\widehat{\boldsymbol{B}} - \eta_{\mathrm{T}}k^2\widehat{\boldsymbol{B}}. \tag{392}$$

For $\boldsymbol{k} = k\hat{\boldsymbol{z}}$, the helical polarizations

$$\widehat{B}_\pm \equiv \widehat{B}_x \pm i\widehat{B}_y \tag{393}$$

diagonalize the curl operator.

$$\lambda_\pm = \mp\alpha k - \eta_{\mathrm{T}} k^2. \tag{394}$$

One polarization grows when

$$|\alpha| k > \eta_{\mathrm{T}} k^2. \tag{395}$$

Maximizing its growth rate gives

$$k_{\max} = \frac{|\alpha|}{2\eta_{\mathrm{T}}}, \qquad \lambda_{\max} = \frac{\alpha^2}{4\eta_{\mathrm{T}}}. \tag{396}$$

28.2 Shear and helicity close the $\alpha\Omega$ loop

For the local shear flow

$$\overline{\boldsymbol{u}} = Sx\,\hat{\boldsymbol{y}} \tag{397}$$

the constant S is the shear rate. For the mean magnetic field

$$\overline{\boldsymbol{B}} = B_x(z,t)\hat{\boldsymbol{x}} + B_y(z,t)\hat{\boldsymbol{y}}, \tag{398}$$

the shear converts B_x into B_y, while the α effect converts B_y back into B_x.

$$\partial_t B_x = -\alpha\partial_z B_y + \eta_{\mathrm{T}}\partial_z^2 B_x, \tag{399}$$

$$\partial_t B_y = SB_x + \alpha\partial_z B_x + \eta_{\mathrm{T}}\partial_z^2 B_y. \tag{400}$$

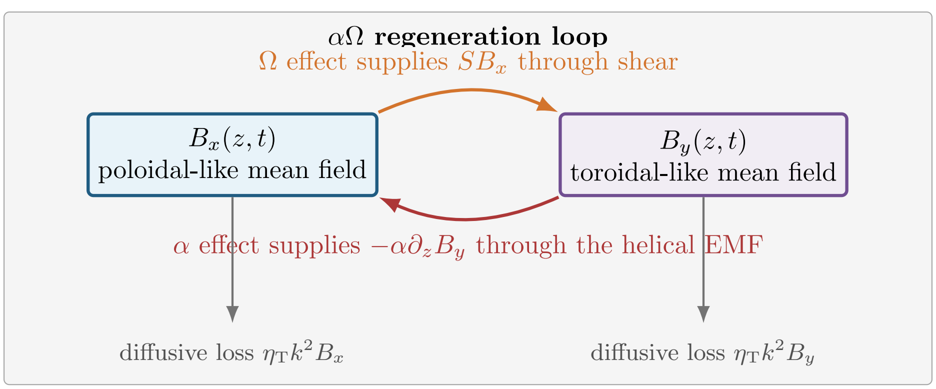

Figure 26. Shear and helical turbulence close the $\alpha\Omega$ regeneration loop. The poloidal-like component $B_x(z,t)$ feeds the toroidal-like component $B_y(z,t)$ through the shear term SB_x. The α effect returns B_y to B_x through the helical-EMF term $-\alpha\partial_z B_y$. Total magnetic diffusivity $\eta_{\mathrm{T}} = \eta + \beta$ removes a Fourier component of either field at the rate $\eta_{\mathrm{T}} k^2$, where k denotes its wavenumber.

Figure 26 displays the two conversions in Equation 399–(400). Large-scale growth requires their combined regeneration to outrun both diffusive loss terms.

The normal-mode ansatz is

$$\begin{pmatrix} B_x \\ B_y \end{pmatrix} = \begin{pmatrix} \widehat{B}_x \\ \widehat{B}_y \end{pmatrix} e^{\lambda t + ikz}. \tag{401}$$

Substitution into the two component equations gives

$$(\lambda + \eta_{\mathrm{T}} k^2) B_x = -i\alpha k B_y, \qquad (\lambda + \eta_{\mathrm{T}} k^2) B_y = (S + i\alpha k) B_x. \tag{402}$$

Eliminating the two amplitudes produces the dispersion relation

$$\left(\lambda + \eta_{\mathrm{T}} k^2\right)^2 = \alpha^2 k^2 - i\alpha S k. \tag{403}$$

In the strong-shear limit,

$$|S| \gg |\alpha k|, \tag{404}$$

the growing branch has

$$\Re(\lambda) \simeq \sqrt{\frac{|\alpha S k|}{2}} - \eta_{\mathrm{T}} k^2. \tag{405}$$

For a specified wavenumber, this branch grows when

$$|\alpha S| > 2\eta_{\mathrm{T}}^2 k^3. \tag{406}$$

Maximizing the strong-shear approximation gives

$$k_{\max} = \left(\frac{|\alpha S|}{32 \eta_{\mathrm{T}}^2} \right)^{1/3}, \qquad \Re(\lambda_{\max}) = 3\eta_{\mathrm{T}} k_{\max}^2. \tag{407}$$

The imaginary part describes a propagating dynamo wave. Equation (405) shows explicitly how shear supplies rapid toroidal amplification while helical turbulence regenerates the component that shear consumes. This mechanism underlies Parker (1955)'s classical dynamo-wave picture.

29 Where the simple fluid models stop

29.1 Small-scale growth can outpace mean-field growth

At large Rm, the fastest turbulent strain often excites the small-scale dynamo before a mean field changes appreciably. The fluctuating magnetic field then reaches nonlinear strength, invalidates a purely kinematic velocity ensemble, and alters the transport coefficients in Equation 379. A large-scale theory must therefore account for the saturated small-scale magnetic state rather than treating the fluctuations as passive noise (Rincon, 2019, Sec. 4.5).

29.2 Magnetic helicity constrains nonlinear large-scale growth

The vector potential $\boldsymbol{A}$ and magnetic helicity H_M satisfy

$$\boldsymbol{B} = \boldsymbol{\nabla} \times \boldsymbol{A}, \qquad H_M \equiv \langle \boldsymbol{A} \cdot \boldsymbol{B} \rangle_{\mathcal{V}}. \tag{408}$$

In a periodic domain with zero net magnetic flux, H_M is gauge invariant and obeys

$$\frac{\mathrm{d}H_M}{\mathrm{d}t} = -2\eta\mu_0 \langle \boldsymbol{J} \cdot \boldsymbol{B} \rangle_{\mathcal{V}}, \qquad \boldsymbol{J} \equiv \frac{1}{\mu_0} \boldsymbol{\nabla} \times \boldsymbol{B}. \tag{409}$$

Large Rm therefore makes total magnetic helicity nearly conserved. A helical large-scale field must generate compensating helicity at smaller scales or export helicity through a boundary. The resulting back reaction can strongly reduce α and slow saturation (Rincon, 2019; Brandenburg and Subramanian, 2005, Sec. 4.6.3).

29.3 Weakly collisional plasmas add feedback below fluid scales

The induction equation remains useful in many dilute astrophysical plasmas, but the isotropic-pressure MHD momentum equation can fail. Adiabatic invariance creates pressure anisotropy as the magnetic-field strength changes; firehose and mirror instabilities then regulate that anisotropy near ion-kinetic scales. Those processes can change the effective stress, stretching statistics, and route to saturation. A fluid dynamo therefore forms the starting point, not the final theory, for weakly collisional accretion flows and galaxy clusters (Rincon, 2019, Secs. 6.4–6.6).

30 Closing perspective

Four ideas recur throughout the discussion. Conservation laws determine what can change. Linearization determines how small disturbances propagate or grow. Nonlinear transfer moves energy among scales without creating or destroying the total. A dynamo instead converts kinetic energy into magnetic energy, while turbulent transfer redistributes both.

The simplest theories work because they isolate one mechanism at a time. Kolmogorov theory sets aside magnetic fields and compressibility. Reduced MHD assumes a strong local field and anisotropic fluctuations. The Kazantsev model replaces the velocity with a random smooth field, while elementary mean-field theory truncates the turbulent electromotive force after its lowest spatial derivatives. Each limit gives a clean calculation, but no single limit contains the whole dynamics of an accretion flow, a stellar interior, or a galaxy cluster.

The useful habit is therefore not to remember a spectral slope or growth rate in isolation. One should also ask which equation supplied it, which terms were retained, which invariant carried the flux, and which physical scale ends the approximation.

Part V

Derivations and mathematical details

A Divergence theorem and moving-volume transport

A sufficiently regular volume $\mathcal{V}$ has boundary $\partial\mathcal{V}$, outward unit normal $\hat{\boldsymbol{n}}$, volume element $\mathrm{d}V$, and boundary-area element $\mathrm{d}A$. For a differentiable scalar field ϕ, vector field $\boldsymbol{A}$, and second-order tensor field T, the scalar, vector, and tensor forms of the divergence theorem are, respectively,

$$\oint_{\partial\mathcal{V}} \phi\hat{\boldsymbol{n}}\,\mathrm{d}A = \int_{\mathcal{V}} \boldsymbol{\nabla}\phi\,\mathrm{d}V, \tag{410}$$

$$\oint_{\partial\mathcal{V}} \boldsymbol{A}\cdot\hat{\boldsymbol{n}}\,\mathrm{d}A = \int_{\mathcal{V}} \boldsymbol{\nabla}\cdot\boldsymbol{A}\,\mathrm{d}V, \tag{411}$$

$$\oint_{\partial\mathcal{V}} \mathsf{T}\cdot\hat{\boldsymbol{n}}\,\mathrm{d}A = \int_{\mathcal{V}} \boldsymbol{\nabla}\cdot\mathsf{T}\,\mathrm{d}V. \tag{412}$$

The tensor-divergence convention is $(\boldsymbol{\nabla}\cdot\mathsf{T})_i = \partial_j T_{ij}$, where $\partial_j = \partial/\partial x_j$. Repeated Cartesian indices imply summation, so applying the vector theorem to each row gives the last identity. For differentiable vector fields $\boldsymbol{a}$ and $\boldsymbol{b}$, for example,

$$[\boldsymbol{\nabla}\cdot(\boldsymbol{a}\otimes\boldsymbol{b})]_i = \partial_j(a_i b_j) = b_j\partial_j a_i + a_i\partial_j b_j, \tag{413}$$

or $\boldsymbol{\nabla}\cdot(\boldsymbol{a}\otimes\boldsymbol{b}) = (\boldsymbol{b}\cdot\boldsymbol{\nabla})\boldsymbol{a} + \boldsymbol{a}(\boldsymbol{\nabla}\cdot\boldsymbol{b})$.

The Reynolds transport theorem follows from the flow map $\boldsymbol{x} = \boldsymbol{\chi}(\boldsymbol{a},t)$ in (3). The deformation gradient is $F_{ij} = \partial\chi_i/\partial a_j$ and its Jacobian determinant $J = \det F$. The current volume element and reference volume element obey $\mathrm{d}V = J\,\mathrm{d}^3a$, where $\mathrm{d}^3a = \mathrm{d}a_1\,\mathrm{d}a_2\,\mathrm{d}a_3$. Jacobi's formula for a determinant gives

$$\frac{\mathrm{d}J}{\mathrm{d}t} = J\,\boldsymbol{\nabla}\cdot\boldsymbol{u}. \tag{414}$$

An overdot denotes a time derivative at fixed material label $\boldsymbol{a}$, and tr denotes the matrix trace. In detail, $\dot{J} = J\,\mathrm{tr}(F^{-1}\dot{F})$ and $(F^{-1})_{ji}\dot{F}_{ij} = \partial u_i/\partial x_i$. Therefore

$$\frac{\mathrm{d}}{\mathrm{d}t}\int_{\mathcal{V}(t)} q\,\mathrm{d}V = \frac{\mathrm{d}}{\mathrm{d}t}\int_{\mathcal{V}(0)} q(\boldsymbol{\chi}(\boldsymbol{a},t),t)J\,\mathrm{d}^3a \tag{415}$$

$$= \int_{\mathcal{V}(t)} \left[\frac{\mathrm{D}}{\mathrm{D}t}q + q\boldsymbol{\nabla}\cdot\boldsymbol{u}\right]\mathrm{d}V \tag{416}$$

$$= \int_{\mathcal{V}(t)} \left[\partial_t q + \boldsymbol{\nabla}\cdot(q\boldsymbol{u})\right]\mathrm{d}V, \tag{417}$$

which reproduces (8). Setting $q = 1$ and shrinking the material volume gives $(1/\mathrm{d}V)\mathrm{d}(\mathrm{d}V)/\mathrm{d}t = \boldsymbol{\nabla}\cdot\boldsymbol{u}$ for that moving element.

Finally, suppose a continuous function $h(\boldsymbol{x},t)$ obeys $\int_{\mathcal{V}} h\,\mathrm{d}V = 0$ for every volume $\mathcal{V}$. If h were positive or negative at some point, continuity would preserve that sign in a sufficiently small neighborhood and the integral over that neighborhood could not vanish. Hence $h = 0$ pointwise. This step, called *localization*, converts an arbitrary-volume conservation statement into a differential equation. Section 3.1 of Batchelor (2000) develops material integrals, their rates of change, and the same localization of integral conservation laws.

B General interface with gravity, shear, and magnetic tension

The main text sets both background velocities and magnetic fields to zero. This appendix allows them to be nonzero and derives the general uniform-half-space result, including shear and magnetic tension.

Plasma 1 occupies $z > 0$ and plasma 2 occupies $z < 0$. Both plasmas are semi-infinite, incompressible, and inviscid, and the interface has no surface tension. For $i \in \{1, 2\}$, plasma i has constant density ρ_i, tangential velocity $\boldsymbol{U}_i$, and tangential magnetic field $\boldsymbol{B}_i$. Gravity is $\boldsymbol{g} = -g\hat{\boldsymbol{z}}$, where $g > 0$. The displaced interface is

$$\xi(\boldsymbol{x}, t) = \widehat{\xi} e^{i(\boldsymbol{k}\cdot\boldsymbol{x}-\omega t)}, \qquad \boldsymbol{k}\cdot\hat{\boldsymbol{z}} = 0, \qquad k = |\boldsymbol{k}|. \tag{418}$$

Here $\boldsymbol{k}$ is the wavevector within the interface and k is its magnitude.

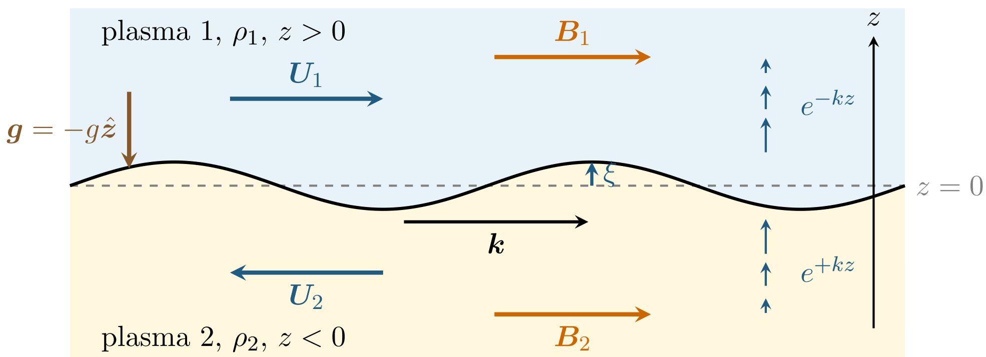

Figure 27. The general interface geometry. Two uniform plasmas meet at $z = 0$ and carry tangential velocities $\boldsymbol{U}_i$ and magnetic fields $\boldsymbol{B}_i$. Gravity points downward, the wavevector $\boldsymbol{k}$ lies along the interface, and ξ is its vertical displacement. The short vertical blue vectors represent perturbation velocity normal to the unperturbed interface; their amplitudes decay away from the sheet in both half-spaces.

B.1 Decaying solutions and the kinematic condition

The perturbation flow remains incompressible and irrotational in each uniform half-space. Writing $\boldsymbol{u}'_i = \boldsymbol{\nabla}\phi_i$ gives $\nabla^2\phi_i = 0$. The solutions that decay away from the interface are

$$\begin{aligned} \phi_1 &= A_1 e^{-kz} e^{i(\boldsymbol{k}\cdot\boldsymbol{x}-\omega t)}, \quad z > 0, \\ \phi_2 &= A_2 e^{+kz} e^{i(\boldsymbol{k}\cdot\boldsymbol{x}-\omega t)}, \quad z < 0. \end{aligned} \tag{419}$$

The frequency measured in the frame of plasma i is

$$\Omega_i = \omega - \boldsymbol{k}\cdot\boldsymbol{U}_i. \tag{420}$$

The kinematic boundary condition requires the interface to move with each plasma.

$$(\partial_t + \boldsymbol{U}_i\cdot\boldsymbol{\nabla})\xi = \partial_z\phi_i|_{z=0}\,. \tag{421}$$

Substitution of the normal modes gives

$$A_1 = \frac{i\Omega_1}{k}\widehat{\xi}, \qquad\qquad A_2 = -\frac{i\Omega_2}{k}\widehat{\xi}. \tag{422}$$

B.2 Fluid and magnetic pressure perturbations

The linearized momentum equation and its spatial integral are

$$\rho_i(\partial_t + \boldsymbol{U}_i \cdot \boldsymbol{\nabla})\boldsymbol{\nabla}\phi_i = -\boldsymbol{\nabla} p_i', \qquad p_i' = -\rho_i(\partial_t + \boldsymbol{U}_i \cdot \boldsymbol{\nabla})\phi_i = i\rho_i\Omega_i\phi_i, \tag{423}$$

where p_i' is the Eulerian pressure perturbation. At $z = 0$,

$$p_1' = -\frac{\rho_1\Omega_1^2}{k}\widehat{\xi}, \qquad p_2' = +\frac{\rho_2\Omega_2^2}{k}\widehat{\xi}. \tag{424}$$

The symbol $\delta\boldsymbol{B}_i$ denotes the magnetic perturbation in plasma i. For uniform $\boldsymbol{B}_i$, the linear induction equation becomes

$$(\partial_t + \boldsymbol{U}_i \cdot \boldsymbol{\nabla})\delta\boldsymbol{B}_i = (\boldsymbol{B}_i \cdot \boldsymbol{\nabla})\boldsymbol{u}_i'. \tag{425}$$

Writing $K_i = \boldsymbol{k} \cdot \boldsymbol{B}_i$ and substituting the normal modes gives

$$-i\Omega_i\delta\boldsymbol{B}_i = iK_i\boldsymbol{\nabla}\phi_i, \qquad \delta\boldsymbol{B}_i = -\frac{K_i}{\Omega_i}\boldsymbol{\nabla}\phi_i. \tag{426}$$

Only the tangential gradient contributes to the magnetic-pressure perturbation at the interface. Equations (422) and (426) therefore give

$$\boldsymbol{B}_1 \cdot \delta\boldsymbol{B}_1 = +\frac{K_1^2}{k}\widehat{\xi}, \qquad \boldsymbol{B}_2 \cdot \delta\boldsymbol{B}_2 = -\frac{K_2^2}{k}\widehat{\xi}. \tag{427}$$

The intermediate division assumes $\Omega_i \neq 0$; the continuous final relation also covers the limit $\Omega_i = 0$.

B.3 The combined dispersion relation

The background pressure satisfies $\partial_z p_{0i} = -\rho_i g$, while equilibrium requires $p_{01} + B_1^2/(2\mu_0) = p_{02} + B_2^2/(2\mu_0)$ at $z = 0$. Continuity of the Lagrangian total pressure at the displaced interface requires

$$\left(p_1' + \frac{\boldsymbol{B}_1 \cdot \delta\boldsymbol{B}_1}{\mu_0}\right) - \left(p_2' + \frac{\boldsymbol{B}_2 \cdot \delta\boldsymbol{B}_2}{\mu_0}\right) = g(\rho_1 - \rho_2)\widehat{\xi}. \tag{428}$$

Substitution of (424) and (427) gives

$$\boxed{\rho_1\Omega_1^2 + \rho_2\Omega_2^2 = gk(\rho_2 - \rho_1) + \frac{K_1^2 + K_2^2}{\mu_0}.} \tag{429}$$

The density-weighted mean velocity and velocity jump are

$$\overline{\boldsymbol{U}} = \frac{\rho_1\boldsymbol{U}_1 + \rho_2\boldsymbol{U}_2}{\rho_1 + \rho_2}, \qquad \Delta\boldsymbol{U} = \boldsymbol{U}_1 - \boldsymbol{U}_2. \tag{430}$$

Completing the density-weighted square yields

$$\rho_1\Omega_1^2 + \rho_2\Omega_2^2 = (\rho_1 + \rho_2)(\omega - \boldsymbol{k} \cdot \overline{\boldsymbol{U}})^2 + \frac{\rho_1\rho_2}{\rho_1 + \rho_2}(\boldsymbol{k} \cdot \Delta\boldsymbol{U})^2. \tag{431}$$

Dividing (429) by $\rho_1 + \rho_2$ gives

$$\boxed{\begin{aligned} &\omega = \boldsymbol{k} \cdot \overline{\boldsymbol{U}} \pm \sqrt{\mathcal{D}}, \\ &\mathcal{D} = \frac{gk(\rho_2 - \rho_1)}{\rho_1 + \rho_2} - \frac{\rho_1\rho_2}{(\rho_1 + \rho_2)^2}(\boldsymbol{k} \cdot \Delta\boldsymbol{U})^2 + \frac{(\boldsymbol{k} \cdot \boldsymbol{B}_1)^2 + (\boldsymbol{k} \cdot \boldsymbol{B}_2)^2}{\mu_0(\rho_1 + \rho_2)}. \end{aligned}} \tag{432}$$

The discriminant $\mathcal{D}$ has dimensions of frequency squared. Buoyancy, velocity shear, and magnetic tension supply its three terms. If $\mathcal{D} < 0$, the root with positive imaginary part grows at the rate $\gamma = \sqrt{-\mathcal{D}}$.

B.4 Recovery of the Rayleigh–Taylor result

Setting $\boldsymbol{U}_1 = \boldsymbol{U}_2 = \boldsymbol{U}_0$ and $\boldsymbol{B}_1 = \boldsymbol{B}_2 = 0$ reduces (432) to

$$(\omega - \boldsymbol{k}\cdot\boldsymbol{U}_0)^2 = \frac{gk(\rho_2 - \rho_1)}{\rho_1 + \rho_2}. \tag{433}$$

If the upper plasma is heavier, $\rho_1 > \rho_2$, the Atwood number

$$A = \frac{\rho_1 - \rho_2}{\rho_1 + \rho_2} > 0 \tag{434}$$

turns (433) into $(\omega - \boldsymbol{k}\cdot\boldsymbol{U}_0)^2 = -Agk$. Thus

$$\omega = \boldsymbol{k}\cdot\boldsymbol{U}_0 \pm i\sqrt{Agk}, \qquad \boxed{\gamma_{\mathrm{RT}} = \sqrt{Agk}.} \tag{435}$$

Gravity supplies the free energy because exchanging heavy material above with light material below lowers the potential energy. In the stationary frame $\boldsymbol{U}_0 = 0$, this result recovers (139).

B.5 Unequal-density Kelvin–Helmholtz limit

Setting $g = 0$ and $\boldsymbol{B}_i = 0$ gives

$$(\omega - \boldsymbol{k}\cdot\overline{\boldsymbol{U}})^2 = -\frac{\rho_1\rho_2}{(\rho_1 + \rho_2)^2}(\boldsymbol{k}\cdot\Delta\boldsymbol{U})^2. \tag{436}$$

The growing root has

$$\boxed{\gamma_{\mathrm{KH}} = \frac{\sqrt{\rho_1\rho_2}}{\rho_1 + \rho_2}|\boldsymbol{k}\cdot\Delta\boldsymbol{U}|.} \tag{437}$$

For equal densities and $\boldsymbol{k} \parallel \Delta\boldsymbol{U}$, defining $\Delta U = |\Delta\boldsymbol{U}|$ reduces this expression to $\gamma_{\mathrm{KH}} = k\Delta U/2$.

B.6 Magnetic stabilization

For equal densities, equal magnetic fields parallel to $\boldsymbol{k}$, and no gravity, (432) gives

$$\gamma^2 = k^2\left(\frac{\Delta U^2}{4} - v_{\mathrm{A}}^2\right), \qquad v_{\mathrm{A}} = \frac{B}{\sqrt{\mu_0\rho}}. \tag{438}$$

Here $\rho_1 = \rho_2 = \rho$ and $B = |\boldsymbol{B}_1| = |\boldsymbol{B}_2|$. The field stabilizes the ideal interface when $\Delta U < 2v_{\mathrm{A}}$. If $\boldsymbol{k}\cdot\boldsymbol{B}_i = 0$, the perturbation does not bend the field and the magnetic-tension term vanishes.

Chapter X, Sections 90–92 and 97 and Chapter XI, Sections 100–101 and 106 of Chandrasekhar (1961) derive the gravitational, shear-driven, and magnetized limits. Chapter 3, Sections 3.1–3.8 of Drazin (2002) provide a shorter hydrodynamic development. Sections 6.6.1 and 6.6.4 and Chapter 13, Sections 13.1.2 and 13.2.1–13.2.3 of Goedbloed et al. (2019) place the combined interface problem within MHD spectral theory.

C Moments of a probability density

For a scalar random variable X with probability density $p_X(x)$, the nth raw moment and nth central moment are

$$m_n \equiv \mathbb{E}[X^n] = \int_{-\infty}^{\infty} x^n p_X(x)\,\mathrm{d}x, \tag{439}$$

$$\mu_n \equiv \mathbb{E}[(X-\mu)^n] = \int_{-\infty}^{\infty} (x-\mu)^n p_X(x)\,\mathrm{d}x, \tag{440}$$

$$\mu \equiv m_1. \tag{441}$$

Assuming that these integrals converge, the first four moments describe different features of the distribution.

First raw moment, m_1	The mean μ locates the centre of the distribution. The first central moment vanishes identically, $\mu_1 = 0$.
Second central moment, μ_2	The variance $\sigma^2 = \mu_2$ measures the squared width; σ is the standard deviation.
Third central moment, μ_3	The standardized skewness $\gamma_1 = \mu_3/\sigma^3$ measures left–right asymmetry. Positive skewness indicates the longer right tail.
Fourth central moment, μ_4	The kurtosis $\beta_2 = \mu_4/\sigma^4$ measures the weight of rare, extreme deviations. A Gaussian has $\beta_2 = 3$, or excess kurtosis $\beta_2 - 3 = 0$.

At fixed separation r, the signed longitudinal increment $q \equiv \delta u_L$ has a density $p_r(q)$. Its signed and absolute moments are

$$S_{n,L}(r) = \mathbb{E}[q^n] = \int_{-\infty}^{\infty} q^n p_r(q)\,\mathrm{d}q, \tag{442}$$

$$S_p^{|\cdot|}(r) = \mathbb{E}[|q|^p] = \int_{-\infty}^{\infty} |q|^p p_r(q)\,\mathrm{d}q. \tag{443}$$

Homogeneity gives $\mathbb{E}[q] = 0$, so $S_{2,L}$ is the variance and $S_{3,L}$ is the unnormalized signed third central moment of q. Increasing p in the absolute moment gives rare, large-amplitude increments progressively greater weight, but removes their sign.

D Power spectra and second-order structure functions

The Wiener–Khinchin relation makes a two-point correlation and its power spectrum a Fourier-transform pair. Combining that relation with Equation 204 connects the energy spectrum directly to a second-order structure function. For a homogeneous, isotropic, incompressible velocity field and the shell-integrated spectrum normalized by Equation 205, the total second-order structure function is

$$S_2(r) \equiv \left\langle |\delta \boldsymbol{u}|^2 \right\rangle = 4\int_0^{\infty} E(k)\left[1 - \frac{\sin(kr)}{kr}\right]\mathrm{d}k. \tag{444}$$

The corresponding longitudinal relation is

$$S_{2,L}(r) = 4\int_0^{\infty} E(k)\left[\frac{1}{3} - \frac{\sin(kr) - kr\cos(kr)}{(kr)^3}\right]\mathrm{d}k. \tag{445}$$

The two kernels vanish when $kr \ll 1$, because a mode with wavelength much larger than r produces nearly the same velocity at both points. Modes with $kr \gtrsim 1$ contribute to the increment, so a separation r probes a range of wavenumbers centred around $k \sim r^{-1}$.

For an inertial-range spectrum $E(k) \propto k^{-\alpha}$ with $1 < \alpha < 3$, the change of variable $x = kr$ gives

$$S_2(r) \propto r^{\alpha-1}, \qquad S_{2,L}(r) \propto r^{\alpha-1}. \tag{446}$$

Consequently,

$$\boxed{E(k) \propto k^{-5/3} \quad \Longleftrightarrow \quad S_2(r),\, S_{2,L}(r) \propto r^{2/3}.} \tag{447}$$

This correspondence holds over matching scale ranges under the stated symmetry assumptions; it does not identify a single separation r with a single Fourier mode $k = 1/r$.

E Complete two-point derivation of the Kármán–Howarth–Monin equation

Chapter 6, Section 6.3 of Pope (2000) and Chapter 6, Section 6.2.1 of Frisch (1995) provide source derivations and complementary notation for this calculation.

An unprimed field denotes evaluation at $\boldsymbol{x}$, and a primed field denotes evaluation at $\boldsymbol{x}' = \boldsymbol{x} + \boldsymbol{r}$.

$$u_i \equiv u_i(\boldsymbol{x}, t), \qquad u_i' \equiv u_i(\boldsymbol{x}', t), \qquad \delta u_i \equiv u_i' - u_i, \tag{448}$$

with analogous notation for p, f_i, and their increments. The two incompressible Navier–Stokes equations are

$$\partial_t u_i + u_j \partial_j u_i = -\rho^{-1}\partial_i p + \nu \nabla^2 u_i + f_i, \qquad \partial_i u_i = 0, \tag{449}$$

$$\partial_t u_i' + u_j' \partial_j' u_i' = -\rho^{-1}\partial_i' p' + \nu \nabla'^2 u_i' + f_i', \qquad \partial_i' u_i' = 0. \tag{450}$$

Subtracting Equation 449 from Equation 450 gives

$$\partial_t \delta u_i + u_j' \partial_j' u_i' - u_j \partial_j u_i = -\rho^{-1}(\partial_i' p' - \partial_i p) + \nu(\nabla'^2 u_i' - \nabla^2 u_i) + \delta f_i. \tag{451}$$

Multiplication by $2\delta u_i$ converts the time derivative into

$$2\delta u_i \partial_t \delta u_i = \partial_t |\delta \boldsymbol{u}|^2. \tag{452}$$

For a homogeneous average, differentiation with respect to the midpoint vanishes. The sum and difference of point derivatives therefore satisfy

$$\partial_{x_i'} \langle Q \rangle + \partial_{x_i} \langle Q \rangle = 0, \qquad \partial_{r_i} \langle Q \rangle = \partial_{x_i'} \langle Q \rangle = -\partial_{x_i} \langle Q \rangle, \tag{453}$$

for any two-point quantity Q. Expanding the advective contribution, integrating derivatives by parts inside the homogeneous average, and using $\partial_j u_j = \partial_j' u_j' = 0$ gives four products that regroup as

$$2\left\langle \delta u_i \left(u_j' \partial_j' u_i' - u_j \partial_j u_i\right)\right\rangle = \partial_{r_j}\left\langle (u_j' - u_j)|\delta \boldsymbol{u}|^2\right\rangle = \partial_{r_j}\left\langle \delta u_j |\delta \boldsymbol{u}|^2\right\rangle. \tag{454}$$

This identity makes the conservative role of the nonlinear term explicit.

The pressure contribution vanishes after averaging. Its primed part expands as

$$\left\langle \delta u_i \partial_i' p' \right\rangle = \left\langle u_i' \partial_i' p' \right\rangle - \left\langle u_i \partial_i' p' \right\rangle$$

$$= \left\langle \partial_i'(u_i'p') \right\rangle - \partial_{r_i} \left\langle u_i p' \right\rangle = 0. \tag{455}$$

The first term vanishes as a homogeneous divergence. For the second, homogeneity and incompressibility give

$$\partial_{r_i} \left\langle u_i(\boldsymbol{x}) p(\boldsymbol{x}') \right\rangle = - \left\langle p(\boldsymbol{x}') \partial_i u_i(\boldsymbol{x}) \right\rangle = 0. \tag{456}$$

The unprimed contribution vanishes in the same way,

$$\langle \delta u_i \partial_i p \rangle = \left\langle u_i' \partial_i p \right\rangle - \langle u_i \partial_i p \rangle = 0, \tag{457}$$

because homogeneity converts the first term into a primed velocity divergence and the second is a one-point divergence. Pressure therefore drops out of the trace of the homogeneous two-point energy equation.

Next, expansion of the viscous term uses homogeneity to equate the one-point gradient variances at $\boldsymbol{x}$ and $\boldsymbol{x}'$, and two integrations by parts give

$$2\nu \left\langle \delta u_i (\nabla'^2 u_i' - \nabla^2 u_i) \right\rangle = 2\nu \nabla_{\boldsymbol{r}}^2 \left\langle |\delta \boldsymbol{u}|^2 \right\rangle - 4\nu \left\langle \partial_j u_i \, \partial_j u_i \right\rangle. \tag{458}$$

For an incompressible field with a vanishing boundary contribution,

$$\nu \left\langle \partial_j u_i \, \partial_j u_i \right\rangle = 2\nu \left\langle S_{ij} S_{ij} \right\rangle \equiv \varepsilon. \tag{459}$$

Finally, the forcing contribution is simply

$$2 \langle \delta u_i \delta f_i \rangle = 2 \langle \delta \boldsymbol{u} \cdot \delta \boldsymbol{f} \rangle. \tag{460}$$

Combining Equation 452, Equation 454, Equation 455, Equation 458, and Equation 460 recovers

$$\partial_t \left\langle |\delta \boldsymbol{u}|^2 \right\rangle + \partial_{r_j} \left\langle \delta u_j |\delta \boldsymbol{u}|^2 \right\rangle = 2\nu \nabla_{\boldsymbol{r}}^2 \left\langle |\delta \boldsymbol{u}|^2 \right\rangle - 4\varepsilon + 2 \langle \delta \boldsymbol{u} \cdot \delta \boldsymbol{f} \rangle, \tag{461}$$

which is Equation 207.

F Longitudinal and transverse laws from the isotropic third-order tensor

Chapter 6, Section 6.3 of Pope (2000) and Chapter 6, Sections 6.2.3–6.2.4 of Frisch (1995) develop the isotropic reduction used below.

Aligning the first coordinate axis with $\hat{\boldsymbol{r}}$ identifies one transverse component δu_T. Isotropy makes the two transverse directions statistically equivalent. The longitudinal component of the mixed flux is therefore

$$Y_L = \left\langle \delta u_L |\delta \boldsymbol{u}|^2 \right\rangle = \underbrace{\left\langle (\delta u_L)^3 \right\rangle}_{S_{3,L}} + 2 \underbrace{\left\langle \delta u_L (\delta u_T)^2 \right\rangle}_{S_{LTT}}. \tag{462}$$

The most general isotropic, fully symmetric third-order increment tensor has the form

$$B_{ijk}(\boldsymbol{r}) \equiv \langle \delta u_i \delta u_j \delta u_k \rangle = A(r) \hat{\boldsymbol{r}}_i \hat{\boldsymbol{r}}_j \hat{\boldsymbol{r}}_k + B(r) \left(\hat{\boldsymbol{r}}_i \delta_{jk} + \hat{\boldsymbol{r}}_j \delta_{ik} + \hat{\boldsymbol{r}}_k \delta_{ij} \right). \tag{463}$$

With $\hat{\boldsymbol{r}}$ along the first coordinate,

$$S_{3,L} = B_{111} = A + 3B, \qquad S_{LTT} = B_{122} = B. \tag{464}$$

Incompressibility applied to the underlying two-point triple correlation supplies one differential constraint between the two scalar functions. Substitution of Equation 463 and differentiation of $\partial_{r_i} r = r_i/r$ and $\partial_{r_i}\hat{\boldsymbol{r}}_j = (\delta_{ij} - \hat{\boldsymbol{r}}_i\hat{\boldsymbol{r}}_j)/r$ give

$$r(A' + 3B') + A - 3B = 0, \tag{465}$$

where a prime on A or B denotes $\mathrm{d}/\mathrm{d}r$. Since $S_{3,L} = A + 3B$, Equation 465 becomes

$$rS'_{3,L} + S_{3,L} - 6B = 0, \qquad S_{LTT} = B = \frac{1}{6}\frac{\mathrm{d}}{\mathrm{d}r}\left(rS_{3,L}\right). \tag{466}$$

Inserting this result into Equation 462 gives

$$Y_L = S_{3,L} + \frac{1}{3}\frac{\mathrm{d}}{\mathrm{d}r}(rS_{3,L}) = \frac{4}{3}S_{3,L} + \frac{r}{3}S'_{3,L} = \boxed{\frac{1}{3r^3}\frac{\mathrm{d}}{\mathrm{d}r}\left(r^4 S_{3,L}\right)}, \tag{467}$$

which proves Equation 213. Combining this identity with $Y_L = -(4/3)\varepsilon r$ gives both

$$S_{3,L} = -\frac{4}{5}\varepsilon r, \qquad S_{LTT} = -\frac{4}{15}\varepsilon r. \tag{468}$$

The second relation is the four-fifteenths law for either one of the transverse components.

G Complete spectral derivation of the Fourier-space energy equation

Chapter 6, Sections 6.4.2–6.4.3 and 6.6 of Pope (2000) and Chapter 2, Section 2.4 of Frisch (1995) provide complementary modal and filtered derivations of spectral transfer.

Let $\mathcal{D}$ be a periodic domain of positive volume $\mathcal{V}$, and let $\boldsymbol{k}$ run over its reciprocal-lattice wavevectors. The volume-normalized Fourier-series convention is

$$\widehat{u}_i(\boldsymbol{k}, t) = \frac{1}{\mathcal{V}}\int_{\mathcal{D}} u_i(\boldsymbol{x}, t)e^{-i\boldsymbol{k}\cdot\boldsymbol{x}}\,\mathrm{d}V, \qquad u_i(\boldsymbol{x}, t) = \sum_{\boldsymbol{k}} \widehat{u}_i(\boldsymbol{k}, t)e^{i\boldsymbol{k}\cdot\boldsymbol{x}}. \tag{469}$$

Parseval's identity then gives $\langle|\boldsymbol{u}|^2\rangle = \sum_{\boldsymbol{k}} \widehat{u}_i^*(\boldsymbol{k})\widehat{u}_i(\boldsymbol{k})$, where the average is over $\mathcal{D}$. As in the spectral discussion in the main text, the mean velocity and hence the zero mode vanish, so $K = \langle|\boldsymbol{u}|^2\rangle/2$. Thus every modal energy below has units of kinetic energy per unit mass, consistently with Equation 205. The incompressibility condition becomes $k_i\widehat{u}_i = 0$. Writing the advective term in conservative form, $u_j\partial_j u_i = \partial_j(u_j u_i)$, and transforming it gives

$$\widehat{\partial_j(u_j u_i)}(\boldsymbol{k}) = ik_j \sum_{\boldsymbol{q}} \widehat{u}_j(\boldsymbol{q})\widehat{u}_i(\boldsymbol{k} - \boldsymbol{q}). \tag{470}$$

Thus only triads $\boldsymbol{k} = \boldsymbol{q} + \boldsymbol{p}$, with $\boldsymbol{p} = \boldsymbol{k} - \boldsymbol{q}$, interact.

Applying the projection tensor $P_{i\ell}(\boldsymbol{k})$ from Equation 220 removes the pressure gradient because $P_{i\ell}k_\ell = 0$ and gives the mode equation

$$\partial_t\widehat{u}_i(\boldsymbol{k}) = -\nu k^2\widehat{u}_i(\boldsymbol{k}) + \widehat{f}_i^{\perp}(\boldsymbol{k}) - iP_{i\ell}(\boldsymbol{k})k_j \sum_{\boldsymbol{q}} \widehat{u}_j(\boldsymbol{q})\widehat{u}_\ell(\boldsymbol{k} - \boldsymbol{q}), \tag{471}$$

where $\widehat{f}_i^{\perp} = P_{i\ell}\widehat{f}_\ell$ is the solenoidal part of the forcing.

The energy density of a Fourier mode is

$$\Phi(\boldsymbol{k},t) \equiv \frac{1}{2}\widehat{u}_i^*(\boldsymbol{k},t)\widehat{u}_i(\boldsymbol{k},t), \tag{472}$$

where the asterisk denotes complex conjugation. Multiplying Equation 471 by $\widehat{u}_i^*$, adding the complex conjugate, and dividing by two gives

$$\partial_t\Phi(\boldsymbol{k}) = \mathcal{T}(\boldsymbol{k}) + \mathcal{P}_f(\boldsymbol{k}) - 2\nu k^2\Phi(\boldsymbol{k}), \tag{473}$$

where

$$\mathcal{P}_f(\boldsymbol{k}) = \mathrm{Re}\Big[\widehat{u}_i^*(\boldsymbol{k})\widehat{f}_i^{\perp}(\boldsymbol{k})\Big], \tag{474}$$

$$\mathcal{T}(\boldsymbol{k}) = -\,\mathrm{Re}\left[i\widehat{u}_i^*(\boldsymbol{k})P_{i\ell}(\boldsymbol{k})k_j\sum_{\boldsymbol{q}}\widehat{u}_j(\boldsymbol{q})\widehat{u}_\ell(\boldsymbol{k}-\boldsymbol{q})\right]. \tag{475}$$

The operator Re selects the real part.

The Dirac delta δ_{D} converts the discrete modes in the periodic domain into one-dimensional shell spectra.

$$E(k) \equiv \sum_{\boldsymbol{k}}\Phi(\boldsymbol{k})\delta_{\mathrm{D}}(k-|\boldsymbol{k}|), \quad T(k) \equiv \sum_{\boldsymbol{k}}\mathcal{T}(\boldsymbol{k})\delta_{\mathrm{D}}(k-|\boldsymbol{k}|), \quad F(k) \equiv \sum_{\boldsymbol{k}}\mathcal{P}_f(\boldsymbol{k})\delta_{\mathrm{D}}(k-|\boldsymbol{k}|). \tag{476}$$

Consequently, $\int_0^\infty E(k)\,\mathrm{d}k = \sum_{\boldsymbol{k}}\Phi(\boldsymbol{k}) = K$. Practical shell averaging smooths the delta functions into finite-width bins, and the large-box limit produces the continuous spectrum used in the main text. Summing Equation 473 over each shell gives Equation 224.

Finally, the nonlinear contribution integrated over all modes is the Fourier representation of the physical-space integral

$$\frac{1}{\mathcal{V}}\int_{\mathcal{D}} u_iu_j\partial_ju_i\,\mathrm{d}V = \frac{1}{\mathcal{V}}\int_{\mathcal{D}}\partial_j\left(\frac{1}{2}u_iu_iu_j\right)\mathrm{d}V = 0 \tag{477}$$

in a periodic domain or under vanishing surface flux. Parseval's identity therefore gives

$$\int_0^\infty T(k)\,\mathrm{d}k = 0, \tag{478}$$

which proves Equation 223 and completes the spectral derivation.

H The perpendicular Elsasser system from reduced-MHD ordering

This appendix makes the ordering behind Equation 246 explicit. It adopts the strong distinguished limit $\epsilon_z \sim \epsilon_k \sim \epsilon_{\mathrm{RMHD}} \ll 1$, in which Alfvén propagation and perpendicular nonlinear shearing enter at the same asymptotic order. Split every vector and gradient into guide-field-parallel and perpendicular parts,

$$\boldsymbol{z}^{\pm} = \boldsymbol{z}_\perp^{\pm} + z_\parallel^{\pm}\hat{\boldsymbol{e}}_\parallel, \qquad\qquad \boldsymbol{\nabla} = \boldsymbol{\nabla}_\perp + \hat{\boldsymbol{e}}_\parallel\partial_\parallel. \tag{479}$$

The shear-Alfvén sector uses

$$\frac{|\boldsymbol{z}_\perp^{\pm}|}{v_{\mathrm{A}}} \sim \epsilon_{\mathrm{RMHD}}, \qquad \frac{|z_\parallel^{\pm}|}{v_{\mathrm{A}}} \sim \epsilon_{\mathrm{RMHD}}^2, \qquad \frac{\partial_\parallel}{|\boldsymbol{\nabla}_\perp|} \sim \epsilon_{\mathrm{RMHD}}, \qquad \partial_t \sim v_{\mathrm{A}}\partial_\parallel, \qquad \epsilon_{\mathrm{RMHD}} \ll 1. \tag{480}$$

Allowing $z_\parallel^\pm/v_\mathrm{A} \sim \epsilon_\mathrm{RMHD}$ adds pseudo-Alfvén fluctuations that the leading perpendicular fields passively mix; it does not change the closed perpendicular system derived below.

The leading time derivative, guide-field propagation, and perpendicular nonlinearity all scale as

$$\partial_t \boldsymbol{z}_\perp^\pm \sim v_\mathrm{A}\partial_\parallel \boldsymbol{z}_\perp^\pm \sim \boldsymbol{z}_\perp^\mp \cdot \boldsymbol{\nabla}_\perp \boldsymbol{z}_\perp^\pm \sim \epsilon_\mathrm{RMHD}^2 v_\mathrm{A}^2 k_\perp. \tag{481}$$

The terms involving a parallel fluctuation are smaller.

$$z_\parallel^\mp \partial_\parallel \boldsymbol{z}_\perp^\pm \sim \epsilon_\mathrm{RMHD}^4 v_\mathrm{A}^2 k_\perp, \qquad \boldsymbol{z}_\perp^\mp \cdot \boldsymbol{\nabla}_\perp (z_\parallel^\pm \hat{\boldsymbol{e}}_\parallel) \sim \epsilon_\mathrm{RMHD}^3 v_\mathrm{A}^2 k_\perp. \tag{482}$$

The perpendicular pressure gradient must balance the leading terms, so $P_\mathrm{tot} \sim |\boldsymbol{z}_\perp^\pm|^2 \sim \epsilon_\mathrm{RMHD}^2 v_\mathrm{A}^2$. Incompressibility gives

$$\boldsymbol{\nabla}_\perp \cdot \boldsymbol{z}_\perp^\pm = -\partial_\parallel z_\parallel^\pm \sim \epsilon_\mathrm{RMHD}^3 v_\mathrm{A} k_\perp, \tag{483}$$

so $\boldsymbol{\nabla}_\perp \cdot \boldsymbol{z}_\perp^\pm = 0$ at the retained order.

Projecting Equation 238 perpendicular to $\hat{\boldsymbol{e}}_\parallel$, dropping terms beyond $\mathcal{O}\big(\epsilon_\mathrm{RMHD}^2 v_\mathrm{A}^2 k_\perp\big)$, and retaining the dominant perpendicular diffusion gives

$$\partial_t \boldsymbol{z}_\perp^\pm \mp v_\mathrm{A}\partial_\parallel \boldsymbol{z}_\perp^\pm + \boldsymbol{z}_\perp^\mp \cdot \boldsymbol{\nabla}_\perp \boldsymbol{z}_\perp^\pm = -\boldsymbol{\nabla}_\perp P_\mathrm{tot} + \nu \nabla_\perp^2 \boldsymbol{z}_\perp^\pm + \boldsymbol{f}_\perp^\pm, \tag{484}$$

which is Equation 246. Taking $\boldsymbol{\nabla}_\perp \cdot$ of this equation and using perpendicular solenoidality gives Equation 247. The distinguished ordering therefore retains linear propagation and nonlinear distortion at the same asymptotic order. After deriving the closed perpendicular system, choosing solutions with $\epsilon_z \ll \epsilon_k$ gives $\chi \ll 1$ and the weak-RMHD regime, in which nonlinear distortion is small during one crossing but accumulates over the longer cascade time. Reduced MHD therefore defines the guide-field geometry and perpendicular dynamics, while χ distinguishes weak from strong interactions within that system.

I Complete two-point derivation of the Politano–Pouquet relation

For clarity, this derivation takes $\nu = \eta$ and suppresses the $\pm$ label until the final line. The symbols $a_i = z_i^\pm$ and $c_j = z_j^\mp$ denote the advected field and counterpropagating advector. At $\boldsymbol{x}$ and $\boldsymbol{x}' = \boldsymbol{x} + \boldsymbol{r}$,

$$\partial_t a_i + c_j \partial_j a_i = \pm v_\mathrm{A} \partial_\parallel a_i - \partial_i P_\mathrm{tot} + \nu \nabla^2 a_i + f_i, \tag{485}$$

$$\partial_t a_i' + c_j' \partial_j' a_i' = \pm v_\mathrm{A} \partial_\parallel' a_i' - \partial_i' P_\mathrm{tot}' + \nu \nabla'^2 a_i' + f_i'. \tag{486}$$

Subtracting Equation 485 from Equation 486, multiplying by $2\delta a_i = 2(a_i' - a_i)$, and averaging gives

$$\begin{aligned}
\partial_t \left\langle |\delta \boldsymbol{a}|^2 \right\rangle &+ 2\left\langle \delta a_i (c_j' \partial_j' a_i' - c_j \partial_j a_i) \right\rangle \\
&= \pm 2 v_\mathrm{A} \left\langle \delta a_i (\partial_\parallel' a_i' - \partial_\parallel a_i) \right\rangle - 2\left\langle \delta a_i (\partial_i' P_\mathrm{tot}' - \partial_i P_\mathrm{tot}) \right\rangle \\
&\quad + 2\nu \left\langle \delta a_i (\nabla'^2 a_i' - \nabla^2 a_i) \right\rangle + 2\left\langle \delta \boldsymbol{a} \cdot \delta \boldsymbol{f} \right\rangle.
\end{aligned} \tag{487}$$

Homogeneity removes derivatives with respect to the midpoint $\boldsymbol{X} = (\boldsymbol{x} + \boldsymbol{x}')/2$. Incompressibility then converts the nonlinear term into

$$2\left\langle \delta a_i (c_j' \partial_j' a_i' - c_j \partial_j a_i) \right\rangle = \frac{\partial}{\partial r_j} \left\langle \delta c_j |\delta \boldsymbol{a}|^2 \right\rangle. \tag{488}$$

The linear propagation term is a midpoint derivative and vanishes. The trace of the pressure term also vanishes under homogeneity and solenoidality. Two integrations by parts give the viscous identity

$$2\nu \left\langle \delta a_i(\nabla'^2 a_i' - \nabla^2 a_i)\right\rangle = 2\nu\nabla_{\boldsymbol{r}}^2 \left\langle |\delta \boldsymbol{a}|^2\right\rangle - 4\nu \left\langle \partial_j a_i\, \partial_j a_i\right\rangle . \tag{489}$$

Restoring the Elsasser labels, $S_2^{\pm} = \left\langle|\delta \boldsymbol{z}^{\pm}|^2\right\rangle$, $\boldsymbol{Y}^{\pm} = \left\langle \delta \boldsymbol{z}^{\mp}|\delta \boldsymbol{z}^{\pm}|^2\right\rangle$, and $\varepsilon_{\mathrm{d}}^{\pm} = \nu\left\langle|\boldsymbol{\nabla} \boldsymbol{z}^{\pm}|^2\right\rangle$ recovers Equation 291.

Stationarity removes $\partial_t S_2^{\pm}$. In an inertial interval, forcing varies smoothly across r so $\langle \delta \boldsymbol{z}^{\pm} \cdot \delta \boldsymbol{f}^{\pm}\rangle$ becomes negligible, while the explicit separation-space diffusion becomes negligible away from the dissipation scale. The finite mean dissipation survives the large-Reynolds-number limit and leaves

$$\boldsymbol{\nabla}_{\boldsymbol{r}} \cdot \boldsymbol{Y}^{\pm} = -4\varepsilon^{\pm}. \tag{490}$$

Integrating this divergence over a three-dimensional ball of radius r provides a geometric alternative to Equation 293.

$$\int_{\mathcal{V}_3(r)} \boldsymbol{\nabla}_{\boldsymbol{r}} \cdot \boldsymbol{Y}^{\pm}\, \mathrm{d}V = 4\pi r^2 Y_L^{\pm}(r), \qquad\qquad -4\varepsilon^{\pm}\mathcal{V}_3(r) = -4\varepsilon^{\pm}\frac{4\pi r^3}{3}. \tag{491}$$

Here $4\pi r^2$ is the sphere's surface area and $\mathcal{V}_3(r) = 4\pi r^3/3$ is the ball's volume. Equating the two sides immediately yields $Y_L^{\pm} = -(4/3)\varepsilon^{\pm} r$.

J Why an exponent gains one under increment–spectrum conversion

A one-dimensional spectrum $E(k)$ uses the normalization

$$\frac{1}{2}\left\langle|\boldsymbol{a}|^2\right\rangle = \int_0^{\infty} E(k)\,\mathrm{d}k. \tag{492}$$

Up to a convention-dependent geometric factor, homogeneity relates the second-order increment to the spectrum through

$$S_2(\lambda) \sim \int_0^{\infty} [1-\cos(k\lambda)]\, E(k)\,\mathrm{d}k. \tag{493}$$

For an inertial-range power law $E(k) = Ck^{-m}$ with $1 < m < 3$, the change of variable $q = k\lambda$ gives

$$S_2(\lambda) \sim C\lambda^{m-1}\int_0^{\infty} (1-\cos q) q^{-m}\,\mathrm{d}q \propto \lambda^{m-1}. \tag{494}$$

Thus $\delta a_\lambda \propto \lambda^h$ implies

$$\boxed{m = 1 + 2h, \qquad E(k) \propto k^{-(1+2h)}.} \tag{495}$$

The weak-turbulence value $h = 1/2$ gives $m = 2$, GS95 gives $h = 1/3$ and $m = 5/3$, and scale-dependent alignment with $h = 1/4$ gives $m = 3/2$.

K Assumptions, times, and predictions for the cascade regimes

Regime	Defining assumption	Cascade time	Increment	Perpendicular spectrum
Isotropic IK	$\tau_{\mathrm{A}} = \lambda/v_{\mathrm{A}} \ll \tau_{\mathrm{nl}}$	$\tau_{\mathrm{cas}} \sim \tau_{\mathrm{nl}}^2/\tau_{\mathrm{A}}$	$\delta z_\lambda \sim (\varepsilon v_{\mathrm{A}} \lambda)^{1/4}$	$E(k) \propto k^{-3/2}$
Weak anisotropic	$\ell_\parallel$ fixed, $\chi_\lambda \ll 1$	$\tau_{\mathrm{cas}} \sim \lambda^2/(\delta z_\lambda^2 \tau_{\mathrm{A}})$	$\delta z_\lambda \sim (\varepsilon/\tau_{\mathrm{A}})^{1/4}\lambda^{1/2}$	$E(k_\perp) \propto k_\perp^{-2}$
Strong GS95	$\tau_{\mathrm{A}} \sim \tau_{\mathrm{nl}}$	$\tau_{\mathrm{cas}} \sim \lambda/\delta z_\lambda$	$\delta z_\lambda \sim (\varepsilon\lambda)^{1/3}$	$E(k_\perp) \propto k_\perp^{-5/3}$
Aligned strong	$\tau_{\mathrm{nl}} \sim \lambda/(\delta z_\lambda \sin\theta_\lambda)$	same as nonlinear time	$\delta z_\lambda \propto \lambda^{1/4}$ if $\sin\theta_\lambda \propto \lambda^{1/4}$	$E(k_\perp) \propto k_\perp^{-3/2}$

The first and fourth rows share a spectral slope but not a physical picture. IK assumes isotropic weak collisions; aligned strong turbulence retains critical balance and develops anisotropic sheet geometry. A measured slope alone cannot distinguish them.

L Finite-deformation form of flux freezing

The map $\boldsymbol{x} = \boldsymbol{\chi}(\boldsymbol{a}, t)$ gives the position at time t of the plasma element labelled by $\boldsymbol{a}$. The deformation gradient and its Jacobian are

$$F_{ij}(\boldsymbol{a}, t) \equiv \frac{\partial \chi_i}{\partial a_j}, \qquad J(\boldsymbol{a}, t) \equiv \det \boldsymbol{F}. \tag{496}$$

Differentiating $\partial_t \chi_i = u_i(\boldsymbol{\chi}, t)$ with respect to a_j gives

$$\frac{\mathrm{D}F_{ij}}{\mathrm{D}t} = \frac{\partial u_i}{\partial x_k} F_{kj}. \tag{497}$$

Mass conservation gives

$$\rho(\boldsymbol{\chi}(\boldsymbol{a}, t), t) = \frac{\rho(\boldsymbol{a}, 0)}{J(\boldsymbol{a}, t)}. \tag{498}$$

The ideal induction and continuity equations combine into

$$\frac{\mathrm{D}}{\mathrm{D}t}\left(\frac{B_i}{\rho}\right) = \frac{B_k}{\rho}\frac{\partial u_i}{\partial x_k}. \tag{499}$$

Equation (497) shows that $F_{ij}B_j(\boldsymbol{a}, 0)/\rho(\boldsymbol{a}, 0)$ obeys the same equation and has the same initial value as B_i/ρ. Therefore

$$\frac{B_i(\boldsymbol{\chi}(\boldsymbol{a}, t), t)}{\rho(\boldsymbol{\chi}(\boldsymbol{a}, t), t)} = F_{ij}(\boldsymbol{a}, t)\frac{B_j(\boldsymbol{a}, 0)}{\rho(\boldsymbol{a}, 0)}, \tag{500}$$

$$B_i(\boldsymbol{\chi}(\boldsymbol{a}, t), t) = \frac{1}{J(\boldsymbol{a}, t)} F_{ij}(\boldsymbol{a}, t) B_j(\boldsymbol{a}, 0). \tag{501}$$

This is the Cauchy solution. It states that the same deformation gradient maps a material line element and a frozen-in magnetic field. For incompressible flow, $J = 1$.

M Why three-dimensional stretching can overcome diffusion

A smooth velocity field looks linear sufficiently close to a chosen trajectory. The simplest example is the steady diagonal strain

$$u_i = \lambda_i x_i \qquad \text{(no sum on } i\text{)}, \qquad \lambda_1 + \lambda_2 + \lambda_3 = 0, \tag{502}$$

where the second relation enforces incompressibility. We represent one magnetic Fourier mode as

$$B_i(\boldsymbol{x}, t) = \widetilde{B}_i(t) \exp[i\boldsymbol{k}(t) \cdot \boldsymbol{x}]\,. \tag{503}$$

The real part gives the physical field. Acting on this mode gives

$$\partial_t B_i = \left(\frac{\mathrm{d}\widetilde{B}_i}{\mathrm{d}t} + i \frac{\mathrm{d}k_j}{\mathrm{d}t} x_j \widetilde{B}_i \right) e^{i\boldsymbol{k}\cdot\boldsymbol{x}}, \tag{504}$$

$$u_j \partial_j B_i = i \lambda_j x_j k_j \widetilde{B}_i e^{i\boldsymbol{k}\cdot\boldsymbol{x}}, \qquad B_j \partial_j u_i = \lambda_i \widetilde{B}_i e^{i\boldsymbol{k}\cdot\boldsymbol{x}}, \tag{505}$$

$$\nabla^2 B_i = -k^2 \widetilde{B}_i e^{i\boldsymbol{k}\cdot\boldsymbol{x}}. \tag{506}$$

Substitution into the incompressible induction equation and separate matching of the terms that do and do not contain x_j give

$$\frac{\mathrm{d}k_i}{\mathrm{d}t} = -\lambda_i k_i, \qquad \frac{\mathrm{d}\widetilde{B}_i}{\mathrm{d}t} = \left(\lambda_i - \eta k^2\right) \widetilde{B}_i. \tag{507}$$

Their solutions are

$$k_i(t) = k_{i0} e^{-\lambda_i t}, \tag{508}$$

$$\widetilde{B}_i(t) = B_{i0} e^{\lambda_i t} \exp\left[-\eta \int_0^t k^2(t')\,\mathrm{d}t'\right] \qquad \text{(no sum on } i\text{)}. \tag{509}$$

Consider first a three-dimensional strain with

$$\lambda_1 > \lambda_2 \geq 0 > \lambda_3. \tag{510}$$

The magnetic field tends to align with the stretching direction $\widehat{\boldsymbol{e}}_1$, while a generic wavevector tends to align with the compression direction $\widehat{\boldsymbol{e}}_3$. Compression makes $k_3 = k_{30} e^{|\lambda_3| t}$ grow and Ohmic diffusion rapidly removes modes with $k_{30} \neq 0$. The modes that survive have k_{30} increasingly close to zero. Solenoidality requires

$$\boldsymbol{k} \cdot \widetilde{\boldsymbol{B}} = 0. \tag{511}$$

The most strongly amplified surviving modes can therefore have

$$\widetilde{\boldsymbol{B}} \parallel \widehat{\boldsymbol{e}}_1, \qquad \boldsymbol{k} \parallel \widehat{\boldsymbol{e}}_2. \tag{512}$$

The intermediate direction lets the field grow along $\widehat{\boldsymbol{e}}_1$ without forcing its reversal wavenumber into the compressive direction.

Two dimensions remove that option. Incompressibility gives

$$\lambda_2 = -\lambda_1 < 0. \tag{513}$$

If the growing field aligns with $\widehat{\boldsymbol{e}}_1$, solenoidality places its wavevector along $\widehat{\boldsymbol{e}}_2$. Equation (509) then gives

$$k_2(t) = k_{20} e^{\lambda_1 t}, \qquad \eta \int_0^t k_2^2(t')\,\mathrm{d}t' = \frac{\eta k_{20}^2}{2\lambda_1}\left(e^{2\lambda_1 t} - 1\right), \tag{514}$$

$$\widetilde{B}_1(t) = B_{10} \exp\left[\lambda_1 t - \frac{\eta k_{20}^2}{2\lambda_1}\left(e^{2\lambda_1 t} - 1\right)\right] \longrightarrow 0. \tag{515}$$

The Ohmic exponent then grows exponentially in time and eventually defeats the ordinary exponential stretching of the field. This calculation illustrates the geometrical distinction; it does not claim that every three-dimensional flow acts as a dynamo. Section 3.1 of Schekochihin and Cowley (2007) gives the full argument in terms of Lyapunov directions. The Les Houches lectures develop the same calculation (Schekochihin, 2007, pp. 8–13).

N Magnetic-energy identity in a periodic domain

Expanding the curl in Equation 306 and dotting the result with $\boldsymbol{B}/\mu_0$ gives

$$\frac{\mathrm{D}}{\mathrm{D}t}\left(\frac{B^2}{2\mu_0}\right) = \frac{B_i B_j}{\mu_0}\,\partial_j u_i + \frac{\eta}{\mu_0}\,\boldsymbol{B}\cdot\nabla^2\boldsymbol{B}, \qquad \frac{\mathrm{D}}{\mathrm{D}t} \equiv \partial_t + \boldsymbol{u}\cdot\boldsymbol{\nabla}. \tag{516}$$

The diffusive contribution obeys

$$\begin{aligned} \boldsymbol{B}\cdot\nabla^2\boldsymbol{B} &= -\boldsymbol{B}\cdot\boldsymbol{\nabla}\times(\boldsymbol{\nabla}\times\boldsymbol{B}) \qquad (\boldsymbol{\nabla}\cdot\boldsymbol{B} = 0) \\ &= -|\boldsymbol{\nabla}\times\boldsymbol{B}|^2 + \boldsymbol{\nabla}\cdot[\boldsymbol{B}\times(\boldsymbol{\nabla}\times\boldsymbol{B})]\,. \end{aligned} \tag{517}$$

The divergence theorem converts the last term into a surface integral,

$$\int_{\mathcal{V}} \boldsymbol{\nabla}\cdot[\boldsymbol{B}\times(\boldsymbol{\nabla}\times\boldsymbol{B})]\,\mathrm{d}V = \oint_{\partial\mathcal{V}} [\boldsymbol{B}\times(\boldsymbol{\nabla}\times\boldsymbol{B})]\cdot\mathrm{d}\boldsymbol{S}. \tag{518}$$

The symbol $\partial\mathcal{V}$ denotes the boundary of $\mathcal{V}$, and $\mathrm{d}\boldsymbol{S}$ denotes its outward-oriented surface element. Opposite faces cancel in a periodic domain. Incompressibility likewise converts the material derivative in Equation 516 into the time derivative of the volume average. These steps give Equation 319.

O Real-space closure of the Kazantsev model

The main text starts from the exact spectral closure problem and then uses the closed smooth-flow equation. This appendix records how the assumptions of the Kazantsev–Kraichnan velocity ensemble close the magnetic two-point function.

Velocity ensemble. A second point is $\boldsymbol{x}' = \boldsymbol{x}+\boldsymbol{r}$, the separation magnitude is $r = |\boldsymbol{r}|$, and $\widehat{r}_i = r_i/r$. The model prescribes a statistically homogeneous, isotropic, Gaussian, mirror-symmetric velocity field with zero correlation time,

$$\left\langle u_i(\boldsymbol{x},t) u_j(\boldsymbol{x}',t')\right\rangle = \kappa_{ij}(\boldsymbol{r})\,\delta(t-t'). \tag{519}$$

The tensor $\kappa_{ij}(\boldsymbol{r})$ gives the spatial velocity covariance, t' denotes a second time, and $\delta(t-t')$ denotes the Dirac delta distribution. Isotropy permits the decomposition

$$\kappa_{ij}(\boldsymbol{r}) = \kappa_N(r)\left(\delta_{ij} - \widehat{r}_i\widehat{r}_j\right) + \kappa_L(r)\widehat{r}_i\widehat{r}_j, \tag{520}$$

where κ_N and κ_L denote the transverse and longitudinal covariances. Mirror symmetry excludes a term proportional to $\epsilon_{ijm}\widehat{r}_m$. Incompressibility, $\partial_{r_i}\kappa_{ij} = 0$, relates the two scalar functions through

$$\kappa_N(r) = \kappa_L(r) + \frac{r}{2}\frac{\partial \kappa_L}{\partial r}. \tag{521}$$

Thus one scalar function, $\kappa_L(r)$, contains all of the prescribed velocity statistics.

Magnetic two-point function. The corresponding equal-time magnetic correlator is

$$\begin{aligned} H_{ij}(\boldsymbol{r},t) &\equiv \left\langle B_i(\boldsymbol{x},t)B_j(\boldsymbol{x}',t)\right\rangle \\ &= H_N(r,t)\left(\delta_{ij} - \widehat{r}_i\widehat{r}_j\right) + H_L(r,t)\widehat{r}_i\widehat{r}_j. \end{aligned} \tag{522}$$

Here H_N and H_L denote the transverse and longitudinal magnetic correlations. The solenoidal constraint $\boldsymbol{\nabla}\cdot\boldsymbol{B} = 0$ gives

$$H_N(r,t) = H_L(r,t) + \frac{r}{2}\frac{\partial H_L}{\partial r}. \tag{523}$$

The tensor closure problem therefore reduces to finding the single scalar function $H_L(r,t)$.

Origin of the closure problem. Writing the incompressible induction equation as

$$\partial_t B_i = \mathcal{I}_i + \eta\nabla^2 B_i, \qquad\qquad \mathcal{I}_i \equiv B_m\partial_m u_i - u_m\partial_m B_i, \tag{524}$$

defines $\mathcal{I}_i$ as the ideal induction operator. Differentiating Equation 522 with respect to time and using statistical homogeneity gives the exact equation

$$\partial_t H_{ij} = \left\langle \mathcal{I}_i(\boldsymbol{x},t)B_j(\boldsymbol{x}',t)\right\rangle + \left\langle B_i(\boldsymbol{x},t)\mathcal{I}_j(\boldsymbol{x}',t)\right\rangle + 2\eta\nabla_{\boldsymbol{r}}^2 H_{ij}. \tag{525}$$

Each ideal term contains a third-order correlator of the form $\langle uBB\rangle$. An evolution equation for that correlator would contain fourth-order moments, so Equation 525 displays the statistical closure problem explicitly.

Gaussian closure. For a zero-mean Gaussian velocity, the Furutsu–Novikov identity gives

$$\langle u_i(\boldsymbol{x},t)F[\boldsymbol{u}]\rangle = \int \mathrm{d}t'' \int \mathrm{d}^3x''\; \langle u_i(\boldsymbol{x},t)u_\ell(\boldsymbol{x}'',t'')\rangle \left\langle \frac{\delta F[\boldsymbol{u}]}{\delta u_\ell(\boldsymbol{x}'',t'')}\right\rangle, \tag{526}$$

where $F[\boldsymbol{u}]$ denotes any functional of the velocity realization and $\delta F/\delta u_\ell$ denotes a functional derivative. Taking $F = B_m(\boldsymbol{x},t)B_n(\boldsymbol{x}',t)$ replaces every $\langle uBB\rangle$ term in Equation 525. The factor $\delta(t-t'')$ in Equation 519 collapses the time integral, while functionally differentiating the induction equation converts the remaining magnetic response into H_{ij} and its spatial derivatives. This functional derivative measures how an infinitesimal velocity impulse at $(\boldsymbol{x}'',t'')$ changes the magnetic-field product. Because the kinematic induction equation is linear in $\boldsymbol{B}$, its response contains one magnetic field; multiplication by the second field and ensemble averaging therefore returns H_{ij}. The zero correlation time removes flow memory, and Gaussianity lowers the third-order moments to second order.

Projecting the closed tensor equation along $\widehat{\boldsymbol{r}}$ and using Equation 521 and Equation 523 gives

$$\partial_t H_L = \mathcal{K}\frac{\partial^2 H_L}{\partial r^2} + \left(\frac{4\mathcal{K}}{r} + \frac{\partial \mathcal{K}}{\partial r}\right)\frac{\partial H_L}{\partial r} + \left(\frac{\partial^2 \mathcal{K}}{\partial r^2} + \frac{4}{r}\frac{\partial \mathcal{K}}{\partial r}\right) H_L, \tag{527}$$

where

$$\mathcal{K}(r) \equiv 2\eta + \kappa_L(0) - \kappa_L(r). \tag{528}$$

The first term in $\mathcal{K}$ represents microscopic magnetic diffusion, while the velocity increment covariance $\kappa_L(0) - \kappa_L(r)$—one half of the longitudinal second-order structure-function coefficient—represents random pair separation. Equations (527) and (528) complete the closure by turning a stochastic vector equation into a deterministic scalar equation (Rincon, 2019, Secs. 3.4.2–3.4.4).

P Kazantsev equation in logarithmic wavenumber

The substitution in Equation 350 follows from a general trial $M = e^{ax+bt}\Psi$. Inserting it into Equation 349 gives

$$\partial_t \Psi + b\Psi = \frac{\gamma_\nu}{5}\left[\partial_x^2 \Psi + (2a-3)\partial_x \Psi + (a^2 - 3a + 6)\Psi\right]. \tag{529}$$

Choosing $a = 3/2$ removes drift and choosing $b = (\gamma_\nu/5)(a^2 - 3a + 6) = 3\gamma_\nu/4$ removes uniform growth. The remaining heat equation has the Green function

$$\Psi(x,t) = \frac{1}{\sqrt{4\pi(\gamma_\nu/5)t}} \int_{-\infty}^{\infty} \exp\left[-\frac{(x-x')^2}{4(\gamma_\nu/5)t}\right] \Psi(x',0)\,\mathrm{d}x', \tag{530}$$

which yields Equation 353 for an initially narrow spectrum.

References

G. K. Batchelor. *An Introduction to Fluid Dynamics.* Cambridge University Press, Cambridge, 2000. ISBN 9780521663960. doi: 10.1017/CBO9780511800955. First published 1967.

Andrey Beresnyak. The spectral slope and Kolmogorov constant of MHD turbulence. *Physical Review Letters*, 106:075001, 2011. doi: 10.1103/PhysRevLett.106.075001.

Andrey Beresnyak. Universal nonlinear small-scale dynamo. *Physical Review Letters*, 108(3):035002, 2012. doi: 10.1103/PhysRevLett.108.035002.

Andrey Beresnyak. Spectra of strong MHD turbulence from high-resolution simulations. *The Astrophysical Journal Letters*, 784(2):L20, 2014. doi: 10.1088/2041-8205/784/2/L20.

Andrey Beresnyak and Alexander Lazarian. *Turbulence in Magnetohydrodynamics.* De Gruyter, Berlin and Boston, 2019. ISBN 9783110263282. doi: 10.1515/9783110263282.

Dieter Biskamp. *Magnetohydrodynamic Turbulence.* Cambridge University Press, Cambridge, 2003. ISBN 9780521810111. doi: 10.1017/CBO9780511535222.

Stanislav Boldyrev. Spectrum of magnetohydrodynamic turbulence. *Physical Review Letters*, 96: 115002, 2006. doi: 10.1103/PhysRevLett.96.115002.

Axel Brandenburg and Kandaswamy Subramanian. Astrophysical magnetic fields and nonlinear dynamo theory. *Physics Reports*, 417(1–4):1–209, 2005. doi: 10.1016/j.physrep.2005.06.005.

Subrahmanyan Chandrasekhar. *Hydrodynamic and Hydromagnetic Stability*. Clarendon Press, Oxford, 1961. ISBN 9780486640716. Reprinted by Dover Publications, 1981.

Michael Chertkov, Gregory Falkovich, Igor Kolokolov, and Massimo Vergassola. Small-scale turbulent dynamo. *Physical Review Letters*, 83(20):4065–4068, 1999. doi: 10.1103/PhysRevLett.83.4065.

Jungyeon Cho and Ethan T. Vishniac. The anisotropy of MHD Alfvénic turbulence. *The Astrophysical Journal*, 539(1):273–282, 2000. doi: 10.1086/309213.

T. G. Cowling. The magnetic field of sunspots. *Monthly Notices of the Royal Astronomical Society*, 94:39–48, 1933. doi: 10.1093/mnras/94.1.39.

P. G. Drazin. *Introduction to Hydrodynamic Stability*. Cambridge University Press, Cambridge, 2002. ISBN 9780521009652. doi: 10.1017/CBO9780511809064.

Katia Ferrière. Plasma turbulence in the interstellar medium. *Plasma Physics and Controlled Fusion*, 62(1):014014, 2020. doi: 10.1088/1361-6587/ab49eb.

Uriel Frisch. *Turbulence: The Legacy of A. N. Kolmogorov*. Cambridge University Press, Cambridge, 1995. ISBN 9780521457132. doi: 10.1017/CBO9781139170666.

Sébastien Galtier. *Introduction to Modern Magnetohydrodynamics*. Cambridge University Press, Cambridge, 2016. ISBN 9781107158658. doi: 10.1017/CBO9781316665961.

Sébastien Galtier, Sergey V. Nazarenko, Alan C. Newell, and Annick Pouquet. A weak turbulence theory for incompressible magnetohydrodynamics. *Journal of Plasma Physics*, 63(5):447–488, 2000. doi: 10.1017/S0022377899008284.

J. P. Goedbloed, Rony Keppens, and Stefaan Poedts. *Magnetohydrodynamics of Laboratory and Astrophysical Plasmas*. Cambridge University Press, Cambridge, 2019. ISBN 9781107123922. doi: 10.1017/9781316403679.

Peter Goldreich and S. Sridhar. Toward a theory of interstellar turbulence. ii. strong Alfvénic turbulence. *The Astrophysical Journal*, 438:763–775, 1995. doi: 10.1086/175121.

Timothy S. Horbury, Miriam A. Forman, and Sean Oughton. Anisotropic scaling of magnetohydrodynamic turbulence. *Physical Review Letters*, 101:175005, 2008. doi: 10.1103/PhysRevLett.101.175005.

A. P. Kazantsev. Enhancement of a magnetic field by a conducting fluid. *Soviet Physics JETP*, 26:1031–1034, 1968. English translation of Zh. Eksp. Teor. Fiz. 53, 1806 (1967).

Neco Kriel, James R. Beattie, Amit Seta, and Christoph Federrath. Fundamental scales in the kinematic phase of the turbulent dynamo. *Monthly Notices of the Royal Astronomical Society*, 513(2):2457–2470, 2022. doi: 10.1093/mnras/stac969.

Neco Kriel, Mark R. Krumholz, Patrick J. Armstrong, James R. Beattie, and Jennifer Schober. Universal growth of magnetic energy during the nonlinear phase of subsonic and supersonic small-scale dynamos. *Physical Review E*, 113(4):045208, 2026. doi: 10.1103/8qjf-8gg4.

Russell M. Kulsrud and Stephen W. Anderson. The spectrum of random magnetic fields in the mean field dynamo theory of the Galactic magnetic field. *The Astrophysical Journal*, 396(2):606–630, 1992. doi: 10.1086/171743.

Jason Maron and Peter Goldreich. Simulations of incompressible magnetohydrodynamic turbulence. *The Astrophysical Journal*, 554(2):1175–1196, 2001. doi: 10.1086/321413.

Joanne Mason, Fausto Cattaneo, and Stanislav Boldyrev. Dynamic alignment in driven magnetohydrodynamic turbulence. *Physical Review Letters*, 97:255002, 2006. doi: 10.1103/PhysRevLett.97.255002.

Joanne Mason, Fausto Cattaneo, and Stanislav Boldyrev. Numerical measurements of the spectrum in magnetohydrodynamic turbulence. *Physical Review E*, 77:036403, 2008. doi: 10.1103/PhysRevE.77.036403.

Sean Oughton and William H. Matthaeus. Critical balance and the physics of magnetohydrodynamic turbulence. *The Astrophysical Journal*, 897(1):37, 2020. doi: 10.3847/1538-4357/ab8f2a.

Eugene N. Parker. Hydromagnetic dynamo models. *The Astrophysical Journal*, 122:293–314, 1955. doi: 10.1086/146087.

Jean Carlos Perez, Joanne Mason, Stanislav Boldyrev, and Fausto Cattaneo. On the energy spectrum of strong magnetohydrodynamic turbulence. *Physical Review X*, 2:041005, 2012. doi: 10.1103/PhysRevX.2.041005.

Hélène Politano and Annick Pouquet. Dynamical length scales for turbulent magnetized flows. *Geophysical Research Letters*, 25(3):273–276, 1998. doi: 10.1029/97GL03642.

Stephen B. Pope. *Turbulent Flows*. Cambridge University Press, Cambridge, 2000. ISBN 9780521598866. doi: 10.1017/CBO9781316179475.

François Rincon. Dynamo theories. *Journal of Plasma Physics*, 85(4):205850401, 2019. doi: 10.1017/S0022377819000539.

Alexander A. Schekochihin. The fluctuation dynamo problem, August 2007. URL https://www-thphys.physics.ox.ac.uk/people/AlexanderSchekochihin/notes/leshouches07.pdf. Les Houches lectures on plasma (astro)physics.

Alexander A. Schekochihin. MHD turbulence: A biased review. *Journal of Plasma Physics*, 88(5):155880501, 2022. doi: 10.1017/S0022377822000721.

Alexander A. Schekochihin and Steven C. Cowley. Turbulence and magnetic fields in astrophysical plasmas. In Sergei Molokov, René Moreau, and H. Keith Moffatt, editors, *Magnetohydrodynamics: Historical Evolution and Trends*, volume 80 of *Fluid Mechanics and Its Applications*, pages 85–115. Springer, Dordrecht, 2007. doi: 10.1007/978-1-4020-4833-3_6.

Alexander A. Schekochihin, Stanislav A. Boldyrev, and Russell M. Kulsrud. Spectra and growth rates of fluctuating magnetic fields in the kinematic dynamo theory with large magnetic Prandtl numbers. *The Astrophysical Journal*, 567(2):828–852, 2002a. doi: 10.1086/338697.

Alexander A. Schekochihin, Steven C. Cowley, Gregory W. Hammett, Jason L. Maron, and James C. McWilliams. A model of nonlinear evolution and saturation of the turbulent MHD dynamo. *New Journal of Physics*, 4:84, 2002b. doi: 10.1088/1367-2630/4/1/384.

Alexander A. Schekochihin, Steven C. Cowley, Samuel F. Taylor, Gregory W. Hammett, Jason L. Maron, and James C. McWilliams. Saturated state of the nonlinear small-scale dynamo. *Physical Review Letters*, 92(8):084504, 2004a. doi: 10.1103/PhysRevLett.92.084504.

Alexander A. Schekochihin, Steven C. Cowley, Samuel F. Taylor, Jason L. Maron, and James C. McWilliams. Simulations of the small-scale turbulent dynamo. *The Astrophysical Journal*, 612(1): 276–307, 2004b. doi: 10.1086/422547.

H. C. Spruit. Essential magnetohydrodynamics for astrophysics, 2013. URL https://arxiv.org/abs/1301.5572.

Ya. B. Zel'dovich. The magnetic field in the two-dimensional motion of a conducting turbulent liquid. *Soviet Physics JETP*, 4:460–462, 1957.